Spring 2018

THE SAUDI ARAMCO JOURNAL OF TECHNOLOGY
A quarterly publication of the Saudi Arabian Oil Company

Saudi Aramco Journal of Technology

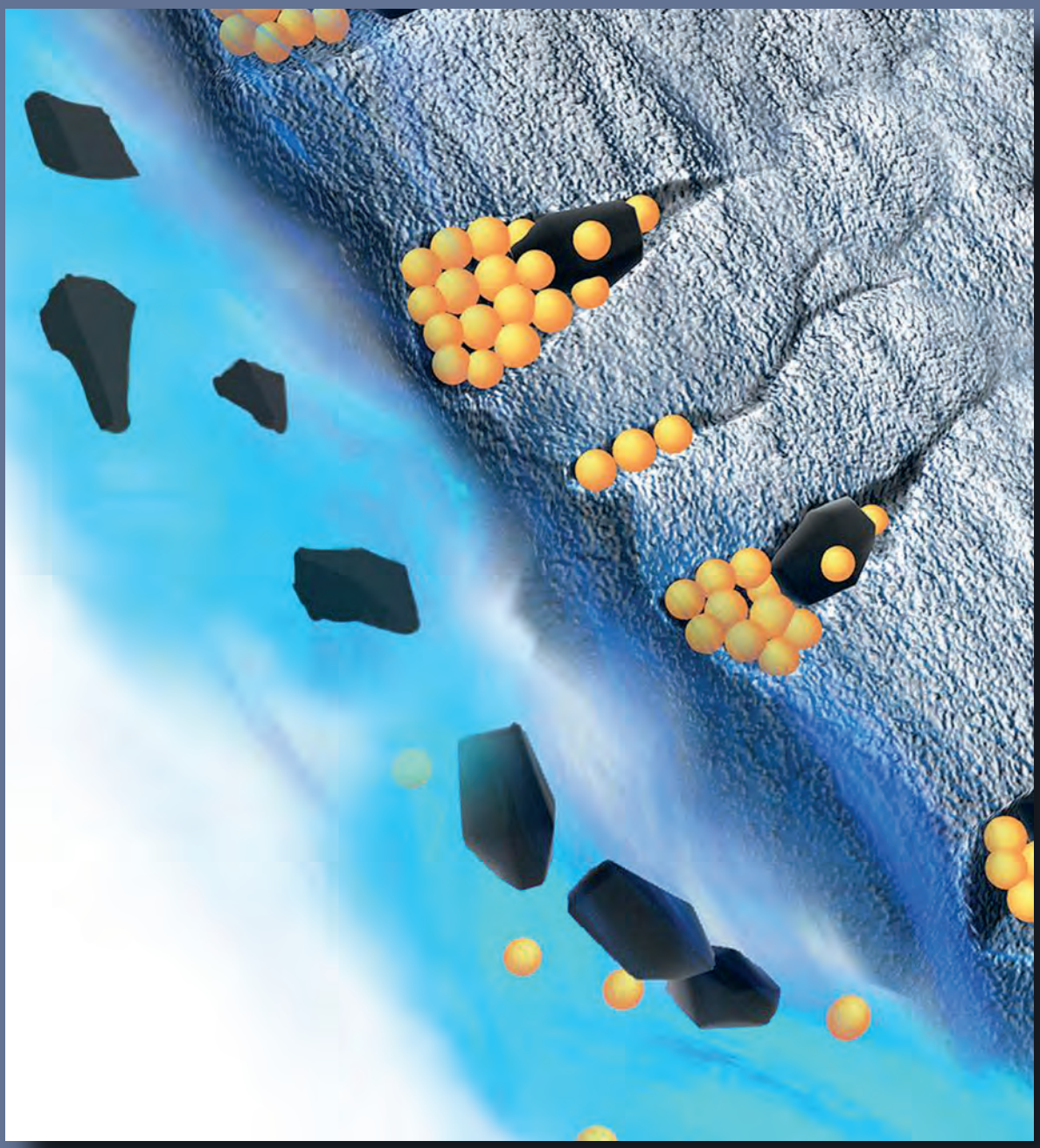

An engineer performing the mud check to confirm that the parameters meet the drilling program requirements for the well.

On the Cover

Micronized sealing co-polymer along with sized marble and graphite, seal off the fracture and strengthen the wellbore to enable the drilling of high overbalance wells.

MORE SAUDI ARAMCO JOURNAL OF TECHNOLOGY ARTICLES AVAILABLE ON THE INTERNET.

Additional articles that were submitted for publication in the *Saudi Aramco Journal of Technology* are being made available online. You can read them at this link on the Saudi Aramco Internet Website: www.saudiaramco.com/jot

The *Saudi Aramco Journal of Technology* is published quarterly by the Saudi Arabian Oil Company, Dhahran, Saudi Arabia, to provide the company's scientific and engineering communities a forum for the exchange of ideas through the presentation of technical information aimed at advancing knowledge in the hydrocarbon industry.

Complete issues of the Journal in PDF format are available on the Internet at: http://www.saudiaramco.com (click on "publications").

SUBSCRIPTIONS

Send individual subscription orders, address changes (see page 73) and related questions to:

Saudi Aramco Public Relations Department
JOT Distribution
Box 5000
Dhahran 31311, Saudi Arabia
Website: www.saudiaramco.com/jot

CONTRIBUTIONS

Relevant articles are welcome. Submission guidelines are printed on the last page. Please address all manuscript and editorial correspondence to:

EDITOR

William E. Bradshaw
The *Saudi Aramco Journal of Technology*
C-11B, Room AN-1080
North Admin Building #175
Dhahran 31311, KSA
Tel: +966-013-876-0498
Email: *william.bradshaw.1@aramco.com.sa*

Unsolicited articles will be returned only when accompanied by a self-addressed envelope.

PRODUCTION COORDINATION

Richard E. Doughty

DESIGN

Graphic Engine Design Studio,
Austin, Texas, U.S.A.

ISSN 1319-2388.

The *Saudi Aramco Journal of Technology* gratefully acknowledges the assistance, contribution and cooperation of numerous operating organizations throughout the company.

أرامكو السعودية
saudi aramco

Spring 2018

THE SAUDI ARAMCO JOURNAL OF TECHNOLOGY
A quarterly publication of the Saudi Arabian Oil Company

Saudi Aramco Journal of Technology

Contents

A New High Performance Bridging System Facilitates Drilling High Overbalance Wells in Depleted Formations

Rafael M. Pino Rojas, Carlos H. Parra C., Ajay Kumar V. Addagalla, and Prakash B. Jadhav

ABSTRACT

Wells drilled in the direction of minimum stress are potentially more favorable for reservoir development and optimal production because the fractures are more easily opened in this situation. In such a situation, hydraulic fractures grow transversely to the wellbore axis, allowing placement of multiple fractures without the possibility of fracture overlapping. Consequently, some wells that have been drilled in the minimum horizontal stress direction encounter several drilling-related problems, such as stuck pipe, downhole losses, wellbore instability, breakouts, and breakdowns.

A customized, high performance bridging system (HPBS) was developed that can be used in water-based mud (WBM) or oil-based mud (OBM) systems. This bridging system helps in drilling the wells with an overbalance of more than 4,500 pounds per square inch (psi) and mud weights exceeding 145 pounds per cubic foot (pcf). In addition, this newly designed system increases the operational efficiency by:

- Minimizing differential sticking
- Reducing downhole losses
- Improving wellbore stability
- Reducing torque and drag
- Enhancing lubricity
- Being environmentally acceptable

This system helps in drilling through depleted reservoirs or sections that lead to multiple reservoir targets where the required mud weight changes drastically. Designing drilling fluids from a wellbore strength point of view has proven successful for managing problems associated with high overbalance pressure and low formation strength. This article analyzes the results of using a deformable sealing polymer that seals the pore throats to avoid pore pressure transmission and maintain borehole integrity.

INTRODUCTION

Formation stresses have an important impact on drilling for hydrocarbons and reservoir development. Knowledge of formation stresses can help in planning the well path, improving completion strategies, and maintaining borehole stability[1]. Drilling a well in the minimum stress direction can have advantages, but it is also very challenging. These types of wells require unique drilling fluid systems with specialized products to make the drilling smoother, thereby reducing or eliminating nonproductive time. A clear advantage and benefit can be seen if we can use the appropriate products properly and efficiently.

Drilling in the minimum stress direction exposes the borehole to the maximum differential stress created by vertical and maximum horizontal in situ stresses. In this scenario, high mud weights are required to minimize the severity of breakouts. In the case of depleted reservoirs, the pore pressure may be well below hydrostatic pressure, leading to an increased risk of differential sticking while drilling across the reservoirs[2]. Most drilling-related problems, such as wellbore instability, tight hole, stuck pipe, and downhole losses, are exacerbated by drilling in the minimum horizontal stress direction. By designing the appropriate drilling fluid, many, if not all of these problems, can be addressed by a combination of wellbore strengthening and reducing pressure penetration into the formation.

This article describes the development of a wellbore strengthening package that efficiently seals the fractures and prevents their propagation, strengthens the wellbore, and prevents pressure penetration. The package strengthens wellbore stability while drilling, making it possible to drill with more than 4,500 psi of overbalance using mud weights exceeding 145 pcf.

Traditional wellbore strengthening fluids typically use a combination of sized calcium carbonate and graphite to seal the fracture openings. These particles form a seal at the fracture opening to help improve wellbore stability by increasing the hoop stress near the wellbore. A fracture will develop when the drilling fluid hydrostatic pressure exceeds the formation breakdown pressure. If the fluid contains appropriate particles, these can form a plug at the fracture opening, propping it open near the wellbore while dissipating fluid into the formation behind the plug that allows the fracture to close ahead of the plug. This is shown schematically in Figs. 1

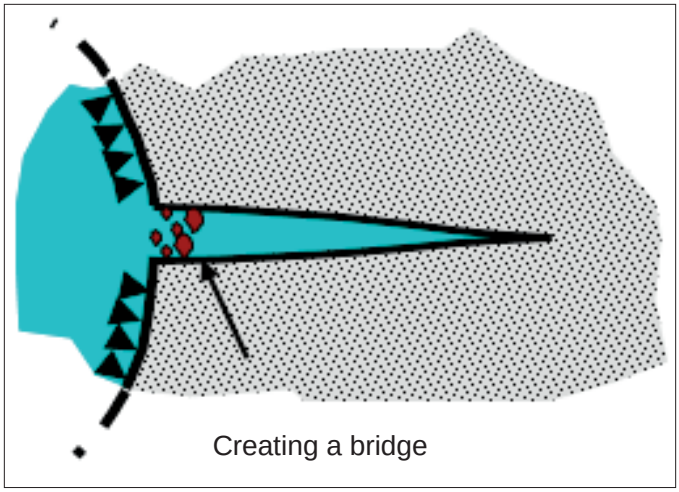

Fig. 1. Bridge creation.

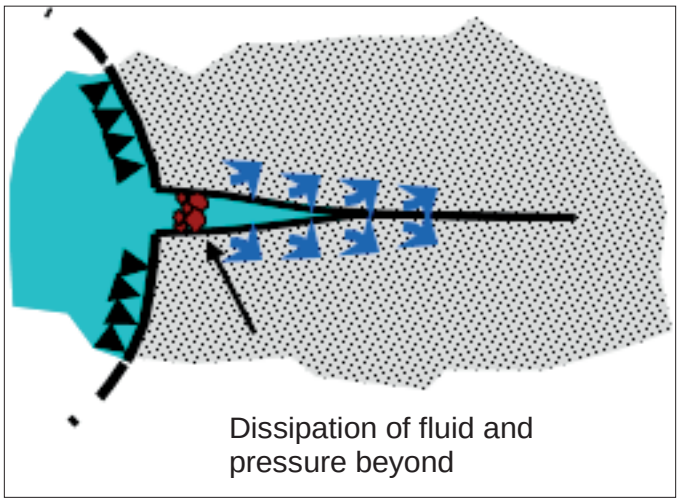

Fig. 2. Fluid dissipation.

and 2, which shows the bridge creation and fluid dissipation, respectively.

Alberty and McLean (2004)[3] were some of the first authors to develop this idea as a Stress Cage Theory, which was modeled only for induced fractures and permeable formations[3], but this concept has since been further developed into what is now known as wellbore strengthening.

Figure 3 shows different stress regimes around the wellbore and illustrates a typical scenario where the in situ stresses in a rock are dominant in one direction — (A) to (B) in this example. When a hole is bored through this rock, the pressure of the drilling fluid within the borehole will act evenly in all directions (Pw). This sets up an imbalance where the maximum in situ stresses are trying to squeeze the hole and force it into an oval shape, flatter in the (A) to (B) direction and extending in the (C) to (D) direction, where the directional stresses are less, giving this portion of the hole a narrower radius. This narrower radius portion is weakened and susceptible to shear failure.

When a connection is made, this effect is exacerbated; the "squeezing" effect increases due to the lower pressure exerted by the drilling fluid caused by the loss of equivalent circulating density when the pumps are shut down. When pumping resumes, there is often an equivalent circulating density surge that charges the area of weakened rock and a cycle is created, increasing the likelihood of hole enlargement and shear failure at the narrower radius areas. In addition, as the rock is compressed, tensile forces are set up in the compression area as the rock is "stretched" in the (C) to (D) direction. If the tensile/stretching forces are sufficient, tensile fracturing can occur in the (A) to (B) direction, i.e., in line with the maximum in situ stress and at right angles to the minimum stresses.

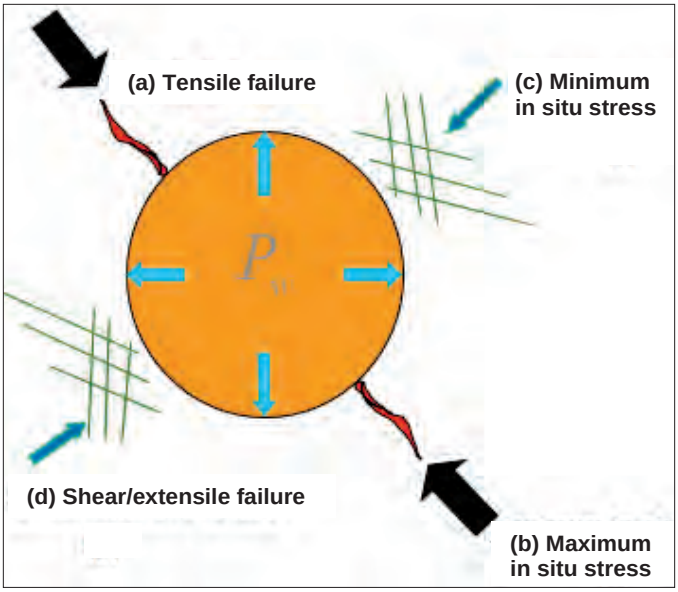

Fig. 3. Different stress regimes around the wellbore.

This is the crux of both the tendency toward borehole failure in these unequal stress situations and the mechanism to allow wellbore strengthening and drilling at high overbalance. As the wellbore fluid enters the tensile fractures, it will act against the fracture tip. The pressure transmission propagates the fracture and continues propagating it until the friction pressure losses on the fluid within the fracture equalize the pressure between the borehole and fracture tip. If many of these tensile fractures are created, the (A) to (B) sides of the hole will be increasingly weakened and may fail. If the fractures reach an in situ connected fracture system, there will be losses.

The application of the high performance bridging system (HPBS) addresses these potential issues by introducing a bridge — once a fracture has started — to plug the fracture mouth and prevent the well fluid pressure from acting on the fracture tip. This capability is critical in high overbalance situations. The HPBS also reduces or prevents the creation of more fractures by forcing flexible and rigid material into the fracture mouth to set up hoop stresses around the circumference of the borehole, overcoming the tensile stresses, which are creating the fractures in the first place, i.e., wellbore strengthening.

The wellbore strengthening technique has proven successful at improving formation strength[4], resulting in increased pore

pressure/fracture pressure margins and allowing marginal wells to be drilled with conventional drilling methods[5]. The application of wellbore strengthening may have many benefits:

- Enabling depleted zones to be drilled successfully.
- Minimizing well control situations due to unexpected losses.
- Reducing mud losses to the formation while drilling and when running casing (surging).
- Potentially eliminating a casing string, allowing two sections to be combined.
- Reducing drilling time.
- Improving the number of wells delivered.

Fig. 4. PPT.

HPBS

For wellbore strengthening to be successful, it is important to select the correct blend of products that will form a low permeability, high strength filter cake to seal the fracture and maintain overbalance pressure. It is essential that the treated drilling fluid has a very low fluid loss. Conventional filtration tests[6, 7] do not demonstrate the effect of the HPBS. Evaluation of the HPBS should be performed with a particle plugging tester (PPT), Fig. 4. This piece of equipment can allow filtration testing above 350 °F and 4,500 psi differential pressure, unlike conventional rig site filtration equipment. The PPT uses a slotted disc, Fig. 5a, or ceramic disc, Fig. 5b, as the filter medium, depending on fluid design requirement. Different permeability/pore size discs are available to simulate permeable formations, or a slotted disc can be used to simulate fractures and confirm whether the bridging package is appropriate to form a quick bridge across the pore throat or fracture.

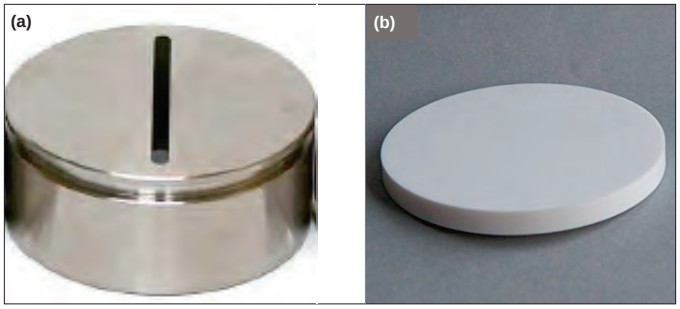

Fig. 5. The slotted disc (a), and the ceramic disc (b) used in the PPT.

An important property to determine whether the formation can be sealed quickly is the spurt loss, which is the amount of fluid going into the formation at time (t) = 0, when the formation is first exposed to the drilling fluid. This amount should be as low as possible; a low spurt loss indicates appropriate bridging material sizing and distribution. If the spurt loss value is high, the hoop stress benefit seen at the wellbore will be reduced because the fracture may be plugged or bridged, but futher in from the wellbore. If the fluid can form an impermeable pressure seal and the pressure behind the seal can leak off, then wellbore stability is still improved, though the near wellbore area may experience some breakout. The overall flu-

Product	Recommended Concentration	Units
Sealing Polymer	2% to 3%	By volume
Graphite — Different Grades	4 to 8	Pounds per barrel
Flaked Calcium Carbonate — Different Grades	4 to 6	Pounds per barrel
Sized Calcium Carbonate	10 to 30	Pounds per barrel

Table 1. Typical recommended product concentration

Fig. 6. SEM image of flaked calcium carbonate.

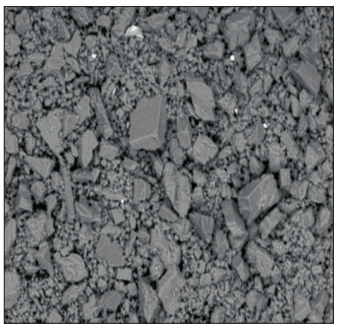

Fig. 7. SEM image of regular calcium carbonate.

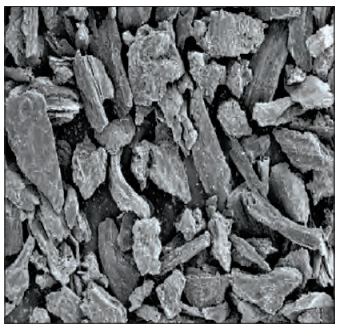

Fig. 8. SEM image of graphite.

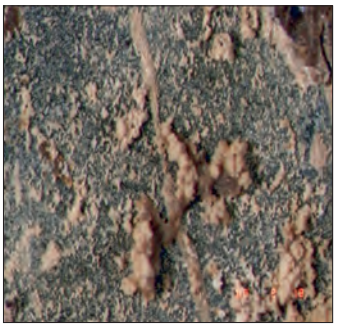

Fig. 9. SEM image of the sealing polymer locking pores and microfractures.

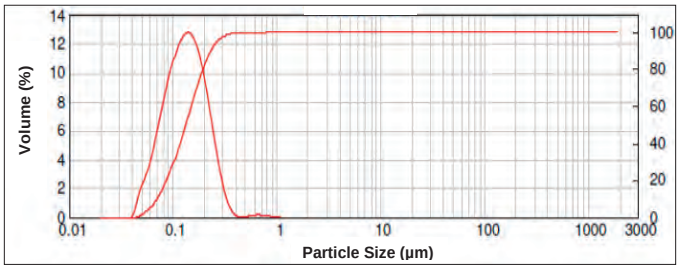

Fig. 10. PSD curve of the sealing polymer in freshwater.

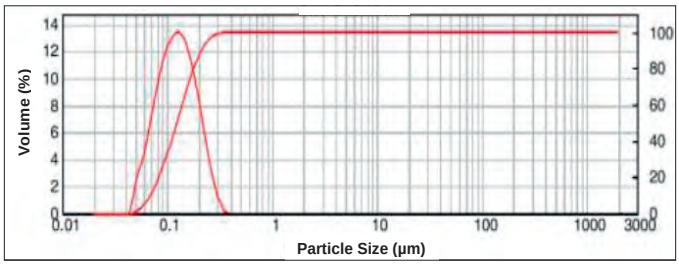

Fig. 11. PSD curve of the sealing polymer in a 20% sodium chloride solution.

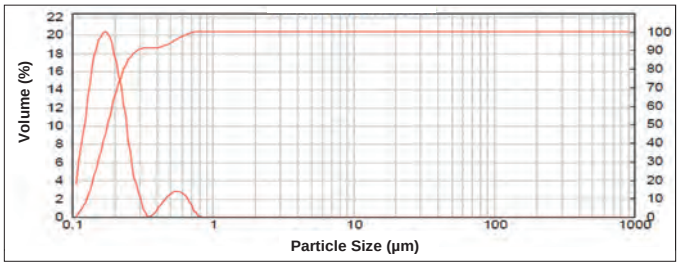

Fig. 12. PSD curve of the sealing polymer in a 20% calcium chloride solution.

id loss is used to indicate if there is sufficient bridging material in the fluid.

The use of flexible graphite in the drilling fluid has been shown to strengthen the reservoir rock, enabling it to remain stable despite an overbalance beyond the point at which physical failure has occurred in offset wells. The advantage of graphite is its deformability. Graphite creates a more effective pressure seal in the throats of fractures than hard particles, thereby preventing fracture propagation and subsequent failure[8].

Product Details

This HPBS consists of three products: (1) graphite, (2) calcium carbonate, and (3) a sealing polymer. To help seal the larger fractures, flaked calcium carbonate is used in addition to granular calcium carbonate. The combination of graphite and calcium carbonate can bridge and seal permeable formations, and can form a resilient plug in fractures that is strong enough to resist crushing as induced fractures close. The sealing polymer is small enough to seal micropores and microfractures in the formation and also fills any imperfections in the seal formed by the graphite and calcium carbonate. The sealing polymer also reduces the filtration rate, further minimizing pore pressure transmission. In permeable formations, the sealing polymer provides protection from differential sticking by sealing microporosity in the formation and by improving the seal formed by bridging particles in larger porosity zones. Table 1 shows the typical recommended concentrations of the products.

The products mentioned here can be used in both water-based mud (WBM) and oil-based mud (OBM) with no compatibility issues.

Figures 6 to 9 are the scanning electron microscope (SEM) images of the products used in the HPBS, which provides an idea of the shape of the particles.

LAB EVALUATION

The industry has used solid particles such as graphite and calcium carbonate in WBM and OBM for decades. The laboratory testing focused on simple fluids to identify whether the sealing polymer was compatible with WBMs and OBMs. The

Product	Medium	D10 (microns)	D50 (microns)	D90 (microns)
Sealing Polymer	Water	0.071	0.131	0.230
	20% NaCl Solution	0.07	0.122	0.208
	20% $CaCl_2$ Solution	0.128	0.179	0.293
D10 = 10% of the cumulative volume of the material D50 = 50% of the cumulative volume of the material D90 = 90% of the cumulative volume of the material				

Table 2. PSD of the sealing polymer in various aqueous media

Product	Concentration	Mixing Time (min.)	Units
Diesel	0.7838	—	bbl/bbl
Primary Emulsifier	0.0184	5	bbl/bbl
Secondary Emulsifier	0.0030	5	bbl/bbl
Brine Phase	0.0948	20	bbl/bbl
Sealing Polymer	0.1	5	bbl/bbl

Table 3. Formulation for the weak oil-based emulsion used to identify where the sealing polymer is distributed in the OBM

Fig. 13. The OBM with the sealing polymer after 30 minutes in a static state at room temperature.

sealing polymer is an aqueous suspension of particles and it is important for the particles to maintain their discrete size to provide the improvements in pressure transmission and filtration control in the drilling mud.

WBM

The sealing polymer can be dispersed in the aqueous phase without any adverse effect on the WBM properties. The typical aqueous phase used in WBM in Saudi Arabia is either freshwater or seawater, with commonly used brines like sodium chloride or calcium chloride. Research has shown that the addition of sealing polymers to WBM reduces the rate of pressure invasion[9] into the wellbore by forming a semi-permeable membrane. The particle size distribution (PSD) of the sealing polymer is ideally suited to sealing shale formations and significantly improves osmotic efficiency. Using a Malvern mastersizer, Fig. 10 shows the PSD curve of the sealing polymer in freshwater, Fig. 11 shows the PSD curve of the sealing polymer in a 20% sodium chloride solution, and Fig. 12 shows the PSD curve of the sealing polymer in a 20% calcium chloride solution.

Table 2 shows that the sealing polymer distributes uniformly in all the tested media types.

OBM

The pressure transmission in emulsion systems is managed by the generation of semi-permeable membrane and the osmotic potential pressure difference between shale and emulsion fluid. Sources of the semi-permeable membrane of OBM proposed include the oil film and emulsifier surrounding the emulsion[1]. The sealing polymer is an aqueous suspension of particles, so it would naturally be expected to accumulate in the internal brine phase of an OBM. To identify where the sealing polymer is distributed in the OBM, a weak oil-based emulsion was prepared, Table 3.

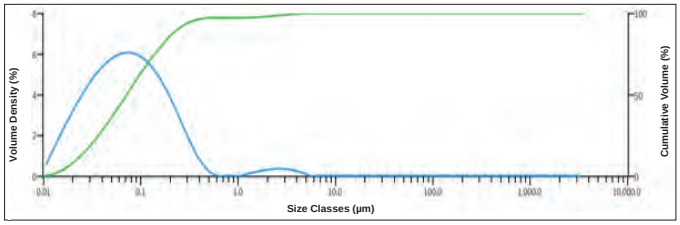

Fig. 14. PSD curve of the separated top, and the diesel layer.

The emulsion was mixed without any solid particulates that are used in a conventional OBM because they would be expected to mask the polymer PSD. A weak emulsion was used to allow three separate phases to quickly separate for testing: (1) a top diesel layer, (2) an emulsion interface, and (3) a bottom brine layer. A higher amount of sealing polymer was used in this test than would be used in a field application to ensure sufficient particles were available to disperse in the various phases and still be detectable by particle size analysis. Figure 13 shows the OBM with the sealing polymer after 30 minutes in a static state at room temperature.

The PSD of the separated top and the diesel layer clearly shows the polymer is at least partially dispersed into the oil phase and is maintaining its original particle size, Fig. 14. This demonstrates that although the polymer is added as an aqueous suspension, it can partition throughout an emulsion fluid.

To confirm that the sealing polymer would be expressed in the filtrate of an OBM and be available to seal the formation permeability and improve the filter cake quality, a simple, unweighted OBM was mixed as detailed in Table 4. In this case, the concentration of the sealing polymer was similar to what would be used in a field application.

A high-pressure, high temperature (HPHT) test was conducted to collect the filtrate from the above formulation. A Malvern particle size analyzer was used to check for the presence of the sealing polymer in the filtrate and then compared with the sealing polymer in an aqueous medium data reference. The results clearly showed the presence of a sealing polymer in the OBM filtrate.

This shows that the sealing polymer particles can be dispersed throughout the mud and can enter the formation in the filtrate where they seal micropores and microfractures.

Product	Units	Formulation	Mixing Time (mins)
Diesel	bbl/bbl	0.7470	—
Organophilic Clay	Pounds per barrel	4	5
Primary Emulsifier	bbl/bbl	0.0184	5
Secondary Emulsifier	bbl/bbl	0.0030	5
Lime	Pounds per barrel	1	5
Brine	bbl/bbl	0.2036	30
Sealing Polymer	bbl/bbl	0.02	5

Table 4. Formulation for the unweighted OBM

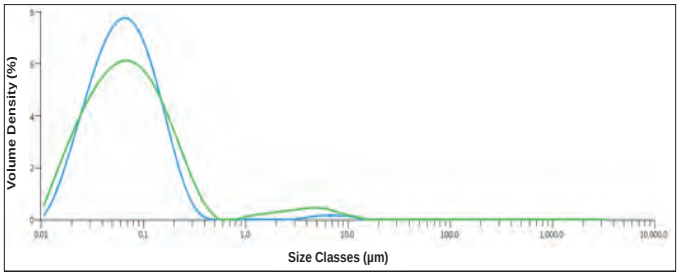

Fig. 15. The PSD curve of the sealing polymer in a filtrate (blue) compared to the sealing polymer in the OBM (green), from Table 3.

The PSD curve, Fig. 15, shows a small amount of larger particles, which suggests some secondary complexing. This small amount of a larger sealing polymer particulate may have some additional benefit in sealing more porous formations. These are dispersed in the entire mud system, which explains the minor effects on the rheological properties of the fluid, Tables 5 and 6, and the improvement in electrical stability. There is a very clear improvement in the filtration properties of the fluid.

Based on these findings, we can clearly say the sealing polymer mechanism in OBM is more complex, especially when

Product	**Units**	**Formulation A**	**Formulation B**	**Mixing Time** (min.)
Base Oil	lb/bbl	141.59	141.59	0
Primary Emulsifier	lb/bbl	4.5	4.5	0
Secondary Emulsifier	lb/bbl	4.5	4.5	0
Organophilic Clay	lb/bbl	7.75	7.75	5
Lime	lb/bbl	7	7	5
Water	lb/bbl	19.01	19.01	10
Calcium Chloride	lb/bbl	79.24	79.24	10
Barite	lb/bbl	302.90	302.90	30
Sealing Polymer	vol	—	3%	40

Table 5. Formulation for the OBM

Mud Properties	**Units**	**Formulation A**	**Formulation B**
Density	pcf	100	100
ES	Volts	399	458
Plastic Viscosity (cP)	cP	36	38
Yield Point	lb/100 ft^2	17	22
6 RPM	lb/100 ft^2	9	10
3 RPM	lb/100 ft^2	7	8
Gels 10”/10 ft	lb/100 ft^2	9/11	10/13
Spurt Loss	ml	0.5	0.1
HPHT Fluid Loss	ml	3.2	1.2
HPHT	°F/psi	250/500	

Table 6. Properties comparing the formulation with and without a sealing polymer

Section Length	**4,000 ft**
Last Casing	7” liner
Hole Size	5⅞”
Formation	Interbedded shale with carbonate
Mud Weight	144 pcf (19.2 pounds per gallon)
Expected Overbalance	~4,455 psi
Maximum Inclination	78°
Mud System	Oil-based HPBS
Expected Bottom-hole Temperature	~300 °F

Table 7. Details of the subject test well

Fig. 16. Sealing polymer in water.

Fig. 17. Sealing polymer in a typical unweighted OBM.

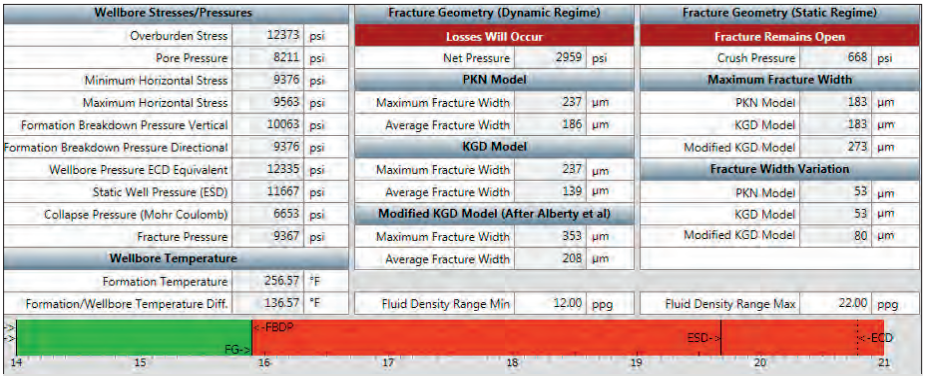

Fig. 18. Proprietary bridging software utilized to select the optimum particle sizes.

compared to its behavior in an aqueous system. While it is true that filtrate loss in OBM is oil, it is equally true that the product can still deliver submicron particles — dispersed in the oil phase via shear dispersion — into the formation with the filtrate to seal microfractures and other formation irregularities. Figures 16 and 17 show the dispersion of the sealing polymer in the medium of the aqueous solution (water) and a typical unweighted OBM, respectively. It clearly

Targets and Results			
	D-90	D-50	D-10
Target for Kaeuffer Rule	139.049	42.916	1.717
Product Mix PSD	529.47	42.588	2.863
Difference	390.422	-0.329	1.146
Untreated Mud PSD	—	—	—
Treated Mud PSD	529.47	42.588	2.863

Table 8. HPBS products and concentration used to obtain the resultant PSD

Product	Recommended Concentration	Units
Sealing Polymer	3%	By volume
Graphite – F	6	Pounds per barrel
Graphite – Regular	4	Pounds per barrel
Flaked Calcium Carbonate	5	Pounds per barrel
Calcium Carbonate – F	5	Pounds per barrel

Table 9. Target results for the cumulative volume of the material used to determine the PSD

Material	Unit	Quantity	Property	Unit	Value
Water	bbl	As Req.	Density	pcf	140 to 144
Diesel	bbl	As Req.	Plastic Viscosity	cP	ALAP
Organophillic Clay	lb	6	Yield Point	lb/100 ft²	16 to 18
Fluid Loss Control Agent	lb	8	Gels, 10 sec/10 min	lb/100 ft²	10/16 to 12/18
Primary Emulsifier	Gallons per barrel (gpb)	1.5	LSYP	lb/100 ft²	≥ 10
$CaCl_2$	lb	~8	OWR		85/15
Secondary Emulsifier/ Wetting Agent	gpb	1.0	Excess Lime	lb/bbl	≥ 2
Lime	lb	5	Drilled Solids	% vol	< 5
Wetting Agent	gpb	0.25	$CaCl_2$ (in water phase)	% by wt	20 to 25
Barite	lb	As Req.	ES	Volt	≥ 800
Low End Rheology Modifier	lb	1-2	HPHT Filtrate at 300 °F and 500 psi	ml/30 min	< 3.0 (FW = 0)
Sealing Polymer	% v/v	2.5% to 3%	HPHT Filtrate Cake Thickness	1/32"	2 to 3
Sized Marble	lb	5	PPT Filtrate at 300 °F and 4,500 psi	ml/30 min	< 4.0
Resilient Graphite — F&R	lb	10	Spurt Loss	ml	< 0.5
Flaked Calcium Carbonate	lb	5			

Table 10. Mud formulation, properties and the PSD of the bridging additives that were continuously monitored

shows there is no miscibility issues.

The sealing polymer helps in reducing the HPHT filtrate in OBM by sealing the microfractures. This also helps in improving the filter cake quality.

The following observations were drawn based on the lab results and field experience.

- Sealing polymer can be used in OBM and WBM.
- It is suitably sized to plug micropores and microfractures.
- It can be used in a saline and calcium environment without reduction in performance.
- It can increase the electrical stability of the OBM.
- It reduces the HPHT fluid loss for OBM.
- It improves the filter cake quality.

The following observations were drawn based on the lab results.

- The sealing polymer can be used in OBM and WBM.
- It is suitably sized to plug micropores and microfractures.
- It can be used in both a saline and calcium environment without reduction in performance.
- It can increase the electrical stability of the OBM.
- It reduces the HPHT fluid loss for OBM.
- It improves the quality of the filter cake.

CASE HISTORY

Table 7 is a list of details concerning the subject test well.

Background

This well is planned to drill as a single lateral across the reservoir. This will be drilled in a minimum stress direction with a section length of 4,000 ft and an overbalance of approximately 4,500 psi and completed with open hole multistage fracturing completion.

Challenges

The offset wells and motherbore associated risk were reviewed, as listed:

- Salt water influx.
- Expected severe losses across the upper reservoir formations.
- High density fluid management with losses and influx situation.
- Differential sticking across low-pressure formations.
- High slanted section profile (> 60° inclination).

Fluids Design

The 5⅞" side track section was planned to drill utilizing the HPBS in OBM. Based on the rock properties, proprietary software was utilized to calculate and to simulate the fracture width at downhole conditions.

Results from the Software

The simulation predicted a fracture width up to 139 µ to reduce chances for losses and differential sticking across the reservoir section. The microfractures simulated were targeted to seal across the fracture throat using optimum sizes of bridging additives to include resilient graphite and sized marble to increase hoop stress around the wellbore, minimizing breakouts across weak carbonate formations. Figure 18 is a screen shot of the proprietary bridging software, which was utilized to select the optimum particle sizes.

Bridging Software Output

Table 8 shows the HPBS used to obtain the previously mentioned resultant PSD.

Table 9 shows the target results for the cumulative volume of the material used to determine the PSD.

Fluid Formulation and Parameters

Table 10 lists the mud formulation and properties along with the PSD of the bridging additives that were continuously monitored and precisely controlled through appropriate drilling fluids engineering. HPHT and PPT fluid loss was uncontrolled when tested without a HPBS.

Considerations While Drilling with HPBS

1. Coarser shaker screens must be used when compared to conventional mud. This will not be possible all the times when considering the economics.
2. Minimal effects on rheology will be observed from the addition of a sealing polymer.
3. The increase in low gravity solids due to the attrition of solids in the HPBS. A gradual increase in mud weight can be observed.
4. The increase in electrical stability.
5. Tighten the HPHT fluid loss and spurt loss.
6. Regular treatment of the HPBS should be made to the active system to compensate the the material loss on shakers.

Results

The operator was successfully able to drill and complete the section using a customized OBM HPBS across the extreme overbalance conditions (~4,500 psi overbalance).

CONCLUSIONS

The HPBS shows good performance in sealing the fractures both in the field and in the lab. This has been very successful around the world. More than 500 jobs were run in the Middle East with a success rate of more than 99.5%. Other case histories from the region indicate the successful drilling of wells having an overbalance greater than 5,000 psi and a bottom-hole temperature of 325 °F.

ACKNOWLEDGMENTS

The authors would like to thank the management of Saudi Aramco for their support and permission to publish this article. We would like to extend our gratitude toward Qassem Al-Saqer, who helped in the lab work during the entire project.

This article was presented at the SPE/IADC Middle East Drilling Technology Conference and Exhibition, Dubai, UAE, October 3-4, 2017.

REFERENCES

1. Zheng, Y., Tang, X. and Patterson, D.J.: "Identifying Stress-Induced Anisotropy and Stress Direction Using Cross-Dipole Acoustic Logging," SPWLA paper 2009-21660, presented at the SPWLA 50th Annual Logging Symposium, The Woodlands, Texas, June 21-24, 2009.
2. Ahmed, S., Khan, K., Omini, P.I., Abdulaziz, A., et al.: "An Integrated Drilling and Geomechanics Approach Helps to Successfully Drill Wells along the Minimum Horizontal Stress Direction in Khuff Reservoirs," SPE paper 171755, presented at the Abu Dhabi International Petroleum Exhibition and Conference, Abu Dhabi, UAE, November 10-13, 2014.
3. Alberty, M.W. and McLean, M.R.: "A Physical Model for Stress Cages," SPE paper 90493, presented at the SPE Annual Technical Conference and Exhibition, Houston, Texas, September 26-29, 2004.
4. Fett, J.D., Martin, F., Dardeau, C., Rignol, J., et al.: "Case History: Successful Wellbore Strengthening Approach in a Depleted and Highly Unconsolidated Sand in Deepwater Gulf of Mexico," SPE paper 119748, presented at the SPE/IADC Drilling Conference and Exhibition, Amsterdam, the Netherlands, March 17-19, 2009.
5. Moroni, L.P., Vickers, S., Trenery, J., et al.: "Enhancing Bridging and Sealing to Drill Highly Overbalanced Wells," paper presented at the Rio Oil and Gas Expo and Conference 2010, Rio de Janerio, Brazil, September 13-16, 2010.
6. *Recommended Practice for Field Testing of Water-based Drilling Fluids*, API RP 13B-1, 4th edition, March 2009, 91 p.
7. *Recommended Practice for Field Testing of Oil-based Drilling Fluids*, API RP 13B-2, 5th edition, April 2014, 141 p.
8. Davison, J.M., Leaper, R., Cauley, M.B., Bennett, B., et al.: "Extending the Drilling Operating Window in Brent: Solutions for Infill Drilling in Depleting Reservoirs," SPE paper 87174, presented at the IADC/SPE Drilling Conference, Dallas, Texas, March 2-4, 2004.
9. Dye, B., Clapper, D., Hansen, N., Leaper, R. et al.: "Design Considerations for High Performance Water-based Muds," paper AADE-04-DF-HO-14, presented at the AADE Drilling Fluids Conference, Houston, Texas, April 6-7, 2004.

BIOGRAPHIES

Rafael M. Pino Rojas joined Saudi Aramco in June 2013 as a Drilling Engineer working in the Drilling Operations Support Unit of the Drilling Technical Department. He has over 15 years of experience in technical and operational procedures, including coordination and supervision of onshore operations in Venezuela and offshore operations in Saudi Arabia. Rafael was trained as a Drilling and Completion Fluids Engineer and has advanced knowledge in the design and field application of oil-based drilling fluid systems (invert emulsion, 100% oil) and water-based systems (conventional, high performance and drill-in), as well as the elaboration of drilling fluids techno-economic proposals under different contract schemes.

Prior to joining the company, he worked for Baker Hughes for 13 years.

Rafael received his B.S. degree in Chemical Engineering from the Universidad Central de Venezuela, Caracas, Venezuela.

Carlos H. Parra C. is currently working as a Drilling Fluids Specialist in Saudi Aramco's Drilling Technical Department. He has more than 23 years of oil and gas field experience and has served in various positions, including as a Field Engineer, technical support, supervisory and managerial positions. Carlos's areas of expertise include drilling and completion fluids, well productivity and drilling optimization.

He received his B.S. degree in Petroleum Engineering from the Universidad Industrial de Santander, Bucaramanga, Colombia.

Ajay Kumar V. Addagalla is currently working as the Technical Manager for Drilling and Completion at Baker Hughes, a GE company for the Saudi Arabia and Bahrain Geomarket. He has more than 9 years of oil field experience and has served in various positions in Engineering, Operations and Sales. Ajay's areas of expertise include drill-in fluids, completion fluids and near wellbore damage remediation techniques.

He received his B.Tech. degree in Chemical Engineering from Jawaharlal Nehru Technological University, Hyderabad, India, and his M.S. degree in Petroleum and Environmental Engineering from University of Nottingham, Nottingham, U.K.

Prakash B. Jadhav is currently working as an Operations Manager at Baker Hughes, a GE company, in the Drilling and Completions fluids product line for the Saudi Arabia and Bahrain Geomarket. He has more than 15 years of experience in the oil industry, and has executed critical high-pressure, high temperature, extended reach drilling and deepwater well campaigns with major operators and worked in more than five countries. Prakash has served in various positions in Operations and Sales before coming to Saudi Arabia in his current position.

He received his B.Tech. degree in Chemical Engineering from Dr. Babasaheb Ambedkar Technological University, Lonere, India.

Novel Fibrous Lost Circulation Materials Derived from Deceased Date Tree Waste

Dr. Jothibasu Ramasamy and Dr. Md. Amanullah

ABSTRACT

A novel fibrous eco-friendly lost circulation material (LCM) has been developed using natural date tree waste as the raw material. As the source of raw material is sustainable and available in huge quantities in the Kingdom of Saudi Arabia and in the Middle Eastern region, it has a great potential to be used as a raw material for the manufacturing of locally made fibrous LCMs for the application during drilling and cementing to mitigate loss of circulation. This article describes the properties of fibrous LCM in different water-based drilling mud systems. The raw material for the fibrous LCM is deceased date tree waste, which are available in huge quantities every year.

A deceased date tree trunk has been used to produce fibers for the application in the drilling industry. The trunk has been subjected to a crushing and grinding process to generate fibrous materials of different sizes and aspect ratio. The fibrous material has been incorporated in different water-based mud systems such as gel polymer (bentonite) mud, potassium chloride (KCl) polymer mud, sodium chloride (NaCl) polymer mud, and calcium chloride ($CaCl_2$) polymer mud. These fiber containing muds have been tested using a pore plugging test (PPT) apparatus for evaluating the sealing efficiency of the fibrous material. A 2 mm slotted disk has been used as a filter medium simulating a fractured formation of the wellbore. Experiments carried out at high-pressure, high temperature (HPHT) conditions prove that the fibrous material is a perfect choice to be used as a LCM for combating moderate types of lost circulation.

INTRODUCTION

Lost circulation is the partial or complete loss of drilling fluid or cement slurries into formation voids during drilling, running casing or cementing operations. It is one of the frequent challenges encountered during drilling operations, and it has been reported that lost circulation occurs during drilling in approximately 20% to 25% of the wells drilled worldwide[1]. Lost circulation can be encountered during any stage of drilling operations and occurs when drilling fluid or drilling mud pumped into a well returns partially or does not return to the surface. While some fluid loss is expected, excessive fluid loss is not desirable from a safety, an economical, or an environmental point of view. It is one of the most troublesome and costly problems encountered in drilling a well. Millions of dollars are being spent every year due to lost circulation and the detrimental effects it causes. Lost circulation has also been blamed for reduced production in that losses resulted in the failure to secure production tests and samples, while the plugging of production zones have led to decreased productivity[2].

Lost circulation is one of the major challenges of Saudi Aramco drilling operations in the Kingdom and is the major contributor for drilling nonproductive time. It can also lead to associated drilling problems, such as well control, borehole instability, stuck pipe, unsuccessful production tests, poor hydrocarbon production after well completion, and formation damage due to plugging of pores and pore throats by mud particles. It often triggers other drilling problems that are difficult to control and usually lead to exponential growth of nonproductive time and the unwanted cost. Even a single loss circulation event can lead to a huge monetary loss by triggering a series of other drilling problems that could cost the company millions of dollars[3]. In extreme cases, lost circulation problems may force the abandonment of a well. Therefore, mitigation or elimination of these loss-related drilling problems is very important for safe, economic, and trouble-free drilling operations.

Lost circulation can occur in various formations, such as naturally fractured formations, cavernous formations, and high permeable formations. It can be categorized by the amount of fluid or mud lost as seepage type, moderate type, severe type, and total loss. The extent of the fluid loss and the ability to control the lost circulation with a lost circulation material (LCM) depends on the type of formation in which the lost circulation occurs. Seepage type and moderate type lost circulation may occur in high permeable formations, extremely high permeable formations (referred to as "super-K" formations), and fissured and fractured formations. In addition to the natural causes of lost circulation, subsurface formations having a narrow mud weight window, such as weak and unconsolidated formations, depleted formations, and high-pressure zone formations, may also cause a moderate type to a severe type of lost circulation due to the creation of

induced fractures in the near wellbore formation. Such lost circulation may occur when the mud weight used for well control and borehole stability exceeds the fracture gradient of the formation.

LCMs are used to mitigate the lost circulation by blocking the path of the drilling mud into the formation. The type of LCM used in a lost circulation situation depends on the extent of lost circulation and the type of formation. LCMs may be classified into different categories, such as fibrous materials, flaky materials, granular materials, gel-type materials, cross-linking polymers, and loss control slurries[4, 5]. Such materials are frequently used either alone or in combination to control loss of circulation. The costs incurred in lost circulation situations may be due to lost time, losses of drilling fluids, and losses of production. Existing LCMs may perform poorly in mitigation and the prevention of moderate lost circulation and seepage-type lost circulation, and may not be suitable for controlling several types of lost circulation.

Among the different categories of lost circulation, seepage to moderate loss of circulation is prevalent and failure to act swiftly to combat the loss may eventually lead to several other problems associated with drilling. The materials that are used as a LCM should be able to stop or minimize the losses as quickly as possible. There are different mechanisms to address the lost circulation such as physical ways of minimizing losses utilizing sized particulate materials[6], chemical ways to solve the lost circulation using polymers[7,] or using cement as a LCM[8]. Each approach has its own advantages and disadvantages. Selection of a lost treatment method should be based on several factors, including type of losses, type of loss zone, risk factor, etc.

The global industrial community is marching toward the use of environmentally benign materials, replacing materials that are harmful to humans, environment and aquatic lives in their operations. The oil and gas industry has been adapting to this change and started to implement the regulations instructed by the regional and global environmental protection agencies. Drilling operations significantly depend on numerous chemicals and materials to fulfill various functional tasks at different stages of drilling operations. At most, care has been taken while choosing chemicals and materials for offshore drilling operations to protect aquatic life. Development products from agricultural waste materials that are suitable for drilling fluid application have attracted a lot of research attention[9].

Along this line, in this article we describe the development of a novel eco-friendly fibrous LCM derived from deceased date tree trunks, which is sustainable and available in abundance in the Kingdom of Saudi Arabia. Due to the organic nature of raw materials, the derived mud additives are eco-friendly, nontoxic and biodegradable. Therefore, the plant-based green product will play an important role in protecting the Kingdom's marine environment and will be in the forefront of best drilling practices to protect regional as well as global environments. The lost mitigation performance of the fibrous system has been evaluated by incorporating the fibers in various frequently used water-based drilling fluids and carrying out a pore plugging test (PPT) at high-pressure, high temperature (HPHT) conditions, and the results show that the two-component system is able to seal off 2 mm slotted disks of the PPT. Therefore, it is a suitable system to be used to mitigate moderate losses, thereby enabling an effective solution.

MATERIALS AND METHODS

The eco-friendly fibers of deceased date palm tree trunks has been obtained by the sequence of simple processes. Figure 1 shows the process flow diagram of the collection and processing of deceased date palm tree fibers. Every year, several tons of date trees have been disposed of as waste in Saudi Arabia. In some cases, these waste materials are used to prepare firewood. The majority of these agricultural wastes are available for further application. Therefore, it is inevitable that it is a sustainable source. The trunk part of the disposed date tree has been collected and dried under the sun and in the open air. Chopping off the dried trunk is carried out followed by the cutting of these chopped pieces into small parts. Grinding of these small parts of the trunk will provide fibers having different sizes and aspect ratios, which are sieved and packed according to their size range.

The fibers obtained from the process have been used as a LCM. As the fibers have different aspect ratios, it is hypothesized that a network of fibers would be created at the fracture mouth that would lead to mass buildup and eventually stop or minimize loss of fluid into the fracture. To prove this hypothesis, a PPT apparatus has been used. A 2 mm slotted

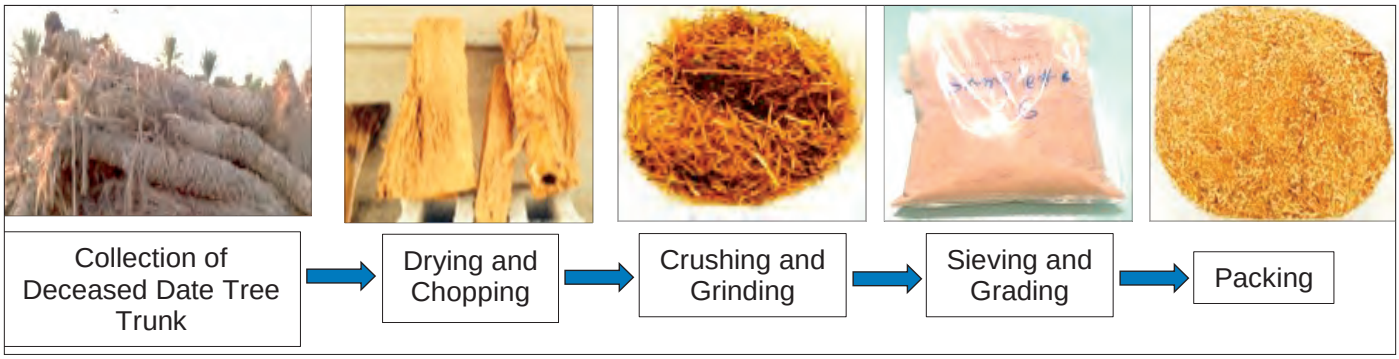

Fig. 1. Process flow diagram of fiber manufacturing from deceased date palm tree trunks.

Mud Components	Gel Polymer Mud
Water (cc)	340.67
Bentonite (g)	25
Caustic Soda (g)	0.25
Soda Ash (g)	0.25

Mud Components	80 pcf NaCl Polymer Mud
Water (cc)	304.64
Caustic Soda (g)	0.25
Soda Ash (g)	0.25
Bentonite (g)	5.00
PAC LV (g)	4.00
XC Polymer (g)	1.00
NaCl (g)	76.16
Barite (g)	57.90

Mud Components	73 pcf KCl Polymer Mud
Water (cc)	310.28
Caustic Soda (g)	0.25
Soda Ash (g)	0.25
Bentonite (g)	5.00
PAC LV (g)	3.00
XC Polymer (g)	1.00
KCl (g)	42.31
$CaCO_3$ (g)	46.80

Mud Components	90 pcf $CaCl_2$ Polymer Mud
Water (cc)	294.87
Bentonite (g)	5.00
PAC LV (g)	3.00
XC Polymer (g)	1.00
$CaCl_2$ (g)	126.37
Lime (g)	0.50
Barite (g)	74.60

Table 1. Formulation of different drilling fluid systems

disk has been used to simulate fractures with a width of 2 mm. Depending on the type of formation drilled, there are a few types of water-based drilling fluids used frequently during drilling, namely 65 pcf of gel (bentonite) polymer mud, 73 pcf of potassium chloride (KCl) polymer mud, 80 pcf of sodium chloride (NaCl) polymer mud, and 90 pcf of calcium chloride ($CaCl_2$) polymer mud. The selection of these mud systems is based on chemical characteristics of the muds having monovalent and di-valent cations and varying density of the mud. It is highly necessary to ensure the compatibility of the eco-friendly fibers in these mud systems and make sure that the fibers not only provide lost circulation but also do not alter the basic properties of the mud. As the fiber is chemically inert to most of the additives incorporated in the formulation, and the mechanism of lost mitigation is a physical process, it is expected that the fiber would not significantly alter the properties of the mud. Formulation of these mud systems are given in Table 1. These are regular and routinely used formulations.

RESULTS AND DISCUSSIONS

The fibrous LCM developed from deceased date tree trunks has been characterized for its sealing efficiency by PPT under HPHT conditions as explained next.

PPT: A PPT is the industry standard test for validating LCMs, and unlike in other methods, this test excludes the effect of gravity by having pressure inlets at the bottom of the cell and the outlet is at the top. Hydraulic oil is used to apply pressure for the test. There are slotted disks with different slot widths, such as 1 mm and 2 mm, used as a filter medium. This is to simulate fractures with widths of 1 mm to 2 mm in the loss zone. A good LCM will seal off the slots of the disk, thereby preventing fluid from passing through the slot. Tests can be carried out at elevated temperatures as well as to better simulate the field conditions. A PPT apparatus as shown in Fig. 2 has been used to conduct tests at a temperature of 250 °F and a differential pressure of 1,500 psi. A 2 mm slotted disk has been used during the test as a filter medium simulating fractures in the moderate loss zone. The tests have been carried out for 30 minutes as an industry standard.

Screening of Fiber Concentration: Initial screening of the fiber concentration has been carried out by preparing a lost circulation slurry for each mud by incorporating 10 pounds per barrel (ppb) of date tree fibers. The test has been conducted at a temperature of 250 °F and an overburden pressure of 1,500 psi. The results of the initial screening are given in Table 2.

It is evident from the results of the initial screening

Fig. 2. PPT.

Mud System	Fiber Concentration	Spurt Loss (cc)	Fluid Loss (cc)	Total Leakoff (cc)	Cake Thickness (mm)	PPT Value (cc)
65 pcf Gel Polymer Mud	10 ppb	0	0	0	12.7	0
73 pcf KCl Polymer Mud	10 ppb	2	3	5	14	10
80 pcf NaCl Polymer Mud	10 ppb	3	7	10	13	20
90 pcf $CaCl_2$ Polymer Mud	10 ppb	2	4	6	12	12

Table 2. PPT carried out at 250 °F and an overburden pressure of 1,500 psi, using a 2 mm slotted disk on a fiber concentration of 10 ppb

Mud System	Fiber Concentration	Spurt Loss (cc)	Fluid Loss (cc)	Total Leakoff (cc)	Cake Thickness (mm)	PPT Value (cc)
65 pcf Gel Polymer Mud	30 ppb	0	0	0	29	0
73 pcf KCl Polymer Mud	30 ppb	0	0	0	21	0
80 pcf NaCl Polymer Mud	30 ppb	0	0	0	19	0
90 pcf $CaCl_2$ Polymer Mud	30 ppb	0	0	0	21	0

Table 3. PPT carried out at 250 °F and an overburden pressure of 1,500 psi, using a 2 mm slotted disk on a fiber concentration of 30 ppb

Mud System	Fiber Type	Fiber Concentration	Spurt Loss (cc)	Fluid Loss (cc)	Total Leakoff (cc)	Cake Thickness (mm)	PPT Value (cc)
65 pcf Gel Polymer Mud	Commercial Fiber	30 ppb	0.7	16	16.7	3.97	33.4
73 pcf KCl Polymer Mud	Commercial Fiber	30 ppb	0.7	16	16.7	3.97	33.4
80 pcf NaCl Polymer Mud	Commercial Fiber	30 ppb	0.7	16	16.7	3.97	33.4
90 pcf $CaCl_2$ Polymer Mud	Commercial Fiber	30 ppb	0.7	16	16.7	3.97	33.4

Table 4. PPT carried out at 250 °F and an overburden pressure of 1,500 psi, using a 2 mm slotted disk on a commercial fiber concentration of 30 ppb

that the fiber is very effective in controlling the loss of fluid through a 2 mm slotted disk, even at elevated temperature and pressure conditions. The fiber is most effective in the case of gel polymer mud as no loss of fluid is observed. For the other three mud systems, a very small amount of fluid loss is observed, which is less than 5% of the volume of the mud used for the experiment. The thickness of the mud cake supports the hypothesis that the fibers would form a network that will lead to the accumulation of mass at the mouth of the fracture and eventually stop or minimize loss of fluid through the fracture.

To find out the maximum concentration of fibrous LCM required to stop any fluid loss through the slotted disk, the concentration of the fiber has been increased from 10 ppb to 30 ppb and the PPTs have been carried out at similar conditions, and the results are shown in Table 3. A total seal-off has been achieved with 30 ppb fibers, and as a result, no fluid loss is observed for all four mud systems used for the experiment. Therefore, it is recommended that 30 ppb of the fibrous material be used in the lost circulation slurry to have effective mitigation.

Comparison with Commercial Fibrous LCM: The performance of date tree trunk-based fiber is benchmarked against a similar commercially available biodegradable fibrous LCM that is widely used in Saudi Aramco drilling operations. The PPTs have been carried out using a LCM slurry prepared from four different types of mud incorporated with 30 ppb of commercial fiber. The tests have been conducted at the same experimental conditions followed for date palm tree fiber and the results of the experiments are tabulated in Table 4.

The results show that although the commercial fiber is capable of controlling loss of fluid, around 10% of the total volume of the fluid has been lost through the slotted disk. This is almost twice the amount of fluid lost while using only 10 ppb of date tree trunk fiber, and for the same concentrations

of date tree fiber (30 ppb) no fluid loss has been observed. It is evident that the fibers of the date palm tree trunk outperforms commercially available counterparts widely used in the industry. Therefore, the organic, nontoxic, eco-friendly, biodegradable fiber obtained from deceased date palm tree trunks is a suitable product to be used for the application as a fibrous LCM to mitigate moderate types of losses.

CONCLUSIONS

In summary, a novel eco-friendly, nontoxic, and biodegradable fibrous LCM has been developed from deceased date palm tree trunks. The manufacturing process of a fibrous product has been demonstrated involving the collection, drying, chopping, grinding, and sieving steps. Lost circulation slurry has been prepared by incorporating fibers into various commonly used mud formulations to show the compatibility of these fibers with different mud systems. The sealing efficiency of the fibrous lost circulation system has been proven by conducting PPTs using 2 mm slotted disks carried out at HPHT conditions to simulate downhole conditions. A comparative study on the sealing efficiency of the commercially available LCM has been carried out under similar experimental conditions, and it has been confirmed that the date palm tree trunk fiber developed in this study shows superior performance in terms of effectively sealing a 2 mm slotted disk. Therefore, the date palm tree trunk fibers have the potential to mitigate moderate types of losses encountered while drilling.

ACKNOWLEDGMENTS

The authors would like to thank the management of Saudi Aramco for their support and permission to publish this article.

This article was presented at the SPE Kingdom of Saudi Arabia Annual Technical Symposium and Exhibition, Dammam, Saudi Arabia, April 24-27, 2017.

REFERENCES

1. Economides, M.J., Watters, L.T. and Dunn-Norman, S.: *Petroleum Well Construction, Chapter 5*, John Wiley and Sons, New York, 1998, 640 p.
2. Bruton, J.R., Ivan, C.D. and Heinz, T.J.: "Lost Circulation Control: Evolving Techniques and Strategies to Reduce Downhole Mud Losses," SPE paper 67735, presented at the SPE/IADC Drilling Conference, Amsterdam, The Netherlands, February 27-March 1, 2001.
3. Kumar, A. and Savari, S.: "Loss Circulation Control and Wellbore Strengthening: Looking beyond Particle Size Distribution," paper AADE-11-NTCE-21, presented at the American Association of Drilling Engineers National Technical Conference and Exhibition, Houston, Texas, April 12-14, 2011.
4. White, R.J.: "Lost Circulation Materials and their Evaluations," API paper 56-352, presented at the Drilling and Production Practice, New York, New York, January 1, 1956.
5. Whitfill, D.: "Lost Circulation Materials Selection, Particle Size Distribution and Fracture Modeling with Fracture Simulation Software," SPE paper 115039, presented at the IADC/SPE Asia Pacific Drilling Technology Conference and Exhibition, Jakarta, Indonesia, August 25-27, 2008.
6. Amanullah, M.: "Characteristics, Behavior and Performance of ARC Plug — A Date Seed-Based Sized Particulate LCM," SPE paper 182840, presented at the SPE Annual Technical Symposium and Exhibition, Dammam, Saudi Arabia, April 25-28, 2016.
7. Boukadi, F., Yaghi, B., Al-Hadrami, H., Bemani, A., et al.: "A Comparative Study of Lost Circulation Materials," *Energy Sources*, Vol. 26, Issue 11, 2004, pp. 1043-1051.
8. Fidan, E., Babadagli, T. and Kuru, E.: "Use of Cement as Lost Circulation Material — Field Case Studies," SPE paper 88005, presented at the IADC/SPE Asia Pacific Drilling Technology Conference and Exhibition, Kuala Lumpur, Malaysia, September 13-15, 2004.
9. Amanullah, M., Ramasamy, J. and Al-Arfaj, M.K.: "Application of an Indigenous Eco-friendly Raw Material Fluid Loss Additive," *Journal of Petroleum Science and Engineering*, Vol. 139, March 2016, pp. 191-197.

BIOGRAPHIES

Dr. Jothibasu Ramasamy is a Petroleum Scientist working with the Drilling Technology Team of Saudi Aramco's Exploration and Petroleum Engineering Center – Advanced Research Center (EXPEC ARC). He joined Saudi Aramco in July 2013. Prior to this, he worked as a Research Fellow with the Department of Chemistry at the National University of Singapore and as a Postdoctoral Fellow with the Catalysis Center at the King Abdullah University of Science and Technology (KAUST), Saudi Arabia.

Jothibasu received his B.S. degree in Chemistry from Bharathidasan University, Tiruchirappalli, India, and his M.S. degree, also in Chemistry, from Anna University, Chennai, India. In 2010, he received his Ph.D. degree in Chemistry from the National University of Singapore, Singapore.

Jothibasu has published 15 technical papers and filed three patents.

Dr. Md. Amanullah is a Senior Petroleum Engineering Consultant working at Saudi Aramco's Exploration and Petroleum Engineering Center – Advanced Research Center (EXPEC ARC). Prior to joining Saudi Aramco, he worked as a Principal Research Scientist at CSIRO in Australia.

Aman is the lead inventor of a vegetable oil-based dielectric fluid (patented) that led to the formation of a spinoff company in Australia for commercialization of the product.

He has published more than 85 technical papers and filed 43 patents, with 10 already granted. Two of Aman's patents were highlighted in scholarly editions of two books published in the U.S.

He is one of the recipients of the 2005 Green Chemistry Challenge Award from the Royal Australian Chemical Institute. Aman also received the CSIRO Performance Cash Reward in 2006, the Saudi Aramco Mentorship Award in 2008 and 2010, the World Oil Certificate Award for nano-based drilling fluid development in 2009, the Intellectual Asset Recognition Award in 2014, and the Award of Recognition for Outstanding Contribution to the success of agricultural waste and environmental protection in 2014. His date tree waste-based product development was highlighted in *The Arabian Sun*, the *Arab News* and also in the Al Riyadh newspaper.

Aman is a member of the Society of Petroleum Engineers (SPE). He received the SPE Regional Service Award in 2014 and also SPE Middle East Drilling Engineering Award in 2016 for his contribution to the industry.

Aman received his M.S. degree (First Class) in Mechanical Engineering from the Moscow Oil and Gas Institute, Moscow, Russia, and his Ph.D. degree in Petroleum Engineering from Imperial College, London, U.K.

Successful Use of Downhole Camera Technology to Assist Fishing Operations

Nasser M. Al-Hajri, Hussain A. Al-Quwaisim, and Rashad M. Al-Zahrani

ABSTRACT

Fishing operations are complex and time-consuming. This is due to the associated uncertainty with the orientation and condition of the tool that requires fishing. In this article, a case study, which demonstrates the usefulness of utilizing downhole camera technology in conjunction with fishing operations is presented. The use of real-time camera inspection enabled the successful fishing of a challenging plug. In addition, the traditional trial and error approach used in most fishing operations was avoided, reducing the operation time and cost.

The article's case study is a high-pressure oil producer that has a stuck retrievable plug at 200 ft. The presence of the fish at a shallow depth makes well intervention operations critical from well control perspectives. In such cases, fishing operations must be meticulously designed to account and plan for contingencies, should complications arise during fishing. Attempts to fish the plug using a normal and heavy-duty slick line were not successful. During these fishing attempts, several tools were lost in the hole due to the damaged nature of the stuck plug, adding to the complexity of the fishing operation.

To address this challenge, a downhole camera with real-time data transmission capability was run in the well using coiled tubing (CT) to enable viewing the condition and orientation of the lost fishing tools and the stuck plug. The results of the camera inspection runs were instrumental in subsequent fishing tool selection and adjusting the operating procedures. The first camera run revealed the presence of metal objects obstructing the proper latch to the fish neck. Following cleanup runs with a magnet, the second camera inspection run clearly showed partial damage to the top of the fish neck — a chipped out metal piece. The rest of the fish neck was found intact.

Given the nature of damage to the top of the fish neck, conventional fishing tool sizes — 3" — were not able to latch onto the fish. Accordingly, a smaller fishing tool — 1.26" spear — was run and latched inside the bottom of the fish neck instead of the damaged top. The 1.26" spear run was successful in latching inside the fish neck and in safely recovering the fish. The fishing operation design, job execution, and contingencies will all be discussed in this article.

INTRODUCTION

Fishing is a common well intervention operation. Hilts et al. (1993)[1] defined fishing as "an attempt to engage and retrieve unwanted, unserviceable, or often damaged equipment from a wellbore." Fishing can be performed using drillpipe, coiled tubing (CT), or wireline. In a typical fishing job, the orien-

Accessory Sketch	Label	Accessory Description	Top Depth (ft)	Length (ft)	ID (in.)
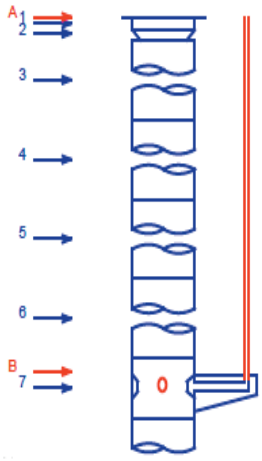	1	Tubing Hanger	23.8	0.92	4.5
	A	SSSV/Monel Control Line	23.8	252.17	N/A
	2	Double Pin Sub	24.72	1.35	3.972
	3	(2) EA Tubing Joints	26.07	76.6	4
	4	Pup Joint	102.67	10.05	4
	5	(4) EA Tubing Joints	112.72	155.16	4
	6	Pup Joint	267.88	6.15	4
	7	SSSV Nipple	274.03	3.88	3.813
	B	SSSV	274.03	1	3.813

Table 1. Uppermost completion diagram of Well-A

tation and condition of the tool that requires fishing are unknown. Fishing is also a complex well intervention operation. The complexity of fishing operations stems from the variety of options that can be used to fish any given tool[2]. Given the uncertainty and complexity associated with fishing, most operation strategies are devised in a manner that minimize economic losses[3].

Downhole video camera inspections have been in use for a long time in the industry. Applications of such inspections include measurements of induced fractures[4] and well integrity diagnostics[5, 6].

In this article, we will present the advantage of using downhole cameras alongside fishing operations. This unique application of a downhole camera provides additional and more certain inputs that aid the fishing operation design.

CASE STUDY BACKGROUND

The case study of this article, Well-A, is an oil producer. The well was completed with 4½" tubing and a wireline retrievable subsurface safety valve (SSSV). The completion diagram of Well-A, along with an accessory description — which is relevant to this article — can be seen in Table 1.

During normal operation of Well-A, it was necessary to install a slick line conveyed retrievable bridge plug inside the well tubing to carry out repair and maintenance activities on the wellhead. After setting the bridge plug at 200 ft and while pulling out of hole (POOH), human error had caused the slick line drum brakes not to lock, which resulted in having the drum suddenly rolling downwards. Consequently, the equalizing prong, which is used to set the bridge plug, hit the top of the plug at 200 ft and broke the prong.

PREVIOUS FISHING ATTEMPTS

Prior to fishing, Well-A was killed with the appropriate weight and volume to facilitate a safe well intervention operation. Several fishing attempts of the lost tools were made. These attempts can be categorized into attempts with a normal slick line and attempts with a heavy-duty fishing slick line.

Fishing with a Normal Slick Line

Fishing was commenced by running different sizes of a lead impression block (LIB). The LIB is typically lowered sharply onto a fish so the lead molds to the shape or condition of the fish neck[7]. A total of three LIBs were run with sizes equal to 2¼", 3½", and 3.78". The LIB runs identified that the setting prong is located inside the plug lock mandrel leaning to the side. Figure 1 shows the LIB marks collected from the fish inside Well-A.

Subsequent fishing using an overshot tool was able to retrieve the equalizing prong used to set the plug. The equalizing prong was found broken from downward impact when

Fig. 1. Photos of the three different LIBs that were run in Well-A, showing different marks on top.

hitting the top of the retrievable bridge plug. Figure 2 shows photos of the recovered broken prong.

After retrieving the equalizing prong, multiple attempts were made to retrieve the bridge plug using catch tools such as overshot, magnets, and wireline pulling tools; however, these attempts were not successful. In addition, many of these pulling tools were found broken or had missing pieces when retrieved to the surface. The failure of common fishing tools to retrieve the bridge plug indicates that the plug was stuck inside the tubing and prompted the design of a special fishing tool. A normal wireline pulling tool that engages a fish internally was modified by welding latching dogs (or teeth) around the pulling tool. The objective from such a design was to centralize the pulling tool around the fish neck and facilitate retrieval; however, this tool was unable to retrieve the plug after latching. In fact, the modified tool itself got stuck on top of the bridge plug and was released — leaving it in the hole.

Fishing with a Heavy-Duty Slick Line

Given the unsuccessful attempts of a normal slick line to retrieve the plug, a heavy-duty slick line unit was mobilized to the well. Fishing, by using heavy-duty slick line units, differs from normal fishing by the ability to carry out heavier weights and provide more impact force when jarring is required. Heavy-duty fishing commenced by running a LIB to confirm a clean fish neck of the modified pulling tool left in the hole by a normal slick line fishing attempt, after which two runs of heavy jarring with wireline pulling tools were made. The jarring force trip was set at 2,000 lbf. The modified pulling

Fig. 2. Photos of the recovered broken prong.

Fig. 3. Photos of the recovered modified pulling tool.

tool was recovered after several upward jarring attempts. The recovered tool was found to have one latch dog missing and scarring was noticed on the pulling tool, reaffirming the presence of foreign objects left from the normal slick line fishing attempts. Figure 3 shows photos of the recovered modified pulling tool.

Several other attempts were made with a heavy-duty fishing slick line. These attempts used a variety of techniques such as changing the slick line wire, shortening the core of the pulling tool, use of a blind-box to move the stuck plug downward, and use of a non-releasable spear. None of these techniques was fruitful in engaging and retrieving the fish.

CT FISHING WITH CAMERA TECHNOLOGY

In this section, we discuss the operational design and field execution of the fishing attempt that had led to the successful retrieval of the plug from Well-A.

Job Planning

Before designing the next fishing attempt, a thorough review of previous attempts is necessary to analyze events and draw proper conclusions. The lessons learned from previous fishing attempts can then be used to adopt a new fishing approach and execute subsequent operations.

Analysis of Previous Fishing Attempts. There are key findings, which were identified from analyzing the previous fishing attempts:

- Given that a variety of common well intervention tools were not able to latch onto the plug, it was concluded that the fish neck of the plug in Well-A was obstructed. This finding is supported by many field observations where the fishing tools were either missing metal parts or were heavily scratched after engaging the downhole fish.
- The attempt to move the plug in Well-A downward using a blind-box conveyed via a heavy-duty slick line was not successful, even though a large number of forceful downward jarring actions were applied. This suggests that the plug in Well-A is stuck or jammed in the tubing.

Newly Adopted Fishing Approach. Based on the findings drawn from previous fishing attempts, a new fishing approach, consisting of the use of CT and downhole camera technology, was adopted. Using a CT-converyed downhole camera will enable pumping on top of the fish and capturing the condition and orientation of the fish in real time. As such, the proper fishing tool selection can be made. The use of a downhole camera is proven to be more reliable than indications obtained by the LIB. The use of a LIB failed to provide required insights with respect to the lost fishing tools. In addition, given the stuck nature of the plug in Well-A, CT would provide more pulling force compared to the slick line option.

Operational Design. The design for well intervention using CT and a downhole camera consisted of the following operational sequence:

1. Perform a CT clean out run using a burn shoe and junk basket to condition the well and remove any particles that were left in the hole from the previous slick line fishing attempts. These particles could obstruct the camera's view as well.
2. Run a downhole camera with real-time inspection capability to the top of the plug. The objective of this run is to view the condition and orientation of the lost wireline tools and the stuck plug.
3. Run the appropriate fishing tool based on the findings of the downhole camera. Fishing tool selection includes magnets, spears, an internal pulling tool, and the contingency use of an impact force hammer. A camera can be run again based on the recovery and progress of the fishing operation.

Proactive measures to account for possible stuck fish across the wellhead valves were made. These measures include repeatedly reciprocating the CT plug 20 ft below the wellhead to ensure that the plug elastomers are deflated. Also, two gate valves were mounted on a 6 ft riser that was installed on top of the wellhead. This operational rig up was necessary to accommodate the bottom-hole assembly (BHA) and fish lengths when POOH, should additional surface control barriers, i.e., the two gate valves, be needed as a contingency from well control perspectives.

Job Execution

Clean out Run. The CT operation commenced by running a clean out BHA, consisting primarily of a burn shoe and junk

Fig. 4. A photo of the recovered latching dog.

basket with other associated running tools. The tools were run in hole (RIH) without pumping to gently tag the top of the fish. Performing a downward clean out run was not preferred to avoid accumulating debris or junk on the top of the fish. As such, the BHA was picked up 10 ft and clean out was performed while POOH, with pumping water used as a circulation fluid. The result of this clean out run was retrieving a latching dog (or teeth) that was part of the modified internal fishing tool used in the normal slick line operation. Figure 4 shows a photo of the recovered latching dog.

First Camera Inspection. Prior to the camera run, the CT riser was flushed to remove any grease and other contaminations that could obstruct the camera view. A water tank was made available to be used to clear downhole visuals when needed. The camera was RIH to 160 ft, then pumping of clear water was started. The pumping rates were increased gradually from 0.5 barrels per minute (bpm) to 2.0 bpm to clear contamination on the camera dome from wellbore fluids. Foreign metal objects were found at a depth of 198.5 ft. No clear view of the plug was obtained given the obstructing objects. Figure 5 compares downhole camera images with the actual recovered tools.

Magnets Fishing Runs. Based on the obtained images from the camera run, the foreign metal objects appear to be of irregular shape and would not be normally retrieved using common pulling tools. The many unsuccessful slick line fishing attempts attest to this fact. As such, it was decided to run magnets to recover the lost tools. Fishing with magnets capitalizes on the attraction to metals and would not require the shape of the fishing tool to match the fish profile. Different sizes of magnets — 3.5" and 2.7" — were run and recovery of the metal objects was made. The frequency of magnets run was decided on a common oil field rule of thumb that suggests continuing to fish with magnets until no further recovery is made.

Fishing with Common Pulling Tools. Once the magnet runs ceased to retrieve additional objects from the well, it was decided to run common pulling tools to engage and retrieve the fish. Multiple runs with the internal fishing tool and spear — both 2.7" in size — did not latch onto the fish. In total, three attempts were made, one with the spear and the other two with an internal fishing tool.

Second Camera Inspection. Based on the lack of progress obtained by the previous operational step, it was decided to run a second camera inspection. The rationale behind running the camera for a second time is to obtain images of the stuck plug

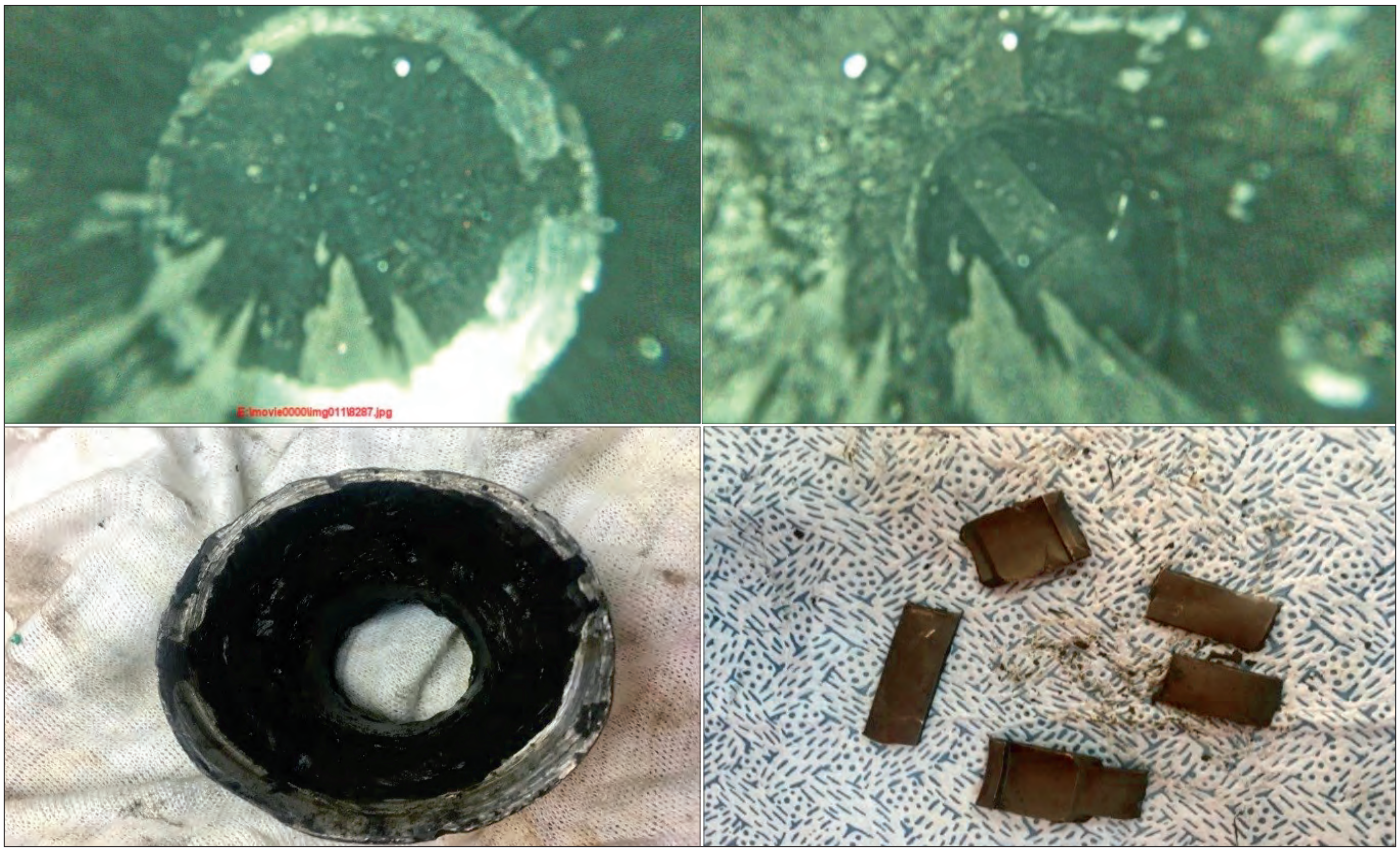

Fig. 5. Comparison between camera images (top) and actual recovered tools (bottom).

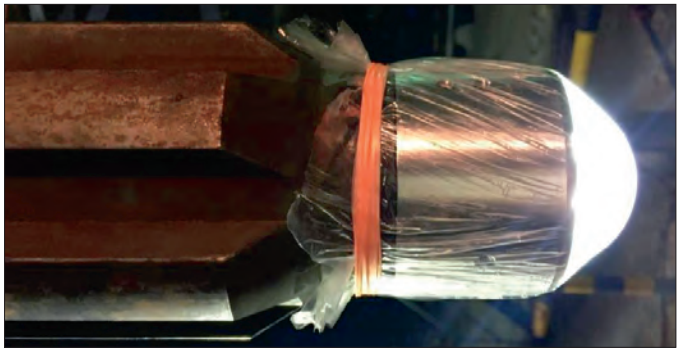

Fig. 6. The water dissolvable bag mounted on the downhole camera.

fish neck itself since all foreign objects were already fished out.

A water dissolvable bag, Fig. 6, was mounted on the downhole camera dome to avoid the wellbore fluid contamination encountered during the first camera inspection run. The camera was RIH to 170 ft and pumping water started with 0.5 bpm. The downhole visual conditions had gotten worse compared to the previous run, therefore, the pumping rate was increased to 2.0 bpm.

Clear images of the plug fish neck were obtained from this second camera inspection. The top of the fish neck was observed at 199.5 ft with a partially parted neck top. Deeper camera inspections were made by tagging the camera on the fish neck. The continuous pictures show a chipped out piece, extending from the fish neck, top to bottom. Figure 7 compares the actual fish neck pictures with downhole images recorded by the camera.

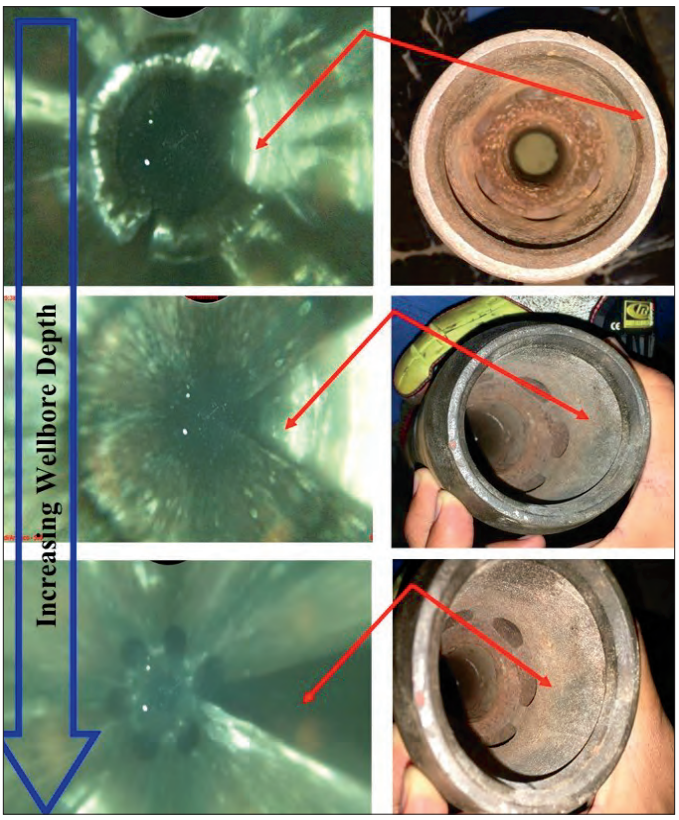

Fig. 7. Comparison between downhole images and the normal plug fish neck.

Fishing with a Small Spear. The findings of downhole images suggest that a normally sized — 2.7" — pulling tool cannot latch onto the fish given the damaged nature of the fish neck top. As stated earlier, multiple runs were made using these tools and could not engage the fish. Accordingly, a small fishing spear — ranging from 1.70" to 1.74" in size — was chosen for this run. This tool selection is planned at engaging the bottom of the plug fish neck in Well-A that is still intact.

The small spear run was successful in engaging the fish from the CT weight indications. An overpull was also noticed while POOH. The CT was reciprocated before arriving to the surface as stipulated in the operational job design and full plug recovery was made. Figure 8 shows photos of the stuck plug from Well-A at the surface upon recovery. The damage to the top of the fish neck (circled) can be seen as suggested by the downhole camera.

CONCLUSIONS AND RECOMMENDATIONS

The use of a downhole camera in conjunction with fishing was proven successful. The challenging case study of the stuck plug in Well-A demonstrates this fact. In cases similar to Well-A, the following is recommended:

1. Perform initial fishing attempts with slick line units — either normal or heavy-duty — as they are more cost-effective than the CT option.
2. Use fishing magnets whenever normal pulling tools cannot engage the fish. Magnets have the ability to retrieve objects of irregular shape and facilitate subsequent fishing with the normal tools.
3. Run cameras downhole to investigate condition and orientation of any fish neck. Selection of the appropriate

Fig. 8. Photos of the stuck plug from Well-A at the surface upon recovery.

fishing tool can be made based on the findings of the camera images.

ACKNOWLEDGMENTS

The authors would like to thank the management of Saudi Aramco for their support and permission to publish this article.

This article was presented at the Abu Dhabi International Petroleum Exhibition and Conference, Abu Dhabi, UAE, November 13-16, 2017.

REFERENCES

1. Hilts, R.L., Fowler Jr., S.H. and Pleasants, C.W.: "Fishing with Coiled Tubing," SPE paper 25499, presented at the SPE Production Operations Symposium, Oklahoma City, Oklahoma, March 21-23, 1993.
2. Walker, G.: "Fishing," SPE paper 13360, presented at the SPE Eastern Regional Meeting, Charleston, West Virginia, October 31-November 2, 1984.
3. Harrison, C.G.: "Fishing Decisions under Uncertainty," *Journal of Petroleum Technology*, Vol. 34, Issue 2, February 1982, pp. 299-300.
4. Palmer, I.D. and Sparks, D.P.: "Measurement of Induced Fractures by Downhole TV Camera in Black Warrior Basin Coalbeds," *Journal of Petroleum Technology*, Vol. 43, Issue 3, March 1991, pp. 270-328.
5. Al-Hajri, N.M., Al-Ajmi, M.D., Al-Subaie, F.M., Hognestad, A., et al.: "Real-Time Well Integrity Diagnostics Using the Latest Developments in Visual Logging Technology; a Case Study," SPE paper 182804, presented at the SPE Kingdom of Saudi Arabia Annual Technical Symposium and Exhibition, Dammam, Saudi Arabia, April 25-28, 2016.
6. Al-Zain, A., Al-Mulhim, A., Al-Subaie, F.M., Al-Jandal, A., et al.: "Well Integrity Assessment Using Video Camera Technology — Case Histories," SPE paper 182952, presented at the Abu Dhabi International Petroleum Exhibition and Conference, Abu Dhabi, UAE, November 7-10, 2016.
7. Spannuth, M., Achihai, R., Gonzalez Campos, J.A., Husvaeg, M.A., et al.: "Improving Intervention Efficiency with a Novel X-ray Diagnostic Service: A Case Study," SPE paper 184798, presented at the SPE/ICoTA Coiled Tubing and Well Intervention Conference and Exhibition, Houston, Texas, March 21-22, 2017.

BIOGRAPHIES

Nasser M. Al-Hajri joined Saudi Aramco in 2013 and currently works as a Senior Engineer in the North Ghawar Production Engineering Division. He has 29 published technical papers and seven filed U.S. patents to his name.

In 2013, he received his B.S. degree in Petroleum Engineering from King Fahd University of Petroleum and Minerals (KFUPM), Dhahran, Saudi Arabia, and in 2017, he received his M.S. degree in Petroleum Engineering, also from KFUPM.

Hussain A. Al-Quwaisim joined Saudi Aramco in 2004 as a Well Intervention Specialist, working in the Southern Area Production Engineering Department. Since then, he has mainly worked as a Senior Production Engineer in the North Ghawar Production Engineering Division. In addition to his work in production engineering, Hussain's experience includes working as a Workover Engineer, Well Services Engineer, Gas Well Completion Site Foreman, and Well Completion Engineer.

In 2004, he received his B.S. degree in Petroleum Engineering from King Fahd University of Petroleum and Minerals (KFUPM), Dhahran, Saudi Arabia.

Rashad M. Al-Zahrani joined Saudi Aramco in 2005 as a Petroleum Engineer, and works in the Southern Area Production Engineering Department. He has more than 12 years of experience in oil and gas wells production engineering and well completion operations. Rashad is currently the Production Engineering Supervisor of the Abqaiq and Dammam fields.

He is an active member of the Society of Petroleum Engineers (SPE) and served as the membership Vice Chairperson for the SPE Saudi Arabia Section during 2012-2013. Rashad has published several technical papers and articles.

In 2005, he received his B.S. degree in Petroleum Engineering from the University of Kansas, Lawrence, KS, and in 2011, Rashad received his M.S. degree in Petroleum Engineering from Texas A&M University, College Station, TX, specializing in DTS applications to allocate production from multilateral wells.

First Multilateral Well Worldwide with an Intelligent Completion System and Open Hole Acid Stimulation

Sofiri Hart and Hatem M. Saggaf

ABSTRACT

The Middle East has long been a pioneer in innovation in drilling and completion technologies for multilateral wells. It was here that the first[1] multilateral tool (MLT) on coiled tubing (CT) was used to access and stimulate each open hole lateral in a trilateral well. Over the years, several[2-4] applications of this and similar technologies have been made. In each instance, a conventional upper completion system was installed.

In a multilateral well with a conventional upper completion and an open hole lower completion, there is no independent flow control from each lateral. Because of this, production is not optimized to account for differences in the production rate or reservoir quality of each lateral. For a well with an upper intelligent completion system (ICS), independent control of flow from each lateral is possible through the use of surface controlled flow control valves (FCVs). This feature addresses the shortcomings of the conventional upper completion previously mentioned.

The challenge in performing an acid stimulation of each open hole lateral in a well with an ICS is the inability to access any of the laterals after the ICS has been installed. Current technologies do not afford this option, and designs in the pipeline do not have field proven applications.

This article chronicles a novel attempt at acid stimulating each open hole lateral of a trilateral well in a carbonate reservoir. It includes the installation of the ICS in the same well. The challenges, results, learnings, and future courses of action are documented in what should provide a template for continuous improvement.

INTRODUCTION

A typical single lateral well in the field of interest consists of conductor, surface, and intermediate casing strings. After the intermediate string is run and cemented, the next hole section is drilled to the reservoir target entry point where the reservoir is confirmed. The production casing is then run and cemented and the reservoir section drilled. A polymer water-base drill-in fluid with calcium carbonate as its weighting agent is used to drill this horizontal section across the carbonate reservoir to the well's total depth (TD). Following the completion of drilling activity, the drill-in fluid is displaced to brine with brine selection based on anticipated reservoir pressures. For wells targeting this reservoir, calcium chloride ($CaCl_2$) brine is used. After displacing the reservoir section to brine, it is completed open hole with acidic brine (hydrochloric (HCl) acid with a brine base). The acidic brine is spotted across the reservoir for filter cake removal and reservoir stimulation.

For the candidate well, Fig. 1, delivery requirements dictated that the well be a multilateral well. The challenge to this objective was how to deal with the resulting fluid loss upon removal of the filter cake with acidic brine. For similar multilateral wells in the past, this challenge was addressed by installing the upper completion before the stimulation treatment was done. The shortcoming to this completion design was that since access to the upper laterals was not possible after installation of the intelligent completion system (ICS), only the motherbore received the requisite stimulation treatment. Bullheading the acid treatment through the flow control valves (FCVs) in the ICS was not a desirable option. This was because such treatments tended to preferentially go to the open hole section closest to the FCV. The result of this was that the rest of the lateral was left untreated.

With the limitation posed by installing the upper completion, the completion program design for the candidate well was predicated on delivering the stimulation treatment before the upper completion was installed. Inherent in this design was a means to addressing the fluid loss challenge previously mentioned. In broad strokes, the outline for the completion program for the candidate well was as follows:

1. Drill and spot $CaCl_2$ brine in all laterals.
2. Perform a wellbore clean out of the production casing.

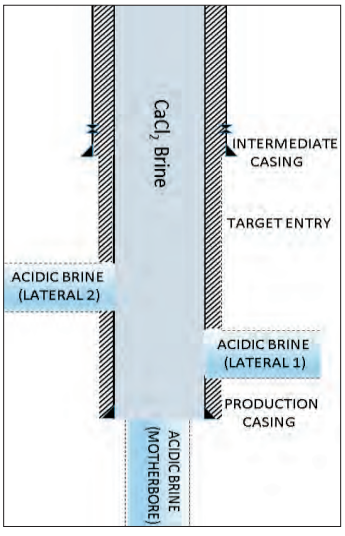

Fig. 1. Initial proposal for candidate well (pre-ICS installation).

3. Access and deploy acid treatment, isolating each lateral after spotting treatment.
4. Run the ICS.

The following sections detail the design process for delivering the objectives for the candidate well. Most of the focus of this article will be on the access and deployment of the acid treatment and the subsequent lateral isolation after each treatment.

DESIGN FOR LATERAL ACCESS

The plan for access to, and deployment of, the acid treatment in each lateral, was tailor-made for the fiber optic enabled coiled tubing (CT) multilateral tool (MLT). Following the first worldwide application described in detail[1], use of this technology has become more commonplace[2-4]. The MLT is basically a flow activated bent sub that is run on fiber optic connected CT (e-coil). Using hydraulic pressure trends, confirmation of the alignment of the MLT with the window of interest is made. Afterward, casing collar locator (CCL) correlations and gamma ray signatures are used to confirm the identity of the lateral, as the MLT is run through the window into the lateral of interest.

Getting the MLT to TD of each lateral was a requirement for the stimulation program. To ensure that this was achieved, a simulation of the reach of the e-coil was undertaken. Although the directional trajectory, e-coil size, and friction reducing agent impacted the reach of the e-coil, the wellbore configuration proved critical to getting the e-coil to the TD of each lateral. This was because the helical tendency of the e-coil was exarcerbated inside the much larger production casing, resulting in the lockup of the e-coil — shallower than the TD of the lateral. To prevent this from happening, the drillpipe used by the rig was run in the model as the conduit for the e-coil. Its footage was limited to 100 ft from the window to the uppermost lateral. The more restrictive inside diameter (ID) of the drillpipe workstring allowed the e-coil to reach TD of each lateral before lockup.

Figure 2 illustrates the additional footage achieved by running the e-coil through the drillpipe compared to not doing so. This incremental footage was in excess of 2,000 ft.

Another modification had to be made to the wellbore configuration prior to the MLT run. Anticipated circulating pressures from pumping through restrictive IDs in the MLT necessitated that flow rates for the treatment be limited to a few barrels per minute. With the wellbore volume in excess of several hundred barrels, resulting circulating times proved prohibitive. Having a packer at the end of the workstring simplified the wellbore configuration and reduced circulating volumes, and associated times by more than 50%. Figure 3 illustrates the final wellbore configuration and outlines the sequence of the MLT access to each lateral.

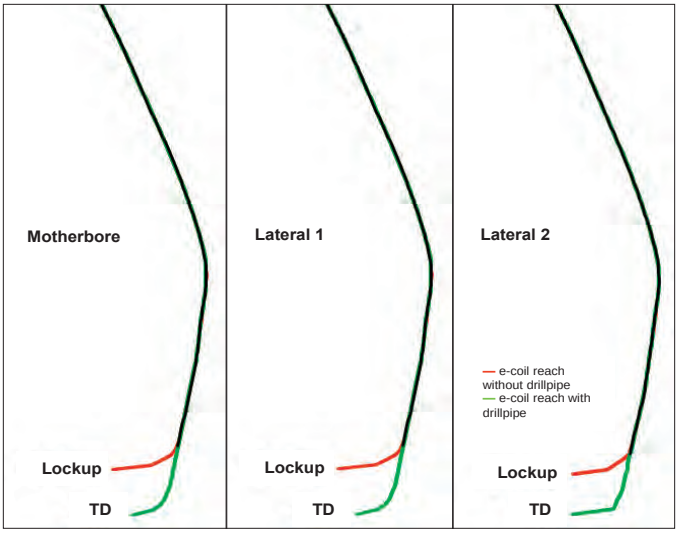

Fig. 2. E-coil reach (depth vs. e-coil weight running in hole) simulations illustrating impact of running MLT through drillstring.

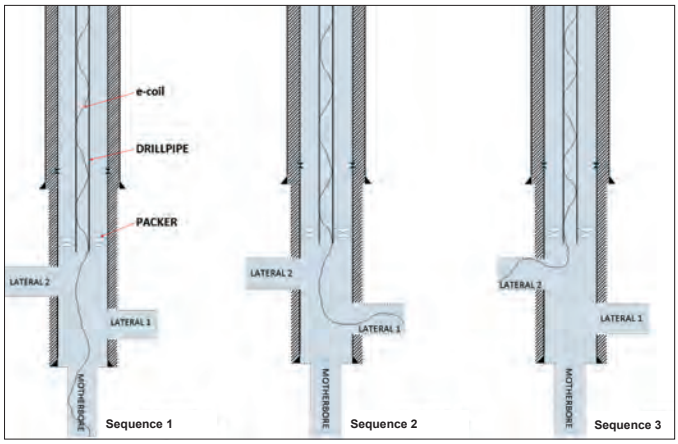

Fig. 3. Sequence of MLT runs for acid treatment.

ACID TREATMENT DESIGN

Parallel to the lateral access design was the selection of an appropriate acid treatment. The rapid reaction rate between the HCl acid and the calcium carbonate in the filter cake does not only generate almost instantaneous fluid loss, it also results in much less of the HCl acid being available to penetrate and stimulate the reservoir. The other difficulty in having acidic brine as a stimulating agent is the challenge in handling it on the surface. Unlike stimulation vessels, drilling rigs are less equipped to handle and pump such reactive materials. Since the ICS is not installed in this scenario until after the stimulation treatment, using a stimulation vessel for the acid treatment would be impractical as a drilling rig would be required to return for the installation of the ICS.

In selecting alternative acid treatment options, it was important that the acid reaction time be sufficient for uniform distribution across, and provide adequate stimulation of the reservoir. It was also critical that the treatment be more easily handled on the surface by the drilling rig.

Organic acids such as acetic and formic acids have been used in the industry for many years to stimulate carbonate

reservoirs. Buijse et al. (2003)[5] documented in their article case histories of the use of a combination of acetic and formic acids as alternatives to HCl acid. In a case study that was a close analog to the candidate well, Leschi et al. (2006)[6] documented the selection of a formic acid treatment where the acid release mechanism is delayed. This feature allowed for a pH neutral mixture on the surface and a slow acid release across the reservoir. As detailed by Leschi et al. (2006)[6], formic acid presents a better option to acetic acid. This is because at comparable reservoir temperatures, the rate of release of acetic acid is much slower than formic acid. As a result, the removal of the calcium carbonate filter cake is less efficient.

In designing the optimum acid formulation, the fluid injectivity rate through a ceramic disk with a pore throat size similar to that of the reservoir in question was recorded. Thereafter, the drill-in fluid formulation was replicated in the laboratory. The ceramic disk was then exposed to this fluid at reservoir temperature and pressure, resulting in a filter cake on the disk. Subsequently, different formic acid formulations were made to react with the filter cake. The timeline to the first fluid loss through the disk, upon another injectivity test, was adjudged to be the delay necessary for deployment of the acid treatment.

The measure of the effectiveness of the formulation in question was established by how quickly and consistently the filter cake dissolved. The estimate for cleanup was based on the shortest possible time between the treatment and the installation of the ICS. An effective treatment would result in a final injectivity rate similar to the initial injectivity rate.

Using the aforementioned criteria, the optimum acid formulation was selected. The last picture in Fig. 4 illustrates the effectiveness of the formulation selected. In this test sample, virtually all of the calcium carbonate filter cake dissolved, restoring the disk to initial conditions. To ensure that the selected formulation worked as planned, actual drill-in fluid samples were obtained from the well.

The result from the test using the actual fluid samples required that the formic acid formulation be revised. An increase in the concentration of the acid was necessary to achieve the same results as in the prior test. This was likely because the actual sample also contained drilled solids — a feature not easily replicated in laboratory samples.

LATERAL ISOLATION AFTER ACID TREATMENT

To inhibit fluid loss across the reservoir after the acid treatment, mechanical and chemical isolation options were considered. The major disadvantages to mechanical isolation were the associated trips to deploy and retrieve the hydraulic and/or mechanical packer. To isolate the lateral with the packer after treating the lateral in question, the packer would have to be run in hole and set. For the motherbore treatment, this trip would require running the packer past the windows to the upper laterals and setting it below the deeper window. After the

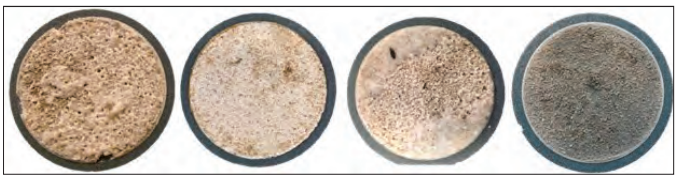

Fig. 4. Filter cake cleanup after separate tests with different formic acid formulations.

treatment for lateral 1, a second packer would then have to be run past the window to the uppermost lateral (lateral 2) and set above the window for lateral 1. After performing the treatment across lateral 2, both packers would have to be retrieved to allow for passage of the upper completion. The complexity of this option and increased risk to successfully deploying and retrieving both packers eliminated mechanical isolation as an option. Since chemical isolation did not have the accompanying risks with the packer, it was selected as the isolation mechanism for the well.

The chemical isolation option involves the use of polymer gel plugs. Polymer gel plugs have been in use in the oil industry for over 25 years. As outlined by Terracina et al. (1989)[7] and McCabe et al. (1991)[8], polymer gel plugs are highly viscous polymer fluids that provide a barrier in the well. This characteristic allows stimulation and workover operations to take place as if a mechanical barrier were in place. There are two types of polymer gel plugs — cross-linked and non-cross-linked. The difference between them is that whereas the cross-linked polymer gel requires a metal or borate ion to cross link with the polymer to form the viscous gel, the non-cross-linked polymer gel requires high concentrations of a polysaccharide polymer to achieve the same viscosity.

The selection of the cross-linked or non-cross-linked polymer gel plug depends on the application in question. This is because while the cross-linked polymer gel plug may degrade to its brine base with the addition of internal (enzymes or oxidizing agents) or external (weak acids like a 5% v/v HCl acid solution) breakers, the non-cross-linked plug only degrades through the use of external breakers. In addition, the cross-linked polymer gel plug sets faster than its non-cross-linked counterpart. As such, for applications where the gel plug is pumped through restrictions as seen in CT tools like the MLT, the non-cross-linked gel plug may be the preferred option. For applications where a faster set time is required or pumping external breakers is infeasible, the cross-linked gel plug may be preferred.

For the candidate well, the non-cross-linked plug was selected due to the uncertainty of how long the plug would be needed. The restrictive IDs in the MLT also precluded the cross-linked gel option because circulating pressures after the gel plug had set would be prohibitive to pumping the gel plug through the MLT. Successful runs[9, 10] in the region with the non-cross-linked polymer gel plug further supported its selection. The final benefit of the non-cross-linked gel plug option for this well was the acceleration of the setting time of the

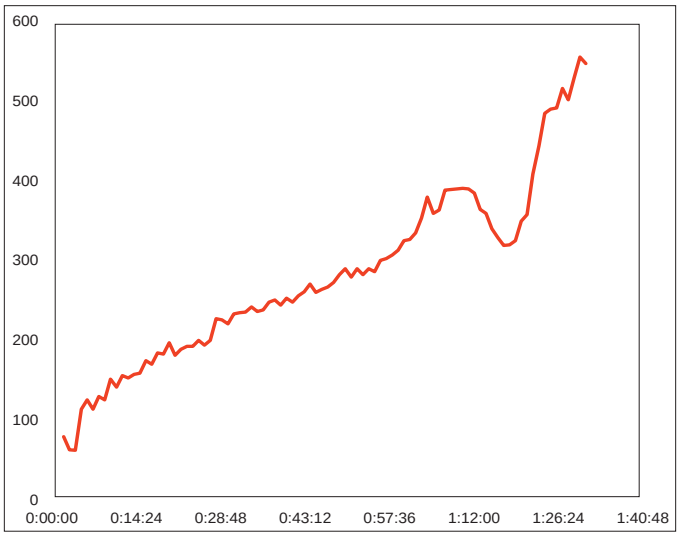

Fig. 5. Non-cross-linked polymer gel viscosity vs. time at reservoir temperature.

gel upon contact with $CaCl_2$ brine. With the well circulated to $CaCl_2$ brine prior to pumping this polymer gel, contact between the polymer gel and the $CaCl_2$ brine in the well would accelerate the setting time of the gel. This counteracted the slower gelling time of the non-cross-linked polymer plug. Test data, Fig. 5, based on well conditions, confirmed the feasibility of the polymer gel plug with viscosity increasing to over 500 centipoise in less than two hours of exposure.

Selection of the non-cross-linked polymer gel plug required that an external breaker be pumped after the installation of the ICS. A weak acid solution was selected as the external breaker, and the FCVs to each lateral were designated as flow paths for distribution of the external breaker.

Because both cross-linked and non-cross-linked polymer gel plugs degrade with the addition of acids as external breakers, it was critical that the placement of the gel plug and acid treatment be accurate. As such, caliper log data were obtained for each lateral during drilling operations. The volume of the acid treatment was based on these data. With each lateral requiring different treating volumes, the importance of accurately determining which lateral the MLT had accessed was further emphasized.

A pill of viscosified brine was mixed and ready to pump as a fail-safe option for the possibility of significant losses after pumping the acid treatment.

With the design process settled, the pumping sequence for the acid treatment was as follows: viscosified brine, acid treatment, brine, spacer, non-cross-linked polymer gel, spacer, and brine. The operation sequence was as follows:

1. Access the lateral of interest with a MLT.
2. Confirm the identity of the lateral of interest with CCL and gamma ray sensors in the CT.
3. Run the MLT to TD of each lateral.
4. At TD, follow the pump sequence until time for the acid treatment.
5. When it is estimated that the acid treatment is out of the tubing, pull the e-coil to the window while pumping at a rate commensurate to the trip out speed in an open hole.
6. Based on these (pull and pump rates), when the tubing is at the window, the brine would be exiting the MLT.
7. Continue pulling into the casing while pumping at a rate commensurate to the trip speed in the cased hole.
8. Stop pulling further into the casing once it is estimated that the spacer ahead of the gel is exiting the MLT.
9. Commence pulling further into the casing once it is estimated that the gel is exiting the MLT. Pull at commensurate trip speeds in the cased hole to the pump rate out of the MLT.
10. Stop pulling further into the casing once it is estimated that the spacer behind the gel is exiting the MLT.
11. Commence pulling further into the casing once it is estimated that the brine is exiting the MLT.
12. Pull up to the anticipated depth of the next window while still pumping out the brine.
13. Repeat steps 1 to 12 until all laterals are treated.
14. Pull and lay down the MLT and e-coil.
15. Pull and lay down drillpipe and a packer.
16. Run the ICS.

Figure 6 illustrates the well outlook after the process outlined and prior to the installation of the ICS.

PROOF OF CONCEPT

The execution of the project began after the CT unit and equipment were rigged up and tested. The first entry point for treatment was the motherbore and the treatment process was as previously outlined. Since the MLT and the e-coil lay on the low side of the well, there was no need for activation of the tool to guide entry into the open hole section of the motherbore. Prior to entry, a CCL correlation, Fig. 7, was obtained. Thereafter, the MLT was successfully run to TD as the gamma ray correlation, Fig. 8, confirmed the identity of the open hole.

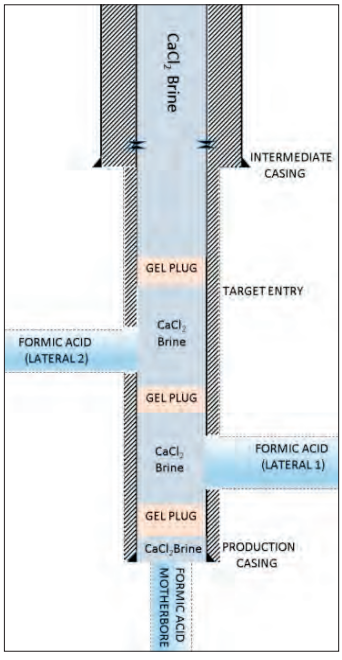

Fig. 6. Final proposal for candidate well (pre-ICS installation).

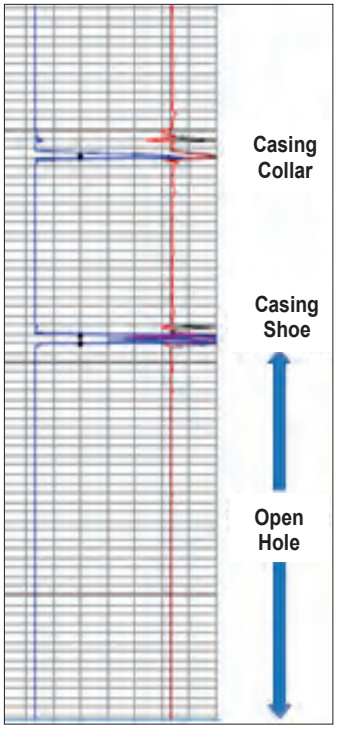

Fig. 7. CCL correlation confirming MLT entry in motherbore open hole.

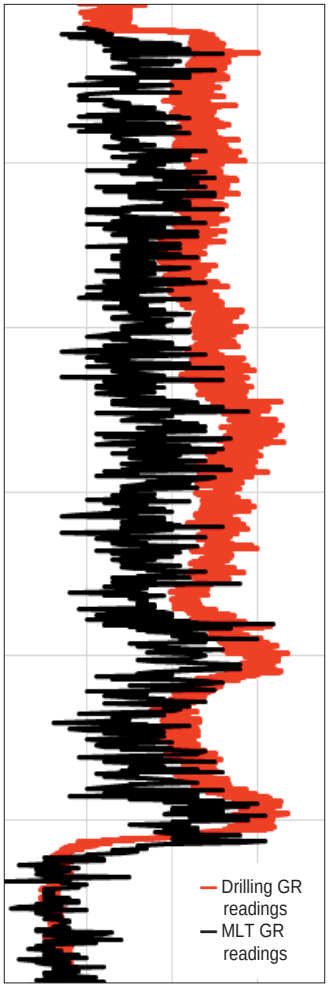

Fig. 8. GR correlation confirming motherbore open hole identity.

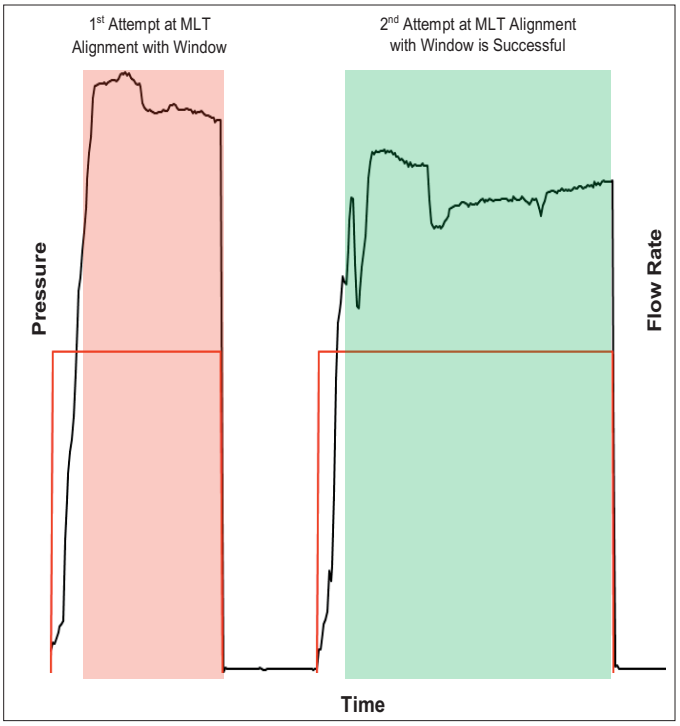

Fig. 9. Pressure drop signature confirming alignment of MLT with lateral 1 window.

Fig. 10. GR correlation confirming lateral 1 open hole identity.

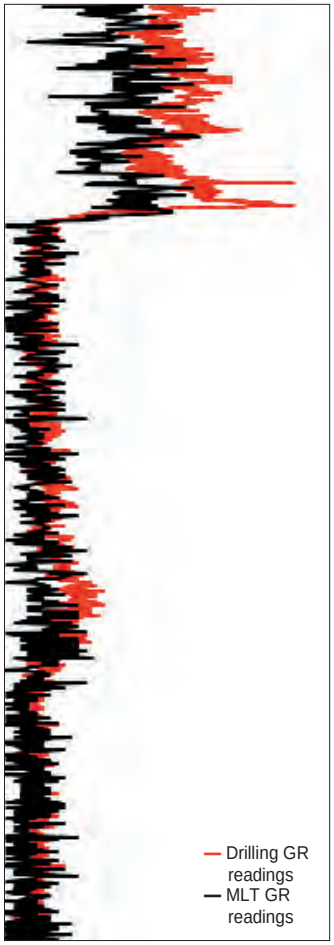

Fig. 11. GR correlation confirming lateral 2 open hole identity.

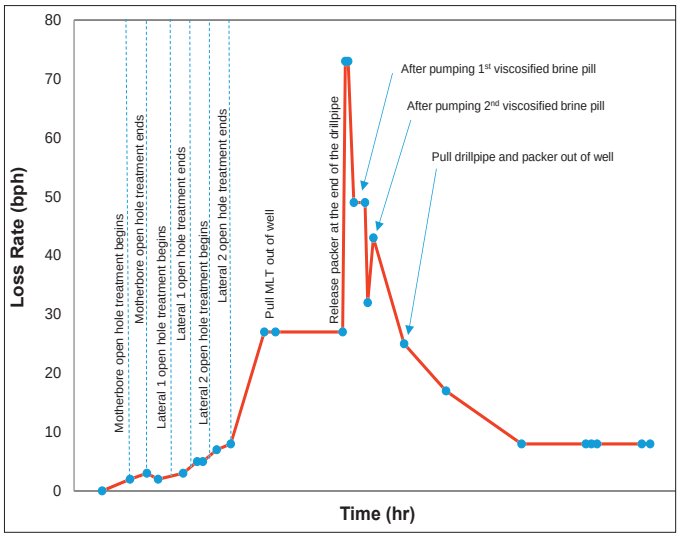

Fig. 12. Loss rate during and after acid treatment.

Alignment and entry of the MLT into the upper lateral above the motherbore open hole required that the MLT be oriented to the window for that lateral. This was successfully achieved with the MLT pressure readings showing the requisite pressure drop signature, Fig. 9, upon alignment of the MLT with the window. CCL correlation upon passage of the e-coil through the window also supported the MLT pressure

signature. As was the case in the motherbore, the treatment process followed the job plan and the gamma ray correlation, Fig. 10, provided further proof of the identity of the lateral.

Like in lateral 1, alignment with the window and entry into lateral 2 were successfully achieved with the gamma ray correlation, Fig. 11, further confirming the identity of the lateral.

After the delay time for the acid release for lateral 2 had elapsed and with the MLT back in the drillpipe, the loss rate increased to 27 barrels per hour (bph) and stabilized there. The MLT was then pulled to the surface. This was necessary as the drillpipe provided a larger conduit for pumping — if necessary — a viscosified brine pill to mitigate against an increasing loss rate. With the MLT on the surface, the packer at the end of the drillpipe was released and the loss rate increased dramatically at this point to 73 bph. A viscosified brine pill was then pumped through the drillpipe and the loss rate monitored. The loss rate subsided, but not to a degree to allow for retrieval of the drillpipe. Another viscosified brine pill was then pumped down the drillpipe and the loss rate subsided. An extended flow check was performed and with the loss rate steadily declining, the drillpipe and packer were pulled out of the hole and laid down. Figure 12 illustrates the loss rate during the entire treatment process with key moments highlighted.

After recovering the drillpipe and packer to the surface, the upper ICS was installed successfully at its planned depth, and the external breaker pumped through each FCV. This ensured that all the non-cross-linked polymer gel plugs at each open hole lateral entry point had degraded to $CaCl_2$ brine before the well cleanup. Thereafter, each lateral was flowed back individually until production testing requirements were met, at which point all laterals were flowed together to satisfy final well cleanup requirements.

CONCLUSIONS

The successful treatment of each open hole lateral section, installation of the ICS and ensuing well cleanup, proved that the conceptual well completion design for the candidate well was viable. Despite the losses encountered after the last open hole treatment, future application of this concept in multilateral wells can be done. Current efforts are underway to optimize the isolation mechanism employed in this case study for future applications.

ACKNOWLEDGMENTS

The authors would like to thank the management of Saudi Aramco for their support and permission to publish this article.

This article was presented at the SPE/IADC Middle East Drilling Technology Conference and Exhibition, Abu Dhabi, UAE, January 29-31, 2018.

REFERENCES

1. Al-Zain, A.K., Said, R., Al-Gamber, S.D., Al-Driweesh, S.M., et al.: "First Worldwide Application of Fiber Optic Enabled Coiled Tubing with Multilateral Tool for Accessing and Stimulating a Trilateral Oil Producer, Saudi Arabia," SPE paper 126730, presented at the Kuwait International Petroleum Conference and Exhibition, Kuwait City, Kuwait, December 14-16, 2009.
2. Al-Momin, A., Zeybek, M., Azrak, A.W. and Burov, A.: "First Successful Multilateral Well Logging in Saudi Aramco: Innovative Approach toward Logging an Open Hole Multilateral Oil Producer," SPE paper 149079, presented at the SPE/DGS Saudi Arabia Section Annual Technical Symposium and Exhibition, al-Khobar, Saudi Arabia, May 15-18, 2011.
3. Al-Zaid, M.R., Al-Ghazal, M.A., Al-Driweesh, S.M., Al-Ghurairi, F., et al.: "Dual Lateral Open Hole Coiled Tubing Acid Stimulation in Deep HPHT Sour Gas Producer Wells — Field Experience and Lessons Learned from the Ghawar Field," SPE paper 164326, presented at the SPE Middle East Oil and Gas Show and Conference, Manama, Bahrain, March 10-13, 2013.
4. Buenrostro, A., Arevalo, A., Al-Zaid, M.R., Abulhamayel, N., et al.: "Enhancing Intervention Efficiency and Eliminating Uncertainty — First Ever Successful Conveyance of MWD Tools on CT for Multilateral Well Stimulation in a Middle Eastern Gas Well," SPE paper 182409, presented at the SPE Asia Pacific Oil and Gas Conference and Exhibition, Perth, Australia, October 25-27, 2016.
5. Buijse, M., de Boer, P., Breukel, B., Klos, M., et al.: "Organic Acids in Carbonate Acidizing," SPE paper 82211, presented at the SPE European Formation Damage Conference, The Hague, The Netherlands, May 13-14, 2003.
6. Leschi, P., Demarthon, G., Davidson, E. and Clinch, D.: "Delayed Release Acid System for Cleanup of Al Khalij Horizontal Open Hole Drains," SPE paper 98164, presented at the SPE International Symposium and Exhibition of Formation Damage Control, Lafayette, Louisiana, February 15-17, 2006.
7. Terracina, J.M., McCabe, M.A., Cramer, J.W. and Legenza, J.E.: "Temporary Chemical Block Brings Efficiency and Economy to Eastern U.S. Workover Operations," *SPE Production Engineering*, Vol. 7, Issue 1, February 1992, pp. 70-74.
8. McCabe, M.A. and Terracina, J.M.: "Chemical Bridging for Well Control during Stimulation and Workover Operations," SPE paper 21037, presented at the SPE International Symposium on Oil Field Chemistry, Anaheim, California, February 20-22, 1991.

9. Al-Ghazal, M.A., Abel, J.T., Al-Saihati, A., Buali, M., et al.: "First Successful Deployment of a Cost-Effective Chemical Plug to Stimulate Selectively Using CT in Saudi Arabia Gas Fields — A Case History," SPE paper 160837, presented at the SPE Saudi Arabia Section Technical Symposium and Exhibition, al-Khobar, Saudi Arabia, April 8-11, 2012.
10. Al-Ghazal, M.A., Al-Driweesh, S.M., Al-Sagr, A., Krishnan, G., et al.: "A New Temporary Chemical Packer Enables Efficient Stimulation of a Lower Zone in a HPHT Gas Well," SPE paper 161651, presented at the Abu Dhabi International Petroleum Conference and Exhibition, Abu Dhabi, UAE, November 11-14, 2012.

BIOGRAPHIES

Sofiri Hart is a Drilling Engineer with Saudi Aramco's Exploration & Oil Drilling Engineering Department. He is the Drilling Engineer for a jackup drilling rig currently operating in the Arabian Gulf.

Sofiri joined Saudi Aramco in 2014. His prior experience was as a Drilling Engineer with BP in the U.S. At BP, Sofiri delivered wells in onshore gas plays in Texas and Wyoming and offshore in Thunder Horse — the largest oil field in the Gulf of Mexico. He was also part of the engineering team that drilled Mississippi Canyon 252 #2, one of the two relief wells to Mississippi Canyon 252 #1 (Macondo).

Sofiri received his B.S. degree in Mechanical Engineering from Oklahoma State University, Stillwater, OK, and an M.S. degree in Petroleum Engineering from the University of Oklahoma, Norman, OK. He is also a licensed Professional Engineer in the state of Texas.

Hatem M. Al-Saggaf is a Drilling & Workover Service Department Superintendent. He joined Saudi Aramco in 2002. Hatem's experience includes work on several drilling projects, such as the Qatif field development and Khurais increment. He was a team leader for the Nuiyyem field development. Hatem also worked in Manifa drilling project from 2007 to 2013.

He received his B.S. degree in Applied Mechanical Engineering from King Fahd University of Petroleum and Minerals (KFUPM), Dhahran, Saudi Arabia.

The Methods of Correcting NMR Data from Dry Gas Wells Drilled with Formate-based Muds by Advanced NMR Techniques

Dr. Hyung T. Kwak, Dr. Gabor G. Hursan, Dr. Ahmad M. Al-Harbi, Jun Gao, and Dr. Shouxiang M. Ma

ABSTRACT

Formate-based drilling mud is used to improve the performance of drilling and completions of high-pressure, high temperature (HPHT) wells due to its properties, such as high density — up to 19 lb/gal — non-corrosiveness, eco-friendliness, high stability, and miscibility with brine and other fluids. Subsequently, the strengths of these formate muds pose challenges for formation evaluation due to their unusual properties such as high density, low hydrogen index (HI), miscibility with connate brines, and high conductivity.

The current work addresses challenges of nuclear magnetic resonance (NMR) logging, which is known to provide capillary-bound fluid for producibility evaluation and accurate porosity for reserve estimation, in deep dry gas wells drilled with formate mud. With a carefully designed workflow composed of a suite of laboratory NMR techniques, the needs for the correction of a T_2 cutoff and HI by formate mud filtrate (FMF) invasion have been investigated. To quantify the accurate amount of correction required, FMF invasion has been monitored under reservoir conditions. The experimentally determined NMR T_2 cutoff values for FMF saturated samples are always slightly longer than those for brine-saturated ones. The difference of bulk volume movable (BVM), however, is less than 5% when the T_2 cutoff value from the brine-saturated sample is applied to the FMF saturated sample. Therefore, the T_2 cutoff determined by conventional NMR laboratory measurement with brine can be applied to the NMR log with the formation invaded by FMF.

The HI correction factors for BVM and bulk volume irreducible (BVI) are dependent on pore structures. For brine-saturated bimodal sandstones, all pores are displaced by FMF, which corresponds to a HI correction factor of 0.74 for both BVM and BVI. For brine-saturated carbonate with a trimodal pore system, however, 100% BVM and 70% of BVI have been displaced with FMF, which corresponds to a HI correction factor of 0.78% and 0.80%, respectively, for the FMF used in the current study.

The outcome of the current study will help to enhance the usage of NMR logging as a powerful formation evaluation tool for gas wells drilled with formate-based drilling muds.

INTRODUCTION

Formate-based drilling mud could improve the drilling and completions of high-pressure, high temperature (HPHT) wells due to its properties such as high density — up to 19 lb/gal — non-corrosiveness, eco-friendliness, high stability, and miscibility with brine and other fluids in the drilling muds. In Saudi Arabian deep gas wells, the low solids content, temperature stability, and enhanced lubricity provided by formate mud systems practically eliminated differential sticking, lowered pump pressures, reduced torque and drag, and led to better bit performance[1, 2]. Subsequently, the strengths of these formate muds pose challenges for formation evaluation due to their unusual properties such as high density, low hydrogen index (HI), miscibility with connate brines, and high conductivity[3-5].

The first systematic studies to better understand the effect of formate mud filtrate (FMF) invasion on downhole logs focused on nuclear measurements and environmental corrections of gamma-gamma density, neutron and natural gamma ray tools[6-8]. For manageable algorithms all of these studies described the degree of invasion by a single number. The description of the pore size dependent nuclear magnetic resonance (NMR) spectral porosity logs in the presence of formate mud invasion carries additional complexities. Laboratory studies on water-bearing and oil-bearing sandstones indicated that formate mud invasion occurs at different rates in micropore structures vs. large pores and it is also affected by non-wetting reservoir fluids[9, 10]. Additionally, the formate mud's effect on the NMR surface interaction needs to be studied on rock samples from the formation of interest for proper rock quality interpretation.

The current work addresses the following challenges for NMR log data interpretation in deep gas wells drilled with formate-based muds.

1. The porosity undercall is due to FMF invasion since the HIs of formate muds are significantly lower than that of connate water[6]. As NMR porosity is proportional to the total amount of hydrogen in the fluids, the low hydrogen density of formate muds compared to water causes a NMR porosity undercall. Since FMFs are miscible with connate water, accurate HI correction factors cannot be found

Salt	mg/l	g/l	g/2l
NaCl	28,007.04	28.0070374	56.0140747
$CaCl_2.2H_2O$	42,861.75	42.8617485	85.723497
$MgCl_2.6H_2O$	1,463.44	1.4634375	2.926875
$BaCl_2$	0.00	0	0
KCl	0.00	0	0
Na_2SO^4	628.41	0.628405	1.25681
$NaHCO_3$	2,511.28	2.5112832	5.0225664
Na_2CO_3	0.00	0	0

Table 1. Synthetic brine composition table

without the knowledge of a FMF invasion profile into different pore systems.

2. The estimation of movable fluids by NMR logging could be affected by FMF invasion because FMFs have different molecular interaction strength with pore surfaces compared to water. In practical terms, this requires a modification of the NMR bound water cutoff, T2 cutoff, and value.
3. A spatial and temporal invasion profile of FMF has to be quantified to develop accurate NMR log data correction algorithms. Without the knowledge of the amount of FMF in different pore systems during specific logging measurements at different times, an adequate correction factor cannot be applied to the NMR logging data.

To solve these issues of the NMR log data interpretation for the well drilled with formate drilling muds, a carefully planned laboratory study was conducted using advanced NMR techniques.

EXPERIMENT

Sample

Synthetic brine has been fabricated based on the composition in Table 1, which is the water analysis from the field. The drilling mud used for the current study collected from the field contains ~350 mg/ml of sodium (Na) formate. Various types of polymers and trace amounts of methanol and Na acetate were also identified by liquid NMR measurement. The mud filtrate has been prepared by using an API filter press instrument. Mud was collected after shaking the container for even mixing of all the contents in the mud, including polymers. The liquid NMR measurement showed there is ~3 times of polymer concentration differences between the samples collected with, and without shaking.

Figure 1 shows the viscosity and density of the FMF and brine under different temperatures. The temperature dependence of the viscosity of FMF and brine is quite similar, which decreased ~4 times as the temperature increased from 25 °C to 90 °C for both fluids. The density, however, is relatively

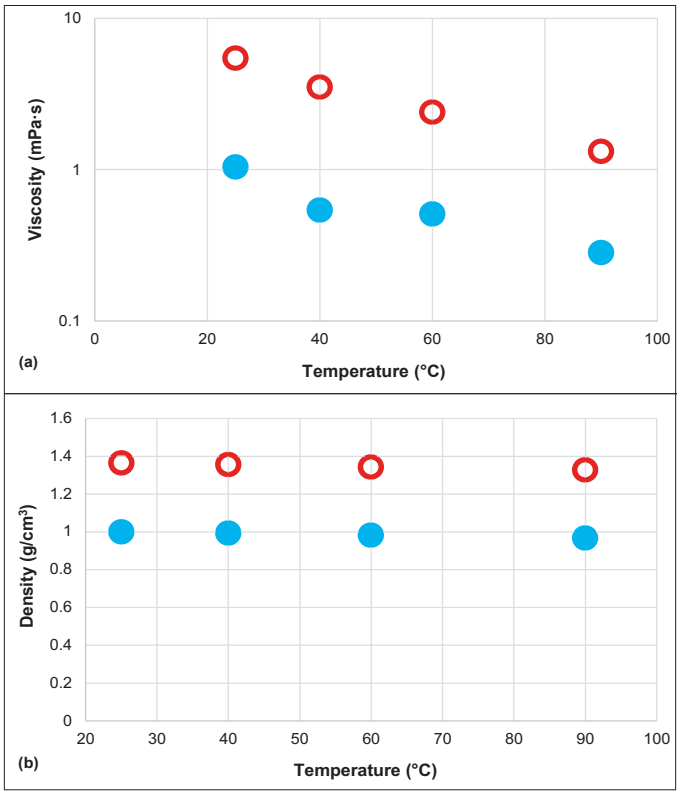

Fig. 1. The viscosity (a) and density (b) of the FMF and brine under various temperatures.

constant over the range of temperature.

Five sandstone samples from a gas well in the Middle East and one carbonate sample from North America have been selected for the current study. Table 2 lists the porosity and permeability data of all samples from the conventional core analysis. The sandstone samples were selected to represent each rock type with various permeability, 0.6 millidaricies (md) ~ 988 md, within 150 ft of vertical depth from the same well.

All five of the deep gas well selected samples show the macropore dominated multimodality in porosity, bimodality for sandstones, and trimodality for carbonates, from the T_2 distribution of 100% saturated brine, Fig. 2. To keep the integrity of the sample from high speed centrifuge and coreflooding, all samples were wrapped with heat shrinkable Teflon tube and capped with specially designed porous Teflon disks, which are all NMR invisible, Fig. 3.

Sample Number	Porosity (p.u.)	Permeability (md)
230	7.1	0.6
56	21.2	34.9
37	20.5	48.5
134	26.2	123.9
53	25	988
Carbonate	20.3	47

Table 2. Porosity and permeability of selected core sample by conventional core analysis

Hardware

The NMR systems used for the current study are Oxford GeoSpec2 2 MHz and 12 MHz with electromagnetic gradient coils for Spatial T_2 measurements. The invasion profiles of the FMF at 1,000 psi and 80 °C were studied with the GeoSpec2's 12 MHz P5 probe for the 1" diameter core plug sample to achieve higher sensitivity.

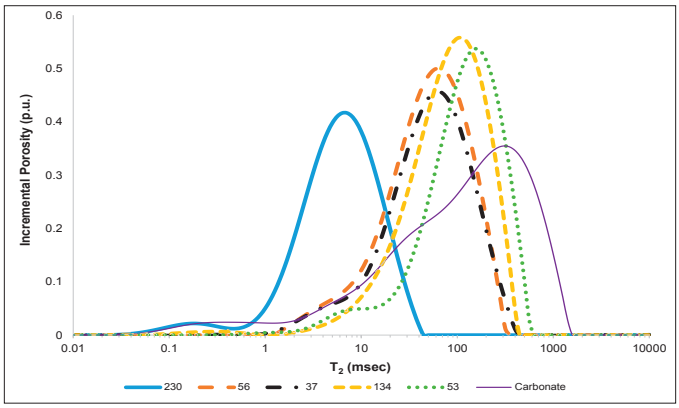

Fig. 2. The T_2 distributions of five deep gas well sandstone samples.

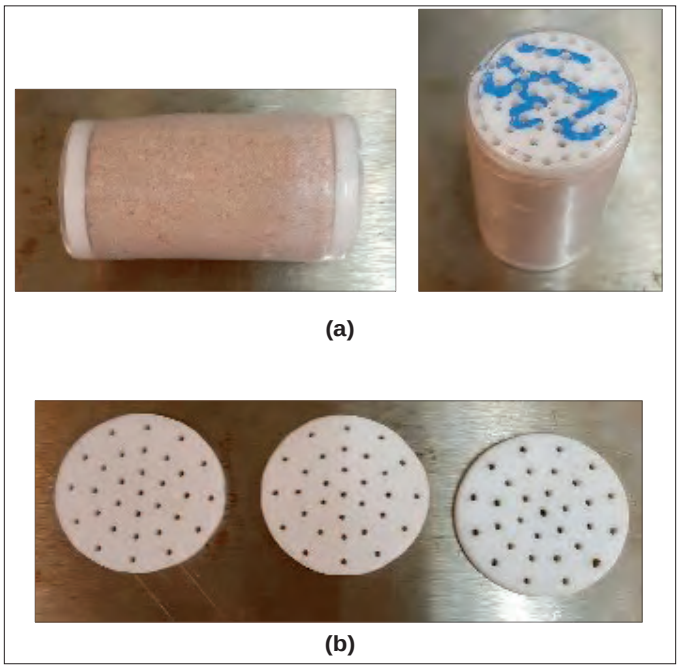

Fig. 3. An image of the sample wrapped with heat shrinkable Teflon tube (a), and the specially designed porous Teflon disk (b).

Experimental Methods and Procedures

Average and spatial NMR T_2 distributions have been measured to determine the correction of NMR porosity and the T_2 cutoff value for the effect of the FMF invasion. The average and the spatial T_2 distributions are acquired by Carr-Purcell-Meiboom-Gill (CPMG) pulse sequence, and Spin-Echo Single Point Imaging (SE-SPI) pulse sequence, respectively, Figs. 4a and 4b.

The T_2 relaxation time measured by the CPMG sequence provides porosity, T_2 cutoff, and volumetric FMF invasion information. CPMG, however, does not provide site specific information. In other words, CPMG only provides a lump sum average response of T_2 relaxation from a given sample. The SE-SPI method — a phase encoded MRI technique — provides T_2 mapping along the sample providing a spatial profile of T_2 distributions. Figure 4b shows that the spatial phase encoding gradient is applied during the first pulse interval, t_0, and signals are acquired through multiple refocusing pulses that follow. A profile of T_2 distributions along the sample is obtained from the T_2 weighted echo data points in the profile during this multipoint acquisition period. Therefore, the spatial T_2 data provided a FMF invasion profile along the core samples. The centrifuge spinning speed used to desaturate the samples for the T_2 cutoff value determination varies with permeability, from 2,000 rpm to 8,000 rpm, Table 3.

Figure 5 shows the procedure of the dynamic NMR measurement for the FMF invasion profile under relatively HPHT, 1,000 psi and 80 °C. Up to 30 pore volumes (PVs) of the FMF were injected by pressure differential gradient of 300 psi. Please note that the D_2O substituted synthetic brine was used for the dynamic study. At the end of each FMF injection, T_2 distribution was acquired to measure the invasion profile of the FMF for each pore system.

RESULTS

HI Correction Factor Determination

The HI correction factor for the FMF can be found by comparing the total area under T_2 distribution of bulk water and

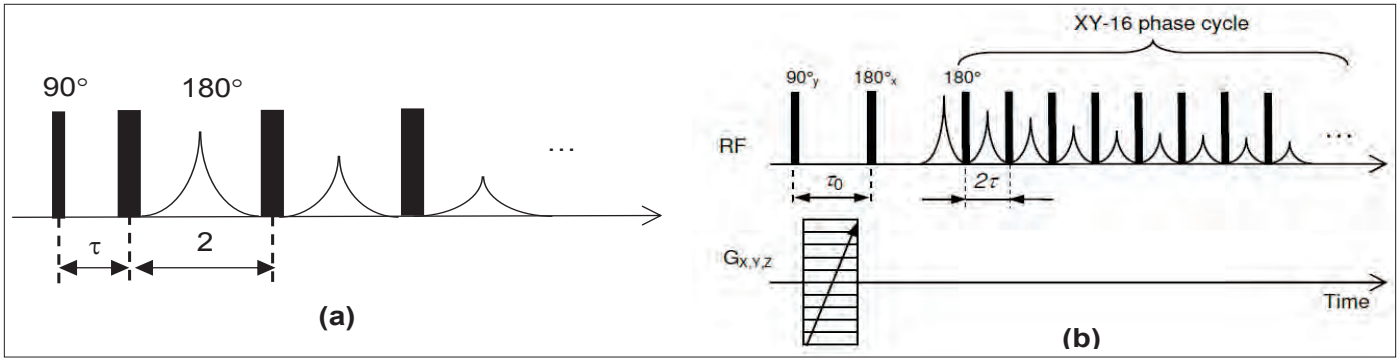

Fig. 4. The diagram of: (a) CPMG pulse sequence, and (b) SE-SPI pulse sequence.

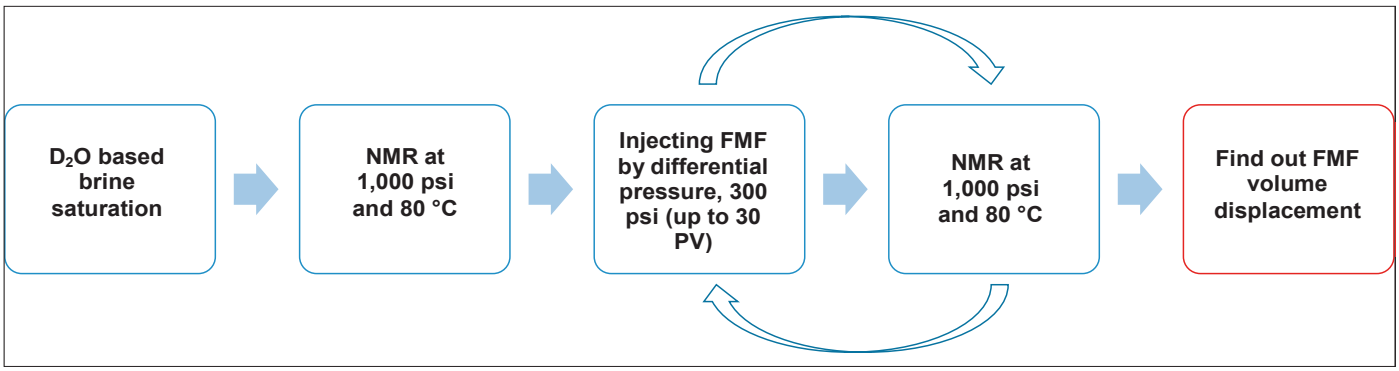

Fig. 5. The diagram for dynamic NMR measurement for FMF invasion profile at HPHT.

Sample Number	Centrifuge Spinning Speed (rpm)
230	8,000
56	3,000
37	3,000
134	3,000
53	2,000

Table 3. The centrifuge spinning speed for desaturating the samples

the bulk FMF by using Eqn. 1:

$$HI_{Corr\_FMF} = \frac{(HI\ of\ Water \times Volume\ of\ FMF)}{Volume\ of\ Water} \quad (1)$$

where HI_{corr_FMF} is the HI correction factor of the FMF. Since the volume of brine and FMF measured by NMR T_2 is 19.58 ml and 14.45 ml, respectively, the HI correction factor of the FMF used for the current study is 0.74, Fig. 6.

Bulk Volume Irreducible (BVI) Cutoff (T_2 Cutoff) Value Determination

The T_2 cutoff values for samples saturated with synthetic brine and FMF are acquired by the determination of bulk volume irreducible (BVI) by centrifugation[11]. As can be seen from Table 4, the T_2 cutoff values for the saturated synthetic brine

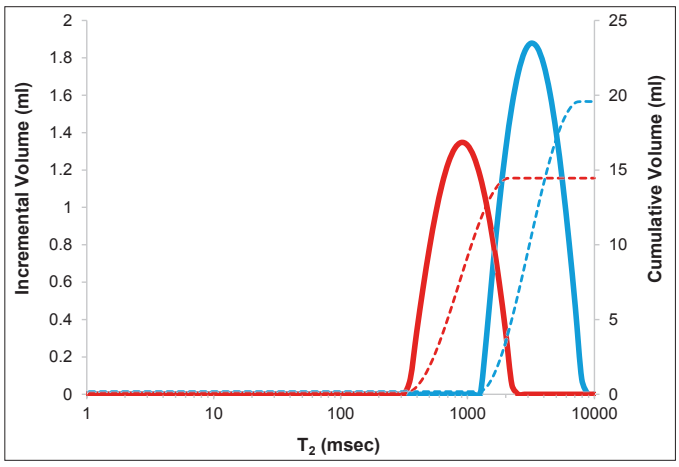

Fig. 6. The T_2 distributions of bulk brine volume (blue) and bulk FMF volume (red). The solid blue line is the T_2 distribution and the dotted red line is the cumulative sum of each T_2 distribution.

Sample Number	T_2 Cutoff (Brine, msec)	T_2 Cutoff (FMF, msec)	T_2 Cutoff Difference (%, Brine vs. FMF)
230	7.6	14.1	85.64
56	43.08	62.08	44.12
37	43.93	59.42	35.28
134	59.87	67.3	12.41
53	75.1	65.19	-13.19

Table 4. T_2 cutoff values for saturated synthetic brine and FMF saturated core samples

and the FMF saturated samples are quite similar, especially for the more permeable samples.

In Fig. 7a, the T_2 distributions and the T_2 cutoff values of brine and FMF saturated samples are displayed in an order of increasing permeability from top to bottom. It can be clearly seen that the differences of the T_2 cutoff values become smaller as the permeability of the sample increases, Figs. 7a and 7b. Since the samples are sandstone, with porosity and permeability well correlated, the similar trend is observed between porosity and the T_2 cutoff values, Fig. 7c.

Since the T_2 cutoff values of the brine and FMF saturated samples are similar, we compare the % volume of BVI relative to the total volume from the FMF saturated sample by using the T_2 cutoff values for brine and the FMF saturated samples, Table 5. The difference of the relative BVI% to the total volume calculated by both the T_2 cutoff values — one from the saturated brine and the other from the FMF saturated sample — is less than ±5%. Therefore, the T_2 cutoff does not need to be changed by the FMF invasion with any degrees for the sandstone samples saturated with brine in the current investigation.

Porosity Correction

For the first step of the porosity correction by FMF invasion, 2D spatial T_2 measurements along the core samples were taken before and after FMF injection. All pore systems in the sandstone samples are homogeneously invaded by the FMF, which can be identified by broadening of T_2 distribution along the whole core samples, Figs. 8a to 8e. On the other hand, the FMF invasion for the carbonate sample is not very clear due

Sample Number	Total Volume of FMF Saturated Sample (ml)	BVI from FMF Saturated Sample (Using FMF T_2 Cutoff)	BVI from FMF Saturated Sample (Using Brine T_2 Cutoff)	% of BVI Relative to Total Volume (Using FMF T_2 Cutoff)	% of BVI Relative to Total Volume (Using Brine T_2 Cutoff)	Difference (%)
230	3.15	1.48	1.63	52.91	48.2	-4.7
56	8.37	3.81	3.44	54.47	58.91	4.44
37	7.4	3.3	3.02	55.4	59.25	3.85
134	8.93	3.18	3.3	64.38	63.06	-1.32
53	7.66	2.58	2.87	66.37	62.52	-3.85

Table 5. Relative BVI% to total volume by using two different T_2 cutoff values, the T_2 cutoff values from the saturated brine and the FMF saturated sample. The difference in the last column is the % difference between relative BVI% by using brine T_2 cutoff and the FMF T_2 cutoff values, which are from columns 5 and 6, respectively.

to a long T_2 component of brine-saturated carbonate, which is overlapped with the bulk FMF T_2 distribution, Fig. 8f. With the dynamic study described in the following discussion, however, the invasion profile for each pore system of carbonate could be observed.

To correct the porosity of the brine-saturated samples, which are invaded by FMF, accurate FMF invasion profiles for each pore system within the sample should be quantified. Figure 9 shows the T_2 distribution of sample 230 with continuous FMF injection at 80 °C and 1,000 psi. T_2 data was acquired right after the injection of 1, 2, 3, 5, and 10 PVs of FMF, which is driven by a pressure differential gradient of 300 psi. Unlike other samples, up to 30 PVs of FMF were injected, but only up to 10 PVs of FMF was injected for sample 230, due to its low permeability. Compared to the T_2 distribution in Fig. 2, which was measured with a normal probe under room condition, T_2 distribution of Fig. 9a shows a few differences. The amplitude of T_2 components, shorter than 1 msec, of the plots in Fig. 9a is higher due to the NMR signals from hardware components of the P5 probe. In addition, there are new T_2 distribution components longer than 100 msec in Fig. 9a. Most likely, these are the signals from the bulk FMF presented in the pores of Teflon disks and mandrels of the core holder. Therefore, the T_2 components longer than 100 msec have been removed for improving the accuracy on the FMF invasion data analysis, Fig. 9b. This can be also achieved by inverting the truncated time domain T_2 relaxation data.

Figure 10 shows the plot of the total volume displacement efficiency by FMF injection at 80 °C and 1,000 psi, which is calculated by the summation of the T_2 distributions in Fig. 9b. The total volume displacement reaches 100% with less than 5 PVs of FMF injection for all samples. The unphysical excess volume displacement, which reaches up to 120%, is mainly owing to the porosity overestimation caused by the short T_2 components from the P5 probe hardware.

It can be clearly seen from the comparison of total volume displacement for BVI and bulk volume movable (BVM) in Fig. 11. The total volume displacements of BVI, where the T_2 components are shorter than the T_2 cutoff, is larger than BVM because of these hardware signals. The T_2 cutoffs for the FMF saturated cores in Table 4 are used for the analysis.

Since all pores are completely invaded by FMF with relatively small amounts — less than 5 PVs of injection — the same HI correction factor, 0.74 for the current study, can be applied to correct the porosity of BVM and BVI of the sandstone sample saturated with brine. Therefore, the corrected porosity after FMF invasion for well-connected multiporous sandstones saturated with brine can be calculated by:

$$\emptyset_{BVM} = HI_{corr} * \emptyset_{BVM_{FMF}}$$
$$\emptyset_{BVI} = HI_{corr} * \emptyset_{BVI_{FMF}} \quad (2)$$

where HI_{corr} is the HI correction factor of the FMF, $\emptyset_{BVM_{FMF}}$ is the BVM fully saturated by FMF, and is the BVI fully saturated by the FMF. The HI_{corr} can be calculated from the bulk fluid NMR measurement data.

To study the FMF invasion profile of other multiporous rocks with different connectivity than the selected sandstone samples, the FMF was injected into the brine-saturated carbonate at 80 °C and 1,000 psi. Unlike the sandstone case, the total volumetric displacement of carbonate by FMF is ~80%, Table 6. In addition, it took more FMF injection to reach the maximum FMF displacement compared to the sandstone case — ~10 PVs for carbonate vs. ~5 PVs for sandstone. The total volume of FMF displacement for BVM and BVI are also different for carbonate, Table 6 and Fig. 12.

A total of 100% BVM and ~70% of BVI was displaced by the FMF injection. Since the relative volumes of FMF that invaded the BVM and BVI are different, the corrected porosity after FMF invasion for muitiporous carbonate can be calculated by:

$$\emptyset_{BVM} = \emptyset_{BVM_{Brine}} + \left(HI_{corr} * \emptyset_{BVM_{FMF}}\right) = HI_{corr\_BVM} * \emptyset_{BVM\_PostFMF}$$

$$\emptyset_{BVI} = \emptyset_{BVI_{Brine}} + \left(HI_{corr} * \emptyset_{BVI_{FMF}}\right) = HI_{corr\_BVI} * \emptyset_{BVI\_PostFMF} \quad (3)$$

where HI_{corr} is the HI correction factor calculated from the ratio of bulk volume of brine and the FMF in Fig. 6.

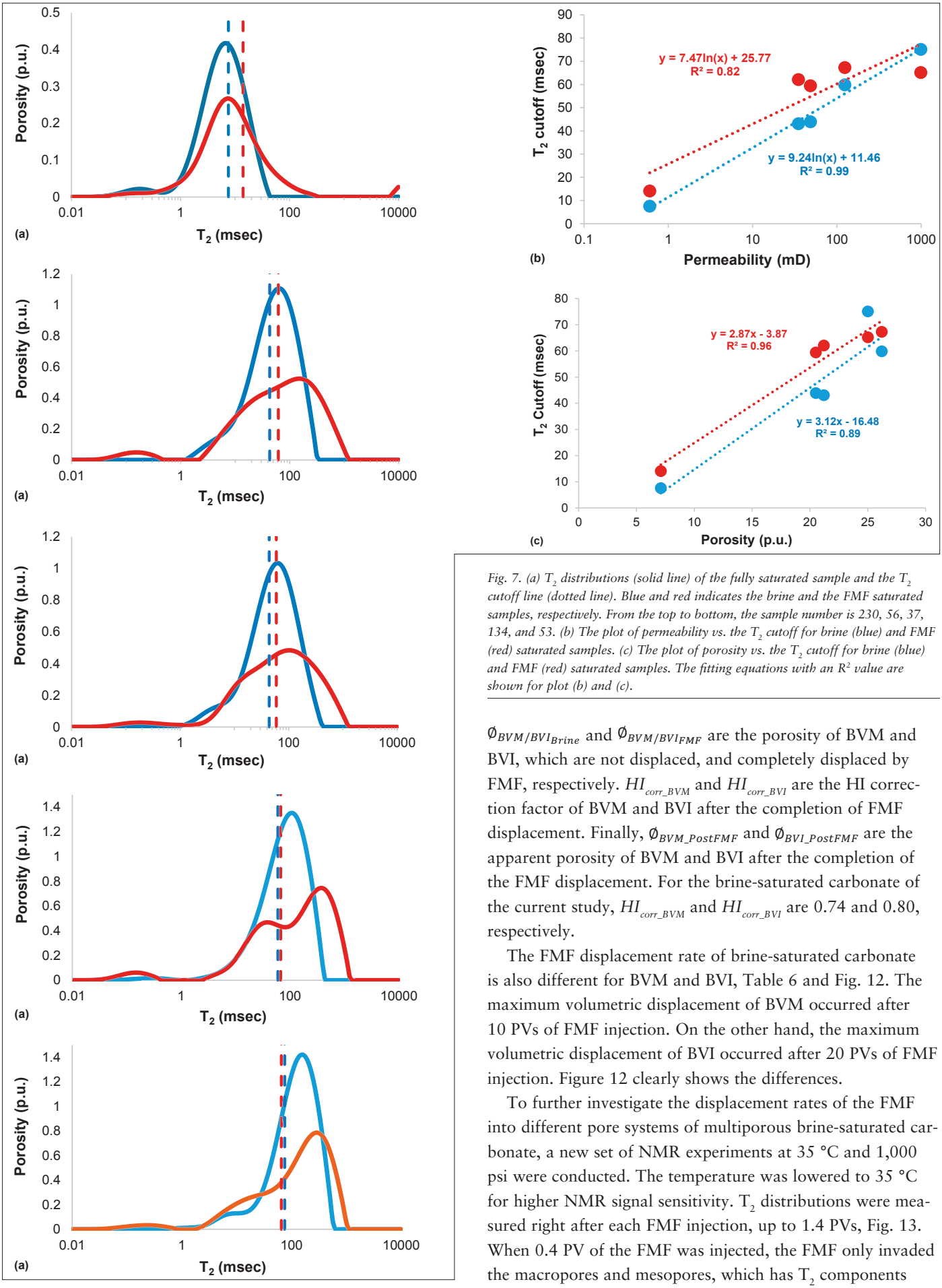

Fig. 7. (a) T_2 distributions (solid line) of the fully saturated sample and the T_2 cutoff line (dotted line). Blue and red indicates the brine and the FMF saturated samples, respectively. From the top to bottom, the sample number is 230, 56, 37, 134, and 53. (b) The plot of permeability vs. the T_2 cutoff for brine (blue) and FMF (red) saturated samples. (c) The plot of porosity vs. the T_2 cutoff for brine (blue) and FMF (red) saturated samples. The fitting equations with an R^2 value are shown for plot (b) and (c).

$\emptyset_{BVM/BVI_{Brine}}$ and $\emptyset_{BVM/BVI_{FMF}}$ are the porosity of BVM and BVI, which are not displaced, and completely displaced by FMF, respectively. HI_{corr_BVM} and HI_{corr_BVI} are the HI correction factor of BVM and BVI after the completion of FMF displacement. Finally, $\emptyset_{BVM\_PostFMF}$ and $\emptyset_{BVI\_PostFMF}$ are the apparent porosity of BVM and BVI after the completion of the FMF displacement. For the brine-saturated carbonate of the current study, HI_{corr_BVM} and HI_{corr_BVI} are 0.74 and 0.80, respectively.

The FMF displacement rate of brine-saturated carbonate is also different for BVM and BVI, Table 6 and Fig. 12. The maximum volumetric displacement of BVM occurred after 10 PVs of FMF injection. On the other hand, the maximum volumetric displacement of BVI occurred after 20 PVs of FMF injection. Figure 12 clearly shows the differences.

To further investigate the displacement rates of the FMF into different pore systems of multiporous brine-saturated carbonate, a new set of NMR experiments at 35 °C and 1,000 psi were conducted. The temperature was lowered to 35 °C for higher NMR signal sensitivity. T_2 distributions were measured right after each FMF injection, up to 1.4 PVs, Fig. 13. When 0.4 PV of the FMF was injected, the FMF only invaded the macropores and mesopores, which has T_2 components

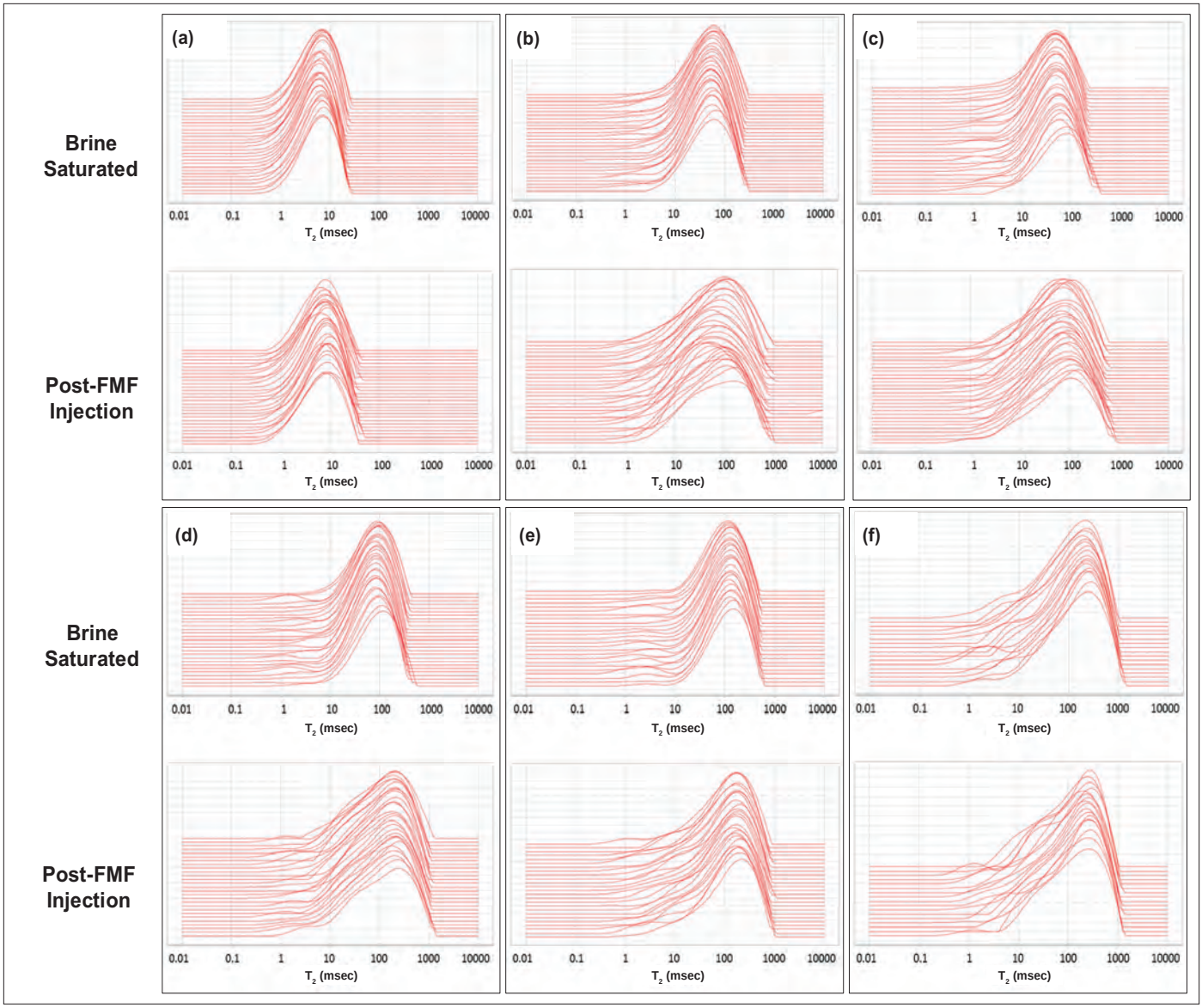

Fig. 8. The 2D T_2 map of the sandstone samples (a to e) and the carbonate sample (f). The spatial T_2 measurements were taken before and after the FMF injection into the saturated brine sample with the following procedure: Saturation of sample with brine → Spatial T_2 measurement → Clean and dry sample → Saturation of sample with D_2O based brine → Inject FMF by differential pressure gradient of 300 psi (up to 30 PV depending on samples) → Spatial T_2 measurement. For each group, the upper plot is a T_2 map of the sample fully saturated with brine and the lower plot is that of sample after complete injection of FMF. Each group corresponds to samples: (a) 230, (b) 56, (c) 37, (d) 134, (e) 53, and (f) carbonate.

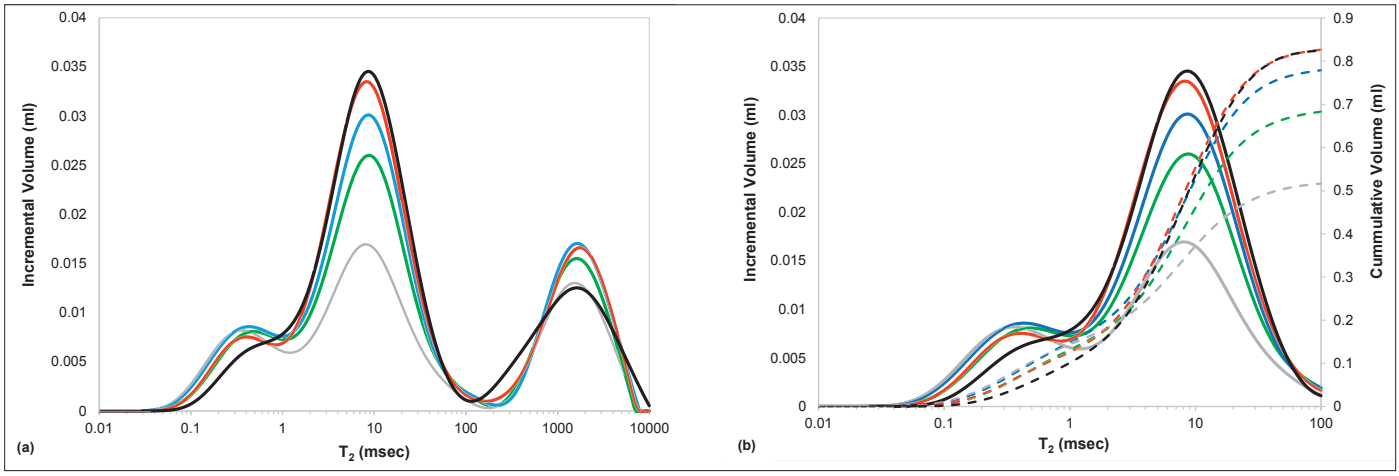

Fig. 9. T_2 distribution changes of sample 230 with continuous FMF injection. The volume of injected FMF is marked with gray (1 PV), green (2 PV), blue (3 PV), red (5 PV), and black (10 PV). (a) Complete T_2 distribution of sample 230 under different amounts of FMF injection. (b) T_2 distributions up to 100 msec from (a) have been plotted.

longer than 10 msec, Fig. 13b. With 0.8 PV of the FMF injection, it begins to invade into the micropore indicated by the development of the T_2 distribution component in between that of large and small pores, Fig. 13c. At 1 PV of the FMF injection, it invaded into all of the pores together, Fig. 13d. Finally, when 1.4 PVs of the FMF was injected, it only invaded into macropores and mesopores, which can be seen from the zoomed plot in Fig. 13f. Therefore, the invasion of the FMF into micropores was completed at the 1 PV of FMF injection. The shift of T_2 distribution of the small pore between 1 PV and 1.4 PVs the FMF injection indicates the increase of pore surface interaction with FMF. In other words, a reduced amount of FMF that invaded into the micropores diffuses back to the macropores and mesopores during continuous FMF injection. Therefore, the invasion of FMF occurs sequentially from macropores and mesopores to micropores of multiporous carbonate rocks of the current study. Since the BVI, T_2 components ≤ 100 msec, is composed of both micropores and mesopores, the above observation of a lower FMF displacement rate for BVI compared to BVM can be possible with an increased injected FMF volume.

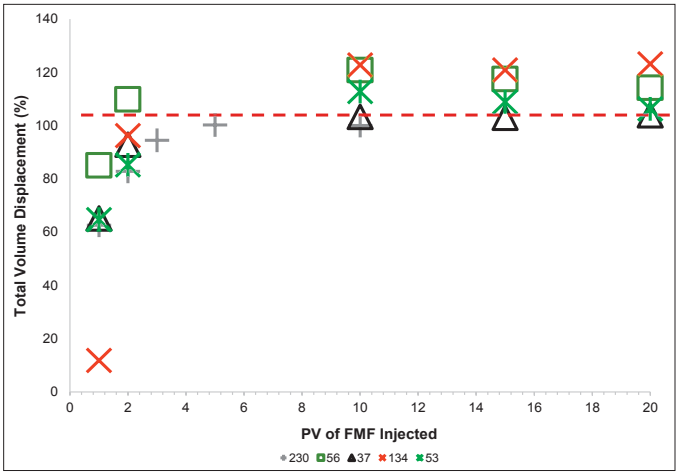

Fig. 10. The total volume displaced by FMF (%) vs. the total PV of FMF injected into five sandstone samples at 80 °C under 1,000 psi. The red dotted line is drawn to indicate 100% total volume displacement.

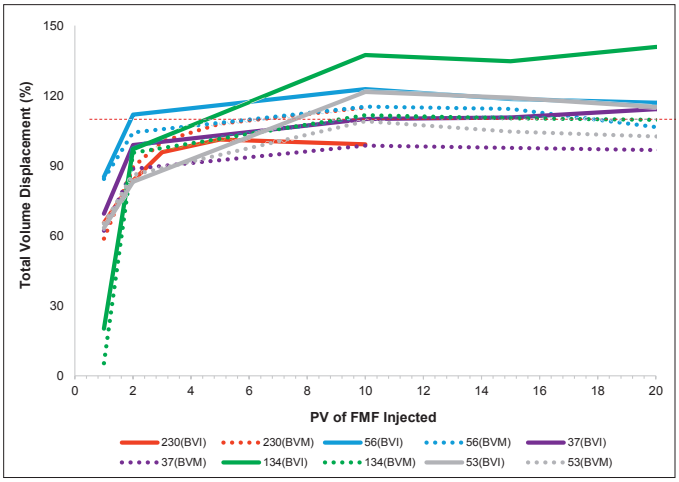

Fig. 11. Total BVI (solid line) and BVM (dotted line) displaced by FMF (%) vs. the total PV of FMF injected at 80 °C under 1,000 psi. The black dotted line is drawn to indicate 100% total volume displacement.

Temporal FMF Invasion Profile Analysis

The temporal FMF invasion profile study was conducted for the brine-saturated carbonate sample. Having an accurate FMF invasion profile with time will provide crucial information for correcting data from the NMR loggings, which were

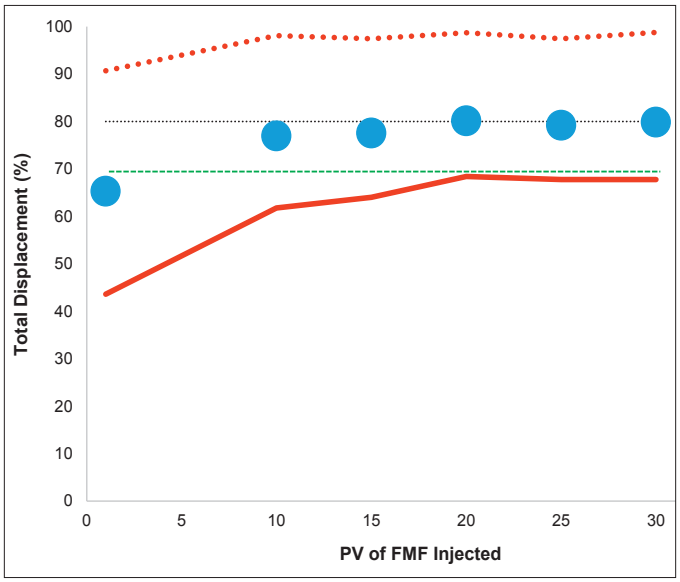

Fig. 12. The total volume displaced by FMF (blue filled circle) vs. the total PV of FMF injected into D_2O saturated Indiana limestone at 80 °C under 1,000 psi. The total BVM (red dotted line) and BVI (red solid line) displaced by FMF are also plotted. The black dotted line is drawn to indicate 100% total volume displacement. The green dotted line is drawn to indicate the plateau of the FMF displacement for BVM and BVI.

Temp (°C)	Pressure (psi)	FMF Injected Volume (PV)	Total Volume Displacement (%)	BVM Displacement (%)	BVI Displacement (%)
80	1,000	1	65.26	90.67	43.58
80	1,000	10	76.9	98.1	61.74
80	1,000	15	77.53	97.42	63.98
80	1,000	20	80.09	98.7	68.4
80	1,000	25	79.16	97.41	67.76
80	1,000	30	79.84	98.76	67.76

Table 6. The volumetric displacement of the FMF into D_2O saturated Indiana limestone at 80 °C and 1,000 psi. The T_2 cutoff used to determine BVI is 100 msec. Different amounts of FMF — up to 30 PVs — has been injected by differential pressure of 300 psi.

conducted at different times such as during logging while drilling (LWD) and post-drilling wireline logging. Since the FMF invasion profiles for BVM and BVI of brine-saturated carbonate are different, it has been selected for the current study.

The T_2 distribution was acquired at different times after 20 PVs of FMF was injected into the brine-saturated carbon-

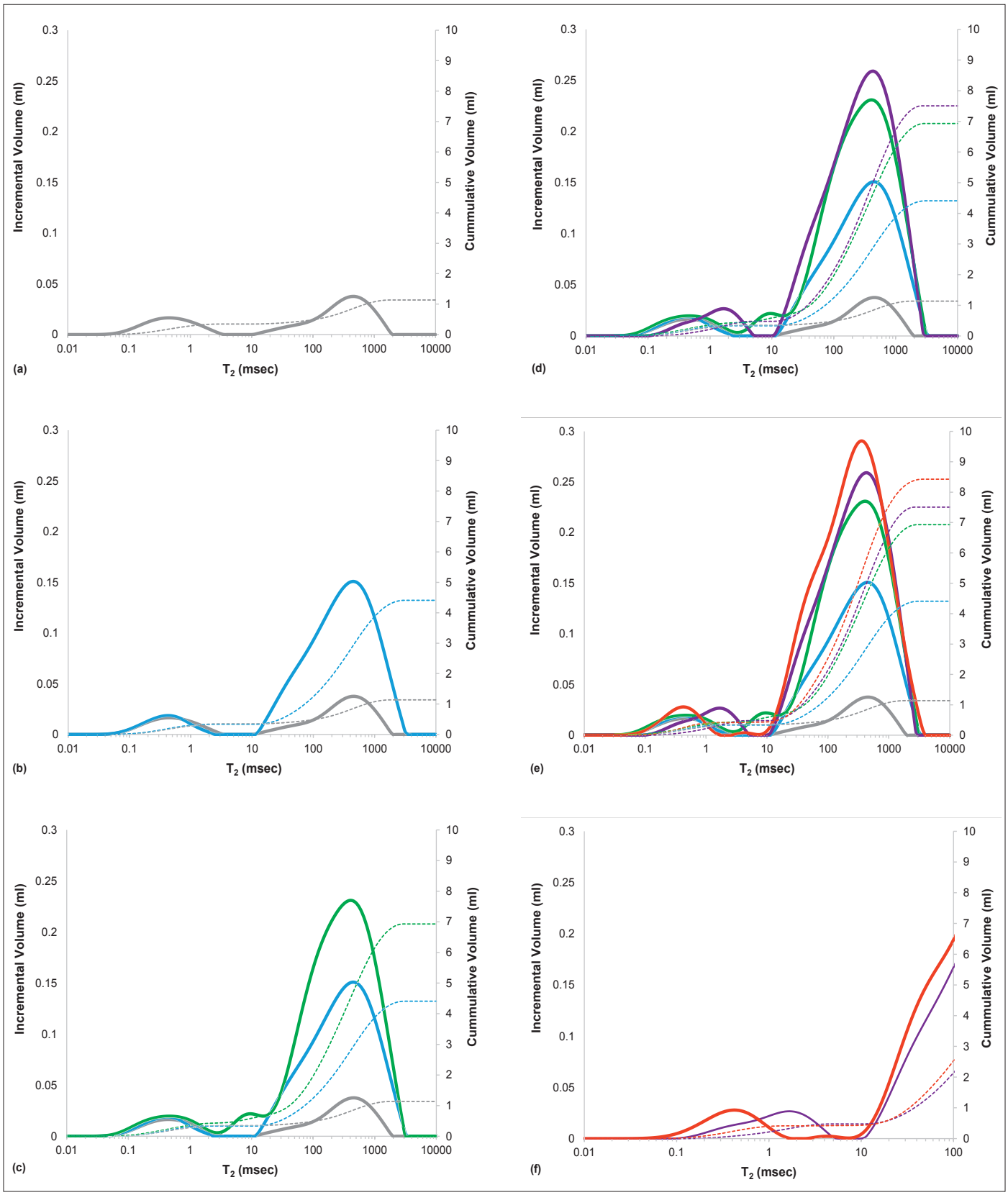

Fig. 13. The T_2 distribution change by injecting FMF into D_2O saturated Indiana limestone at 35 °C and 1,000 psi. The T_2 distribution of (a) D_2O saturated (gray), (b) 0.4 PV FMF injected (blue), (c) 0.8 PV FMF injected (green), (d) 1 PV FMF injected (purple), and (e) 1.4 PV FMF injected (red). The plot (f) is the zoomed T_2 distributions of 1 PV and 1.4 PV FMF injected for $T_2 \geq 100$ msec. The first and the second y-axis on the left and right side of each plot represent the incremental and the cumulative volume, respectively.

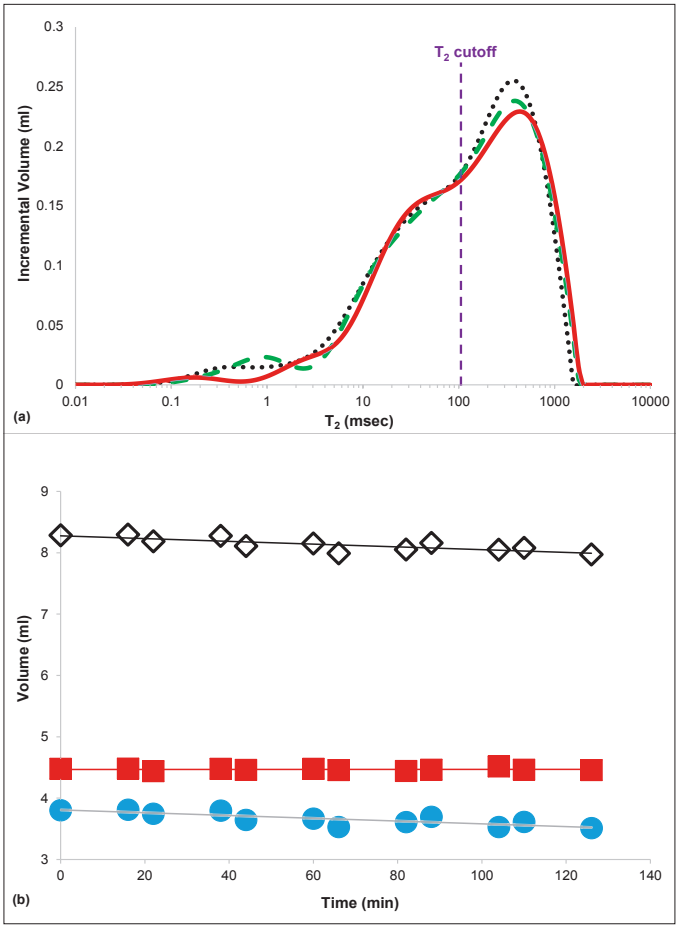

Fig. 14. (a) The T_2 distribution of brine (D_2O based) saturated Indiana limestone fully invaded by FMF measured after T = 0 min (black dotted line), T = 60 min (green dashed line), and T = 120 min (red solid line). (b) The BVM (red filled square), BVI (blue filled circle), and total volume (black empty diamond) changes with time. The T_2 cutoff to determine BVM and BVI is 100 msec, which is marked in the plot (a). The data are fitted linearly, which is shown on the plot.

ate by a differential pressure gradient of 300 psi. The volume changes both the BVM and BVI after the complete injection of the FMF were monitored, up to 120 min, Fig. 14. There is a small amount of fluid exchange between macropores and micropores, which can be observed by T_2 distribution changes in the zone between T_2 = 0.1 msec and T_2 = 10 msec, Fig. 14a. The total volume changes of BVM and BVI, however, is minimal with time, as can be seen from Fig. 14b. Therefore, FMF redistribution through diffusion is minimal with time unless other effects such as gravity segregation or pore structure alteration occurs.

CONCLUSIONS

The FMF invasion profiles for gas reservoir rocks with different degrees of pore connectivity were investigated. Two aspects of the most important information required for correcting NMR log data from the wells drilled with formate-based muds are the T_2 cutoff value and the pore dependent HI correction factors. The former is required for accurate determination of BVM, and the latter is needed for accurate porosity correction for BVM.

Five sandstone and one carbonate rock samples were chosen for the current study. All of them have multimodal pore systems with different degrees of connectivity between them, especially between sandstone and carbonate samples. The difference of BVM determined by using T_2 cutoffs from brine saturated and FMF saturated cores is less than ±5%. Therefore, in practice, the T_2 cutoff values acquired by conventional NMR lab measurement with brine-saturated cores can be used for NMR log data with any degree of FMF invasion.

For well-connected bimodal sandstones saturated with brine, FMF invaded all pores quite rapidly. Before the injection of 5 PVs of FMF with 300 psi pressure gradient, FMF displaced brine in all pores completely. Therefore, the same HI correction factor can be used to correct the porosity of both BVM and BVI. On the other hand, for trimodal carbonate with intermediate pore connectivity, the total PV displaced by FMF for BVM and BVI are 70% and 100%, respectively.

Therefore, different HI correction factors have to be applied to correct BVM and BVI. These HI correction factors can be calculated if the exact displacement volumes of the FMF in BVM and BVI are known, Eqn. 3. In the results, for multiporous brine-saturated sandstones, most likely all pores are well connected, and a single HI correction factor can be used to correct porosity of all pores. On the other hand, for multiporous brine-saturated carbonates, usually pores are connected with different degrees, pore-type specific — or volume-type specific — HI correction factors should be determined and applied to correct the porosity of different pore types.

Finally, time-dependent FMF invasion profiles have been investigated to correct NMR log data acquired in different times. The BVM and BVI have been monitored continuously up to 2 hours after 20 PVs of FMF injection, and no changes were observed. Therefore, the FMF exchange between pore systems are minimal and can be neglected. In other words, an identical HI correction factor can be applied to LWD and wireline NMR log data unless other effects occur, such as gravity segregation or sudden pore structure alterations.

ACKNOWLEDGMENTS

The authors would like to thank the management of Saudi Aramco for their support and permission to publish this article. The authors would also like to thank Dmitry Kosynkin, Mustafa Satrawi, and Badr Al-Zahrani from Saudi Aramco EXPEC ARC for laboratory measurements and sample preparations.

This article was presented at the SPE Kingdom of Saudi Arabia Annual Technical Symposium and Exhibition, Dammam, Saudi Arabia, April 24-27, 2017.

REFERENCES

1. Simpson, M.A., AbdRabAlreda, S.H., Al-Khamees, S.A.,

Zhou, S., et al.: "Overbalanced Pre-Khuff Drilling of Horizontal Reservoir Sections with Potassium Formate Brines," SPE paper 92407, presented at the Middle East Oil and Gas Conference, Manama, Bahrain, March 12-15, 2005.

2. Simpson, M.A., AbdRabAlreda, S.H., Forman, D., Guzman, J., et al.: "Application and Recycling of Sodium and Potassium Formate Brine Drilling Fluids for Ghawar Field HT Gas Wells," *Saudi Aramco Journal of Technology*, Summer 2009.
3. Bungert, D., Maikranz, S., Sundermann, R., Downs, J., et al.: "The Evolution and Application of Formate Brines in High Temperature/High-Pressure Operations," SPE paper 59191, presented at the IADC/SPE Drilling Conference, New Orleans, Louisiana, February 23-25, 2000.
4. Pedersen, B.K., Pedersen, E.S., Moriss, S.L., Constable, M.V., et al.: "Understanding the Effects of Cesium/Potassium Formate Fluid on Well Log Response — A Case Study of the Kristin and Kvitebjorn Fields, Offshore Norway," SPE paper 103067, presented at the SPE Annual Technical Conference and Exhibition, San Antonio, Texas, September 24-27, 2006.
5. Forsyth, D., Al-Musharfi, N.M. and Al-Marzooq, A.M.: "Tight Gas Petrophysical Challenges in Saudi Aramco," SPE paper 149048, presented at the SPE/DGS Saudi Arabia Section Technical Symposium and Exhibition, al-Khobar, Saudi Arabia, May 15-18, 2011.
6. Guo, P., Gilchrist Jr., W.A., Page, G., Wills, P., et al.: "Interpretation of Nuclear Logs in Formate-based Drilling Fluids in a North Sea Well," SPWLA paper 2002-BBB, presented at the 43rd SPWLA Annual Logging Symposium, Oiso, Japan, June 2-5, 2002.
7. Galford, J., Truax, J. and Moake, G.L.: "Borehole and Formation Invasion Effects of Formate-Based Mud Systems on Nuclear Logs," SPWLA paper 2005-LL, presented at the 46th SPWLA Annual Logging Symposium, New Orleans, Louisiana, June 26-29, 2005.
8. Al-Harbi, A.A., Ersoz, H. and AbdRabAlreda, S.H.: "Influence of Sodium/Potassium Formate-based Drilling Fluids on Nuclear Logs," SPE paper 94693, presented at the SPE Latin American and Caribbean Petroleum Engineering Conference, Rio de Janeiro, Brazil, June 20-23, 2005.
9. Zhang, J., Chen, J-H., Thorsen, A.K., Constable, M., et al.: "NMR Investigation of Invasion Process of Formate Mud in Sandstone Cores," SCA paper 2011-52, presented at the International Symposium of the Society of Core Analysts, Austin, Texas, September 18-21, 2011.
10. Chen, J-H., Zhang, J., Thorsen, A.K., Constable, M., et al.: "Method for Correcting NMR Porosity in Formate Brine Invaded Formations," SPWLA paper 2011-SSS, presented at the 52nd SPWLA Annual Logging Symposium, Colorado Springs, Colorado, May 14-18, 2011.
11. Coates, G.R., Marschall, D., Mardon, D. and Galford, J.: "A New Characterization of Bulk-Volume Irreducible Using Magnetic Resonance," SPWLA paper 1997-QQ, presented at the 38th SPWLA Annual Logging Symposium, Houston, Texas, June 15-18, 1997.

BIOGRAPHIES

Dr. Hyung T. Kwak joined Saudi Aramco in April 2010 as a Petroleum Engineer with Saudi Aramco's Exploration and Petroleum Engineering Center – Advanced Research Center (EXPEC ARC). He was a member of the pore scale physics focus area (2010 to 2012) and is currently a member of the SmartWater flooding focus area of the Reservoir Engineering Technology Division. Hyung's current research focus is on seeking deeper understanding of the fluid-rock interaction through modeling and experiments that involve injecting SmartWater into carbonates. Since joining Saudi Aramco, he has been involved in various improved oil recovery and enhanced oil recovery (EOR) research projects, such as SmartWater Flooding, CO_2 EOR, and chemical EOR. Prior to Hyung's current position, he was a Research Scientist at Baker Hughes, where the main area of his research was developing low-field NMR/MRI technology.

He received his B.S. degree in Chemistry from the University Pittsburgh, Pittsburgh, PA, in 1996, and his Ph.D. degree in Physical Chemistry from Ohio State University, Columbus, OH, in 2001.

Before moving into the oil and gas industry, Hyung worked as a postdoctoral fellow for 2 years on the project to develop the world's largest wide bore superconducting magnet, 900 MHz, for the nuclear magnetic resonance spectrometer at the National High Magnetic Field Laboratory.

Dr. Gabor G. Hursan is a Petrophysicist in Saudi Aramco's Reservoir Description and Simulation Department. He is Saudi Aramco's focal point for nuclear magnetic resonance (NMR) well logging and formation evaluation. Previously, Gabor worked as a Scientist and Project Leader on NMR technology development at Baker Hughes for 10 years.

He has published several papers and patents, teaches classes in NMR logging and is a reviewer for technical publications. Gabor is a member of the Society of Petroleum Engineers (SPE) and the Society of Petrophysicists and Well Log Analysts (SPWLA).

He received his M.S. degree in Geophysical Engineering from the University of Miskolc, Miskolc, Hungary, and his Ph.D. degree in Geophysics from the University of Utah, Salt Lake City, UT.

Dr. Ahmad M. Al-Harbi is a Petroleum Engineer in the Pore Scale Physics Group of the Reservoir Engineering Technology Division in Saudi Aramco's Exploration and Petroleum Engineering Center – Advanced Research Center (EXPEC ARC). His current research focus is seeking solutions for ultimate recovery from Saudi Arabian reservoirs by acquiring deeper understandings of fluid dispersion, pore connectivity, and fluid-rock interaction in porous media.

Ahmad has 15 years of experience in the oil industry with Saudi Aramco. He has been involved with various enhanced oil recovery (EOR) research projects, such as chemical EOR.

In 2001, Ahmad received his B.S. degree in Chemical Engineering from King Fahd University of Petroleum and Minerals (KFUPM), Dhahran, Saudi Arabia, and in 2013, he received his Ph.D. degree in Petroleum Engineering from the University of Calgary, Calgary, Alberta, Canada.

Jun Gao joined Saudi Aramco in October 2015 and is currently working in Saudi Aramco's Exploration and Petroleum Engineering Center – Advanced Research Center (EXPEC ARC) as a Petroleum Scientist with the Reservoir Engineering Technology Division. Prior to joining Saudi Aramco, he worked as a Research Scientist on multiple advanced enhanced oil recovery (EOR) studies for oil companies at Tomographic Imaging and Porous Media Laboratory (TIPM lab) in Perm Inc. and the University of Calgary. Prior to that, Jun worked as a Petroleum Engineer on national chemical EOR research projects at the Geological Scientific Research Institute, Shengli Oil Field Company, and China Petroleum & Chemical Corporation (Sinopec).

He has over 25 years of research experience in special core analysis and EOR, including chemical, thermal, and carbon dioxide techniques, assisted by imaging technologies such as X-ray computer tomography and nuclear magnetic resonance imaging.

Jun received his B.S. degree in Physics from Shandong University, Shandong, China, his B.Eng. degree in Petroleum Engineering from the China University of Petroleum (East China), Qingdao, China, and his M.S. degree in Petroleum Engineering from the University of Calgary, Calgary, Alberta, Canada.

Dr. Shouxiang M. "Mark" Ma is a Senior Consultant overseeing research, technology, and professional development with the Reservoir Description Division of Saudi Aramco. He serves on the Petroleum Engineering Special Core Analysis Council and the Technologist Development Program Committee, and he champions the Logging Excellence Professional Network. Mark was Supervisor of the Petrophysical Support & Study Unit, a petrophysics professional development advisor at the Upstream Professional Development Center, and Lead Engineer for logging operations.

Before joining Saudi Aramco in 2000, he worked at the Exxon Production Research Company, Wyoming Western Research Institute, New Mexico Petroleum Recovery Research Center, and China Yangtze University.

Mark has authored or coauthored more than 70 technical papers and holds several patents. He has served on the JPT Editorial Committee since 2015, chairs the 2018 Society of Petroleum Engineers (SPE) Annual Technical Conference and Exhibition Formation Evaluation Committee, and was chairperson of the 2012-2013 SPE Formation Evaluation Award Committee. Mark is a Vice President of the newly established Saudi Arabia Chapter of the Society of Petrophysicists and Well Log Analysts.

Mark received his B.S. degree from the China University of Petroleum, Shandong, China, and his M.S. and Ph.D. degrees from the New Mexico Institute of Mining and Technology, Socorro, NM, all in Petroleum Engineering.

Use of a Novel Coiled Tubing Real-Time Downhole Flow Measurement Tool to Evaluate Matrix Stimulation Treatment for the First Time Worldwide

Ramiro Cedeño, Ibrahim K. Al-Thwaiqib, Danish Ahmed, and Rodrigo Sa

ABSTRACT

This article discusses the first worldwide use of a novel coiled tubing (CT) real-time downhole flow measurement tool to evaluate the effectiveness of a matrix stimulation intervention performed in a saltwater disposal (SWD) well by comparing the acquired data with the injection profile obtained via a conventional production logging tool (PLT) prior to the treatment.

When SWD wells show a decrease in injectivity, the operator's preference is to conduct stimulation treatments or reperforate target intervals before deciding on a costly workover operation. The decision to intervene is often made based on injection profiling performed using PLTs along with injectivity index calculations. This evaluation represents an additional expense that typically requires significant time and logistical coordination. Alternatively, a CT real-time downhole flow measurement tool can be used to conduct — in a single run — injection profiling, which enables optimization of the treatment execution before conducting post-stimulation injection profiling to evaluate the effectiveness of the treatment.

With the recent introduction of the CT real-time downhole flow measurement tool to facilitate the optimization and evaluation of matrix stimulation treatments, new concerns arose as to whether an actual correlation existed between the tool and the existing injection profiles obtained through conventional PLTs. Until now, there has been no field data to compare both approaches. During a recent matrix stimulation treatment on a SWD well, it was decided to perform a correlation between the data acquired by both tools before the execution of the acid stimulation. The correlation between the injection profile obtained via the CT real-time downhole flow measurement tool and the injection profile obtained via a PLT was remarkably similar. Additionally, it was confirmed during the treatment that the data acquired by the CT real-time downhole flow measurement tool can be further used to optimize the stimulation treatment, before performing another injection profile after the stimulation. Surface and downhole parameters acquired during the treatment were also used to model the well performance via nodal analysis.

This article shows the world's first example of the correlation of the injection profile obtained by the CT real-time downhole flow tool to the injection profile obtained via a PLT. This article focuses on the benefits of monitoring downhole parameters during CT acid stimulations. It also highlights the added value brought by the CT real-time downhole flow measurement tool and how its output correlates to PLT data.

INTRODUCTION AND BACKGROUND

The associated water produced along with hydrocarbons is reinjected into the same reservoir through saltwater disposal (SWD) wells. Acid stimulation treatments and reperforation operations are regularly conducted in SWD wells because it is critical for the operation to have the ability to properly dispose of such produced water and to maintain a healthy overall injection pressure in the disposal system to prevent operational disturbances in the surface facilities.

The main goal of the acid stimulation treatments is to create new pathways within the formation and bypass the near wellbore damage[1]. The main target from reperforation operations is to improve the injectivity index through enhancing the perforation efficiency via upgrades on shot density, phase angle, penetration depth, and perforation diameter. In case neither of the mentioned approaches meet the required goals, a workover operation is considered.

The candidate well discussed in this article is a cased, vertical SWD well (Well-A) drilled and completed as a water injector in 1982. Two workover operations were conducted, one in 1983 and one in 2015, the last one was to repair a casing leak and install 4½" tubing. In addition, three acid stimulations were conducted. Some of the most important events and key information of the candidate well are presented in Fig. 1.

After conducting the well performance evaluation on Well-A, it was recommended to first proceed with an underbalanced reperforation of the current open intervals, which had been perforated more than 30 years ago with four shots/ft, to improve perforation efficiency. It should be noted that the well already had three perforated intervals, and the plan was to reperforate the top and second interval, extending a portion of the top interval to take advantage of a highly permeable zone identified through a detailed analysis of the open hole logs. The reason behind the decision of focusing exclusively on the upper two perforated intervals was their relatively high permeability and porosity. It was also recom-

mended to conduct an injection log to determine the injection profile and actual status of the perforation efficiency before any attempt of reperforation to optimize the perforation operation and to conduct the injection and falloff tests before and after perforations. A dynamic underbalanced reperforation, injection logging, and well testing operations were conducted safely and successfully on the well.

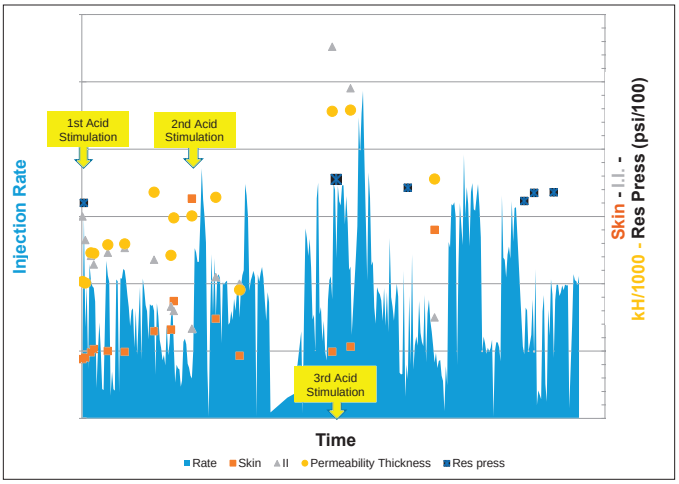

Fig. 1. Historical events and parameters for the vertical SWD well, Well-A.

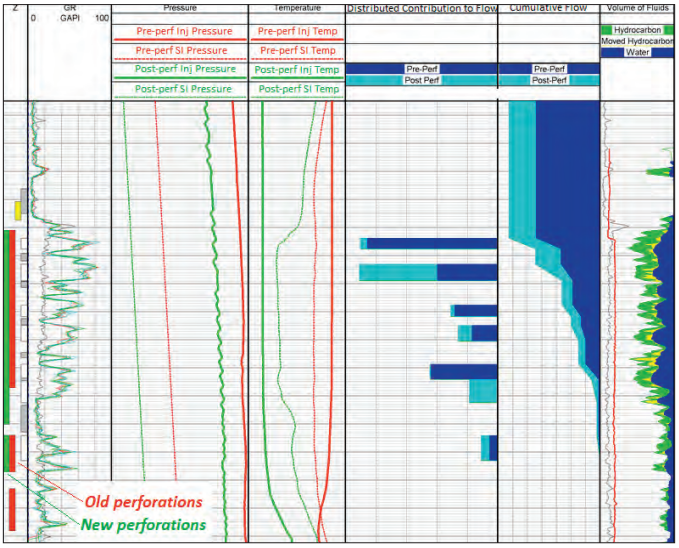

Fig. 2. Qualitative comparison of a pre- and post-perforation injection log.

Figure 2 shows the old vs. the new perforations and the pre-perforation injection profile vs. the post-perforation injection profile, whereas Fig. 3 shows the pressure transient test analysis conducted before and after reperforations.

An increase in the injectivity index from 10.5 stock tank barrels (STB)/psi to 12.8 STB/psi was noticed after reperforation, which represented an increase in the injection rate of 117%. This gain is understood by the fact that the improvement on the permeability thickness was caused by the extension of the top interval. Based on injection logging, it was confirmed that most of the injected water was taken by the upper set of perforations and no crossflow was observed. In addition, the new measured gamma ray (GR) log showed higher values than the reference GR log (black curve), which may be an indication of scale deposition in front of the perforations. Despite the clear improvement in the injectivity, the operator decided to proceed with a matrix stimulation job to increase even further the injectivity on the well, since the calculated skin factor of 8.8 from the falloff data showed no major change after the dynamic underbalanced reperforation, Fig. 3.

JOB OBJECTIVES AND OPPORTUNITIES

There were three main objectives in this well intervention:

1. To effectively reduce the skin factor in the candidate well.
2. To get the noncontributing (noninjection) zones to a contribution/injection stage, resulting in a homogeneous profile.
3. To identify a methodology to be used instead of the conventional step-rate tests and production logging operations to evaluate injection performance and determine an injection profile in the target intervals.

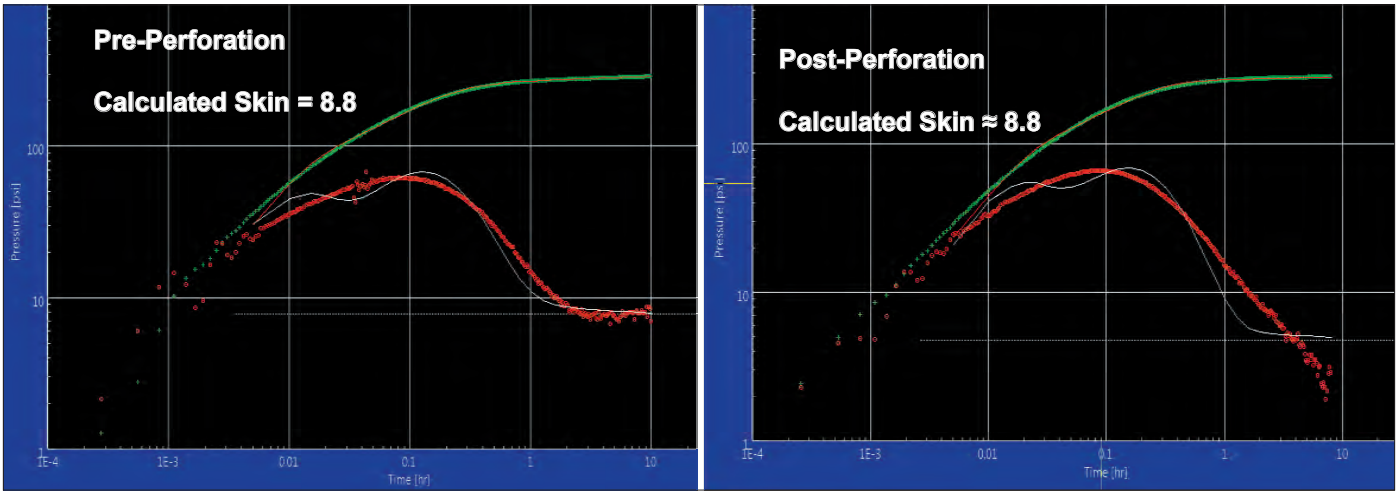

Fig. 3. Comparison of the pressure transient test analysis conducted before and after reperforation.

The evaluation team recognized this operation as a tremendous opportunity to complement the recent conducted injection profiling logs with the coiled tubing (CT) real-time downhole flow measurement tool.

The matrix stimulation could have been pumped via bullheading to meet the first and second job objectives, by utilizing appropriate diversion to avoid the high intake zone to take most of the stimulation fluids and leave the rest of the interval poorly stimulated. Therefore, for the sake of optimizing the stimulation fluid placement to effectively reduce the skin and to address the job objectives, one needed to use a tool that could give similar output as an injection log while still providing good stimulation and diversion capabilities. CT with real-time telemetry was seen as a key component of a solution, which allowed for spotting the fluids at desired depths but would also provide downhole pressures, temperatures, GR, casing collar locator (CCL), and optical distributed temperature sensing (DTS) measurements in real time.

It is important to mention that the DTS on its own could also have been used for the optimization of a matrix stimulation treatment in real time along with its injection log determination techniques of injection and warmup and hot water interface velocity measurement. In this particular case, it also presented the following limitations[2]:

- If there was crossflow, the warmback technique could not be used.
- If the injection rate could not be kept constant, then the hot water interface injection technique could not be used.
- The CT could become differentially stuck during DTS acquisition.

Therefore, considering the above-mentioned limitations of DTS, it was decided to use the novel CT real-time downhole flow measurement tool.

INTRODUCTION TO THE CT REAL-TIME DOWNHOLE FLOW MEASUREMENT TOOL

Figure 4 shows the novel CT real-time downhole flow measurement tool, which is a flow through modular and acid compatible tool dedicated to services with CT, which measures pressure (p-psi) inside the coil, and outside (i.e., in the annulus), downhole flow velocity, and fluid direction with the additional modules of temperature (T) and GR. Figure 4 only shows the upper module of the CT real-time downhole flow measurement tool. The lower module below the flow exit port can be added depending on job objectives, and then the module of the CCL can also be added. The upper or lower module of the CT real-time downhole flow measurement tool has a set of four sensors referred to as A, B, C, and D, placed at 90° apart to cover the tool and wellbore circumference. They are situated away from the nozzles to avoid any jetting effects.

The tool provides real-time monitoring of the placement process during matrix stimulation treatments. This real-time information can be used to make corrective actions during the treatment.

The main benefits of the selected architecture is the robustness of the bottom-hole assembly (BHA), which supports high compressive loads, does not have a centralizer, arms, spinners, or protruding elements, and can be used in acid or hydrogen sulfide environments.

One of the key features of the tool is the temperature probe

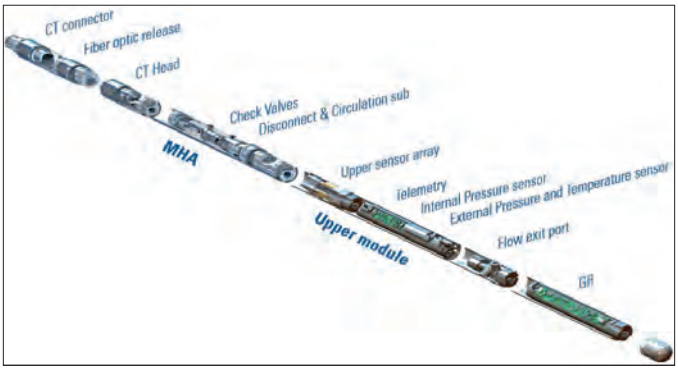

Fig. 4. The novel CT real-time downhole flow measurement tool.

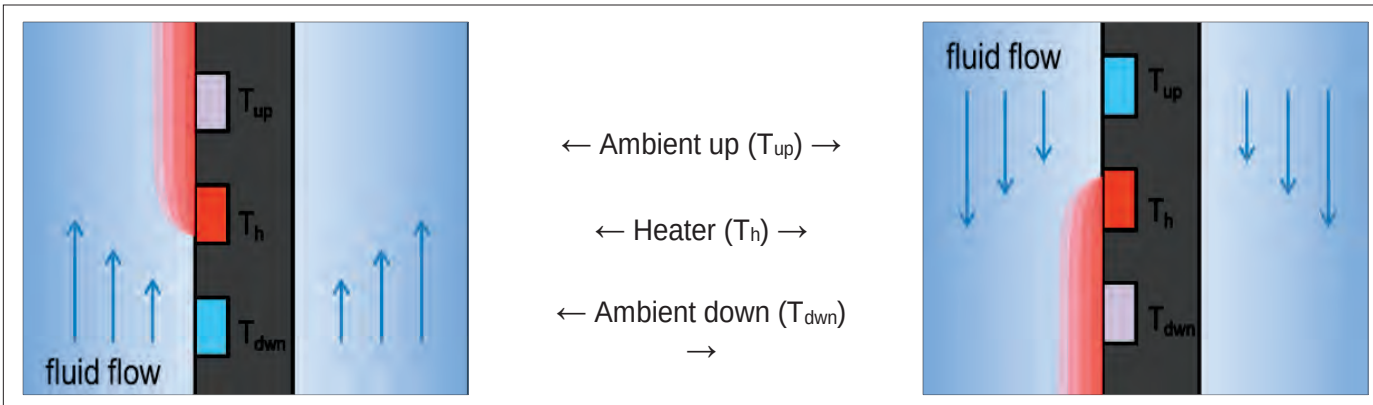

(a) Upward flow: $T_{up} > T_{dwn}$ (b) Downward flow: $T_{up} < T_{dwn}$

Fig. 5. The temperature probe kit of the CT real-time downhole flow measurement tool[2].

kit, which is used to measure the velocity before, during, and after the treatment. This information provides the basis to calculate the flowing rates for each of the different stages considered during the intervention.

Each sensor — A, B, C, and D — has three temperature probes, Fig. 5.

- The top (T_{up}) and bottom (T_{dwn}) sensors are used as temperature probes.
- The middle sensor (Th) is kept at a constant temperature excursion ΔT over the temperature of the fluid: $Th = Tf + \Delta T$ where Th is the heater temperature and Tf is the fluid temperature.

The power, P, is used to heat the middle probe and is dissipated in the fluid, whereas the fluid velocity, v, is a function of the dissipated power: $v = F(P/\Delta T)$.

Then, it is possible to state[2]:

- The amount of the dissipated power per 1° of the temperature excursion, $P/\Delta T$, depends on the fluid velocity.
- The exact functional relationship between the dissipated power and the fluid velocity can be obtained by performing a downhole calibration.
- Direction detection is determined by calculating the temperature difference between the ambient probes $T_{up} - T_{dwn}$. Positive values of this difference indicate an upward flow, and negative values indicate a downward flow.

INTERVENTION DESIGN

The intervention was designed for a single run in which the CT BHA would measure the downhole flow while conveying the high-pressure rotating jetting tool that would perform the stimulation treatment across the perforated intervals. Based on the data collected before initiating the design, it was possible to identify that all of the treatments would go to the top of the perforation interval, despite the fluid type. This would leave the middle and bottom of the perforation zone as noncontributing, thereby reducing the potential of the interval, which could significantly decrease the injection profile in this well.

A tool calibration for the CT real-time downhole flow tool was designed to be performed as a first step to ensure correct measurements in the annulus for different flow regimes. Because the well had multiple perforation intervals with different injection profiles, a depth correlation was also performed to accurately quantify the flow profile for each perforated depth.

Since the last acid stimulation on the well was conducted more than 15 years ago, and after conducting a scale prediction evaluation that suggested a high probability for deposition of calcium carbonate and calcium sulfate, by using a geochemical analysis from the injection water, a multifunctional solvent was recommended — primarily to restore the relative permeability and dissolve scale deposits. A combination of viscoelastic self-diverter acid, emulsifier acid, and high-strength hydrochloric acid was recommended to be pumped in stationary mode on each station, or while the CT was moving to effectively stimulate the noncontributing zones.

JOB EXECUTION

Table 1 presents a typical intervention workflow for a proposed operation planned to be executed by a combination of using the novel CT real-time downhole flow measurement tool and high-pressure rotating jetting.

The CT real-time downhole flow measurement operation comprised four main steps:

1. Obtain the injection profile before pumping the stimulation treatment fluids.
2. Pump the multifunctional solvent to remove scale and determine the injection profile.
3. Pump the main stimulation treatment.
4. Obtain the post-stimulation injection profile.

These steps are described next.

Step 1: Conduct the Injection Profile before Pumping the Stimulation Treatment Fluids

Quality control and quality assurance of the CT real-time downhole measurement tool and high-pressure rotating jetting tool was performed prior to running the tools in the well. CT was run in hole; after the tool reached the desired depths, the calibration was performed to measure the accurate direction of fluid exiting the high-pressure rotating jetting tool and velocity of fluid pumped in the annulus of the CT and tubing/casing.

The CT depth was correlated using a GR reference log to assure correct CT depth during injection profiling before pumping any stimulation fluids. After the CT depth was correlated and the CT real-time downhole flow rate measurement tool was calibrated, the CT was run in hole across the perforated intervals while injecting water in the annulus of the CT and tubing.

Figure 6 shows the injection profile determination (third channel from right) from the CT real-time downhole flow measurement tool, while reciprocating and making stations (red dots) across the perforated interval during annulus pumping vs. previous conducted injection profiles that were conducted after re-perforation just before this intervention from the injection logging tool (last channel on right). The match between the injection profile determined from the CT real-time downhole measurement tool and the injection profile determined from the injection log is particularly good as both were conducted at almost the same injection wellhead

Job Design Phase				
1. Check CT simulations, if able to reach TD. Check minimum restriction. If cannot reach TD, get client consent on profiling interval until the maximum depth reached. Conduct well clean out as necessary.	2. Check BHT limit to determine the temperature rating of fiber and novel CT real-time downhole flow measurement tool. If the temperature limit is exceeded, determine the alternative option of running DTS/PLT.	3. Check available IDs in the well to determine the calibration rates of novel CT real-time downhole flow measurement tool. Rates should not exceed the velocity threshold of the tool. If the known ID is not available, calibration may need to be performed on the surface in the known ID risers.	4. Check the depth correlation reference, i.e., tubing tally, casing markers, gamma ray, etc. If not available, velocity variation provided by novel CT real-time downhole flow measurement tool may be used as a reference. Velocity will vary in downhole conditions while passing the completion items of different sizes.	5. Check pressure limitations. If the wellhead pressure is too high, the well needs to be filled to lower the wellhead pressure.

Job Execution Phase	
Pre-Job	**Pre-Stimulation/Post-Stimulation**
Conduct fiber optics QA/QC.	Determine if CT reaches the TD.
Conduct CT real-time downhole flow measurement tool QA/QC. Check probe's response to offset correction.	Determine if probes respond to offset correction.
Record wellhead pressure and determine if the well is sub-hydrostatic.	Conduct downhole calibration of novel CT real-time downhole measurement tool via CT movement, pumping from annulus or pumping from the CT.
Determine if the well needs displacement with a known 1 phase fluid.	Perform depth correlation.
Ensure acquisition/hardware synchronization.	Perform injection profiling via pumping from annulus and while CT POOH.
Ensure working of pressure/rate gauges.	Perform injection profiling via pumping from annulus and while conducting CT stations.
Ensure the pumps are primed.	
Perform fluid's QA/QC.	
Perform high-pressure jetting tool function test.	

Table 1. The typical intervention workflow when using the novel CT real-time downhole flow measurement tool

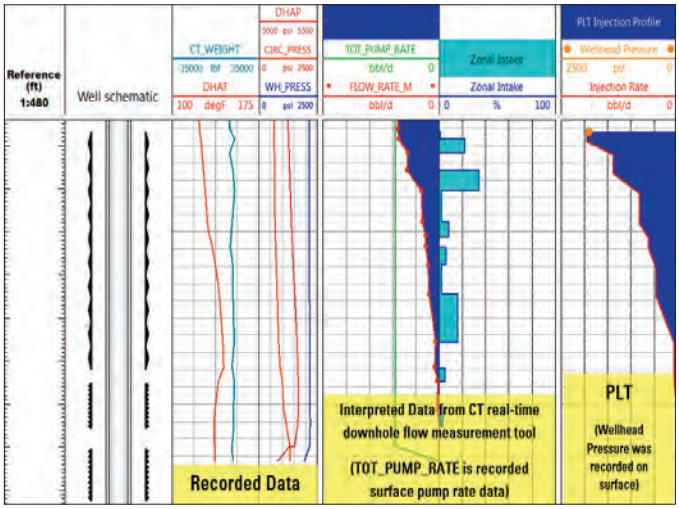

Fig. 6. Injection profile determination by the CT real-time downhole flow measurement tool prior to pumping the multifunction solvent and comparison with the injection profile determined from the injection logging tool.

pressure, which provides a good indication of the degree of accuracy of the CT downhole tool. Figure 6 also shows the data plotted vs. depth, whereas some of the data was actually time-based such as the TOT_PUMP_RATE.

This is the first time worldwide where such an exercise of correlating an injection profile from the CT real-time downhole measurement tool and the injection logging tool has been done.

Despite the promising match of the injection profile noticed in this comparison, the evaluation team recognized the difference in absolute injection rate figures. This situation is understood by the reduction in the cross-sectional injection flowing area from the initial production logging tool (PLT) conducted with wireline, when compared to the effective flowing area during the injection through the annulus of the CT and tubing.

To provide an estimation of the impact on the injection flow rate under this new scenario, nodal analysis was conducted. First, nodal analysis was conducted for the wireline PLT, fol-

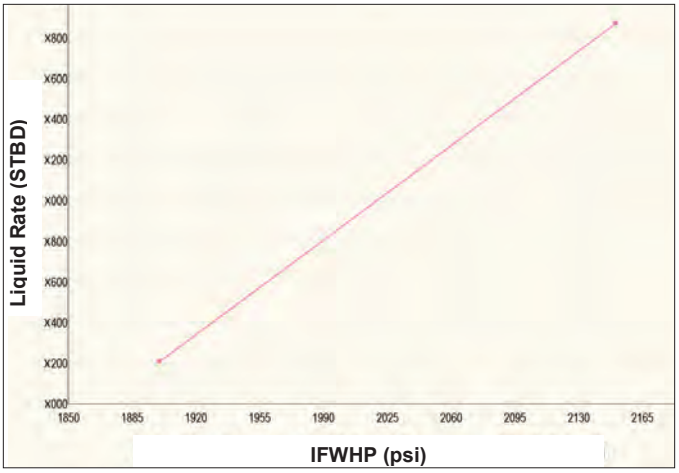

Fig. 7. Sensitivity plot for injection flow rate for two different IFWHPs.

lowed by the nodal analysis at a similar injection of the flowing wellhead pressure (IFWHP) as seen during the operation with the novel CT real-time downhole flow measurement tool.

Figure 7 presents the sensitivity plot for this simulation; it was possible to establish an increase by 27% in the injection flow rate after increasing the IFWHP by 250 psi. Having said that, it was possible to estimate a 64% reduction in the injection flow rate due to the reduction in the cross-sectional flowing area. This reduction is applicable only for the particular case of Well-A, under the observed conditions of the IFWHPs, tubular diameters for both the tubing and the CT, the reservoir parameters, and the calculated skin factor. It is advisable to undertake such calculations for each case for future operations.

Step 2: Pump the Multifunctional Solvent to Remove Scale and Determine the Injection Profile

A multifunctional solvent was pumped while reciprocating across the perforated intervals to remove organic deposits and scales. After the multifunctional solvent was pumped, an injection profile was conducted over 15 stations across the perforated zone while pumping at the same pump rate as before from the annulus of the CT and tubing.

Figure 8 shows the injection profile determination from a CT real-time downhole flow measurement tool after pumping the multifunctional solvent and its comparison to the injection profile determined before pumping the multifunctional solvent, and with the injection profile determined from the injection logging tool. A slight improvement of the injection profile at the top of the upper perforated interval can be seen.

Table 2 shows the definition of the curves presented in the depth-based plots in Figs. 8 and 9.

Step 3: Pump the Main Stimulation Treatment

After the injection profile was recorded by the CT real-time downhole flow measurement tool and the flow rate was compared before and after the multifunctional solvent and with the injection logging tool, the main treatment was slightly redesigned on location to improve the probability of effectively stimulating the noncontributing zones by pumping a viscoelastic diverter in the intake zones. Because data from the preliminary PLT was available, the treatment had already been customized for the candidate well; therefore, no major changes

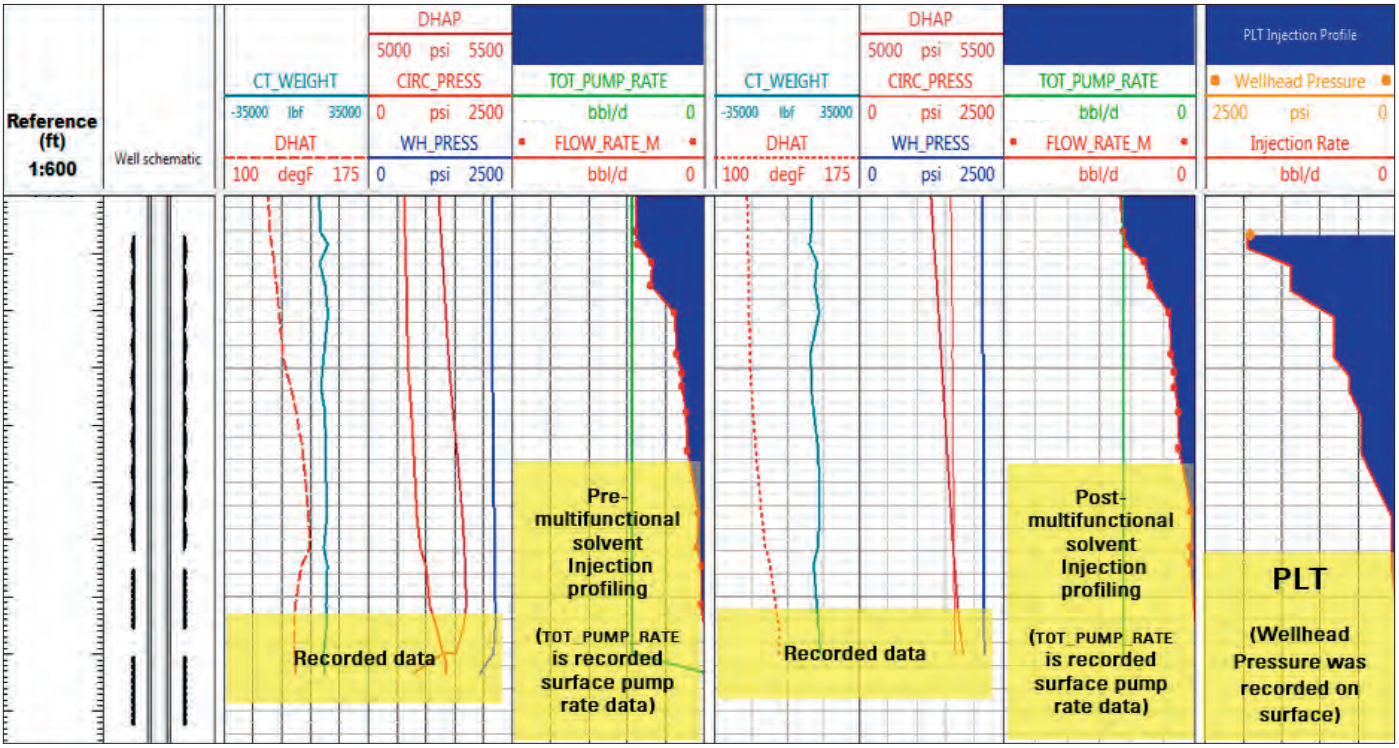

Fig. 8. Injection profile determination by the CT real-time downhole flow measurement tool before and after pumping the multifunction solvent and comparison with the injection profile determined from the injection logging tool.

Recorded Data	
1st Channel	Well schematic showing perforated zone intervals.
2nd Channel	CT weight (light blue), downhole temperature gauge (red DHAT).
3rd Channel	Wellhead pressure (blue), circulation pressure (red) and downhole annular pressure (dark red DHAP).
Interpreted Data	
1st Channel	Total pump rate (green) and flow rate — injection rate (red line filled with blue) from the novel CT real-time downhole measurement tool.
2nd Channel	The % of injection for each intake zone (zonal contribution).
PLT Data	Total injection rate (red line filled with blue) and WHP — PLT injection profile.

Table 2. Curve definitions of the depth-based plots in Figs. 8 and 9

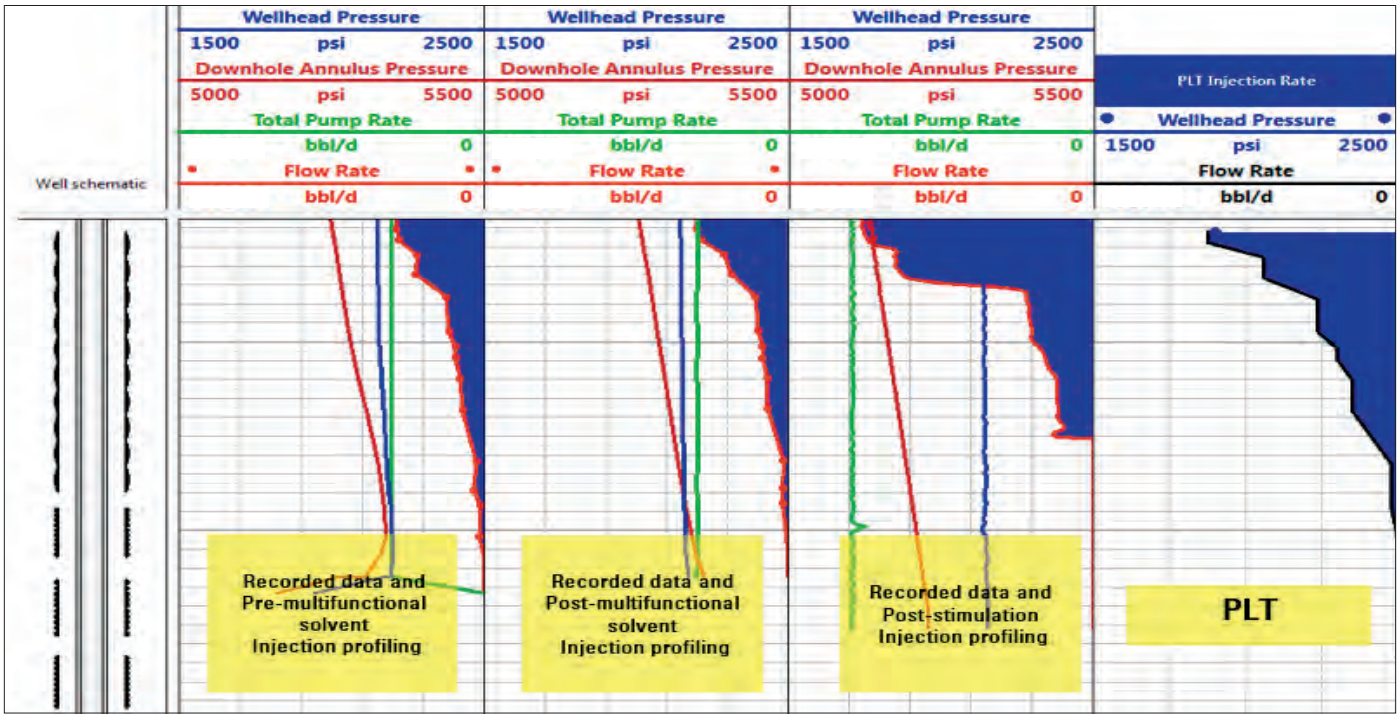

Fig. 9. Injection profile determination by the CT real-time downhole flow measurement tool before and after pumping the multifunction solvent, after pumping stimulation treatment and comparison with the injection profile determined from the injection logging tool.

were implemented on the overall treatment for this particular case. In situations in which such information is not available, a fine-tuning of the original proposed treatment can be executed within 3 hours — on location — giving the opportunity for improvements in operational time, pumping volumes, viscoelastic diverter placement, and acid concentrations, which may lead to substantial reductions in operating costs and increase in overall treatment efficiency.

The perforation interval was divided into seven zones, and the main treatment was performed with emulsifier acid. High strength acid was used as a spacer, and a viscoelastic self-diverter acid was pumped to divert the theft zone.

The lower perforation intervals were the main target for stimulation during the acid treatment to improve the injection profile.

Step 4: Obtain the Injection Profile after Pumping the Matrix Stimulation Treatment

After pumping the matrix stimulation treatment via CT, injection profiling was conducted utilizing the CT real-time downhole flow measurement tool. CT passes were made in addition to conducting the stations while pumping in the annulus to record the data. Figure 9 presents the injection profiling conducted after pumping the matrix stimulation treatment and its comparison to the injection profile determined before and after pumping the multifunctional solvent, and with the injection profile determined from the injection logging tool. The injection profile showed that the upper perforated zone interval was taking most of the injection. There was also a second high intake interval in the middle of the top perforated interval. The lower interval was not contributing to the injected fluid because most of the injection shifted to the top of the top perforated interval.

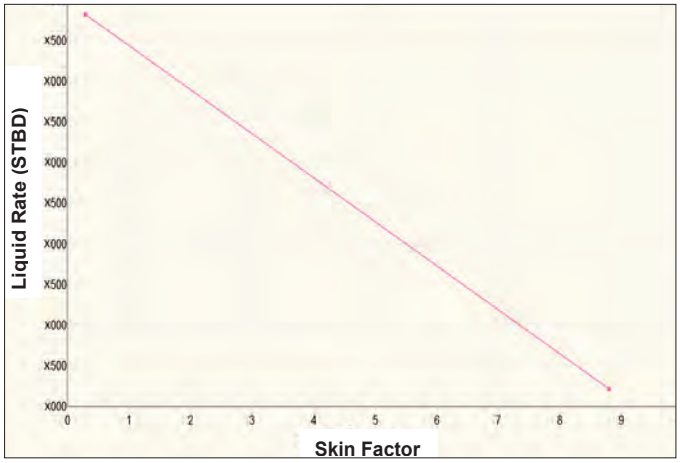

Fig. 10. Reduction in the skin factor experienced by Well-A after treatment.

Figure 9 also presents the information needed to understand the actual gain in injectivity on Well-A — after the stimulation treatment — by comparing the injection figures before the treatment (second channel from the left) vs. after the treatment (fourth channel from the left). This exercise confirmed an increase in 175% on the injection flowing rate at a similar IFWHP, which equates to a reduction in the skin factor from 8.8 to 0.3, Fig. 10.

RESULTS

The CT real-time downhole measurement flow tool proved, for the first time worldwide, its correlation with the injection logging tool measurements. This comparison shows that it is possible to optimize the placement of the stimulation fluids and provides the option to place the CT accurately in front of the target intervals using the information collected prior an acid stimulation treatment. Significant savings can be made in operational cost and logistics by eliminating the need to conduct conventional production logging and step-rate test operations to determine well performance and injection profiles prior to the execution of the main treatment of an acid stimulation in a SWD well. This is because the CT real-time downhole measurement flow tool provides similar information that can be collected using the same equipment and setup already available at the location to conduct the main treatment of the acid stimulation operation.

It was noticed during the evaluation of the information collected by the CT real-time downhole measurement flow tool that the absolute injection rate figures are underestimated. This situation is understood as a consequence of the reduction in the cross-sectional injection flowing area caused by the CT inside the wellbore, since the injection is conducted in the annulus CT/tubing.

Thanks to the proper planning and evaluation of the available information from the candidate well, the skin factor initially estimated at 8.8 was successfully reduced to 0.3, and the overall injectivity was increased by 175% by following the recommended customized procedure defined for this particular SWD well by the production engineering team.

One of the three main objectives of the proposed acid stimulation was not accomplished. This is to get the noncontributing (noninjection) zones to a contribution/injection status, resulting in a homogeneous profile. This situation is a clear indication that only a portion of the target interval was subject to stimulation, despite the homogeneity shown by formation evaluation logs in terms of permeability and porosity. This interesting finding is highly relevant to better estimate the potential gain to be obtained after a similar operation for future acid stimulations in SWD wells. Therefore, it is recommended for the similar interventions, in case there is a dominant injection zone, to divert such zone with more diverter volumes, or a fiber-laden diverter to divert away from it — ensuring the stimulation of the rest of the intervals in case a post-stimulation injection profile is not homogeneous and followed by injection profile evaluation.

CONCLUSIONS

The following conclusions can be drawn from the world's first intervention of this type to correlate the injection logging data, and while performing the matrix stimulation treatment in the single run:

- The information offered by the CT real-time downhole measurement tool can be used as a substitute of the conventional production logging and step-rate test operations to determine the well performance and the injection profile in SWD wells. This situation provides a tremendous opportunity for substantial savings in operational costs and logistics.
- Given the reduction in the cross section injection flowing area caused by the CT inside the wellbore, the absolute injection rate figures from the CT real-time downhole measurement tool are underestimated. This limitation can be easily addressed by the execution of nodal analysis to estimate injection flowing rates, taking into consideration the mentioned reduction in the cross-sectional area.
- The CT real-time downhole measurement tool can be used to perform a post-stimulation injection profile in SWD wells, so that the effectiveness of an acid stimulation treatment can be assessed.
- A conservative approach should be adopted while making the estimation of the expected gain to be obtained in SWD wells when conducting similar operations. This is mainly related to the fact that not necessarily the entire target interval will be effectively stimulated, even after careful placement of diverters in thief zones, despite the homogeneity in petrophysical properties along the target zone.
- To effectively divert from high intake zones, higher

volumes of diverter or fiber laden diverters must be considered.

ACKNOWLEDGMENTS

The authors would like to thank the management of Saudi Aramco for their support and permission to publish this article. The authors would also like to thank Saad M. Mutairi, for his contributions to compiling the final version of this article. Special recognition is given to Ahmed A. Khalaf, Saudi Aramco, and Kaisar Al Hamwi, Mohammad Arifin, and Adzlan Ayob, Schlumberger, for their decisive collaboration during the planning and execution of the operations described in this article.

This article was presented at the Abu Dhabi International Petroleum Exhibition and Conference, Abu Dhabi, UAE, November 13-16, 2017.

REFERENCES

1. Al-Houti, N., Al-Matrouk, Y., Al-Othman, M.R., Al-Mehanna, H.S., et al.: "Cost-Effective Approach in Stimulating Open Hole Water Injectors Using Real-Time Flow Measurement: A Case Study," SPE paper 184760, presented at the SPE/ICoTA Coiled Tubing and Well Intervention Conference and Exhibition, Houston, Texas, March 21-22, 2017.
2. Buhassan, S.A., Halder, S., Tammar, H., Beheiri, F., et al.: "Case History: New Horizons for Downhole Flow Measurements via Coiled Tubing Equipped with Real-Time Downhole Sensors at South Ghawar Field, Saudi Arabia," SPE paper 172570, presented at the SPE Middle East Oil and Gas Show and Conference, Manama, Bahrain, March 8-11, 2015.

BIOGRAPHIES

Ramiro Cedeño is a Senior Production Engineer working for Saudi Aramco's Southern Area Production Engineering Department. He joined Saudi Aramco in 2014 and has over 15 years of experience working for exploration and production companies in South America, the North Sea, and the Middle East.

Ramiro received his B.S. degree in Petroleum Engineering from Universidad Surcolombiana, Neiva, Huila, Colombia. He also received an MBA in Oil and Gas Management with Merit from the Aberdeen Business School, Robert Gordon University, Aberdeen, U.K.

Ramiro is trilingual with fluency over Spanish, Portuguese and English. He is an active member of the Saudi Council of Engineers (SCE), the Society of Petroleum Engineers (SPE), and the Colombian Professional Petroleum Engineering Council (CPIP).

Ibrahim K. Al-Thwaiqib is a Production Engineer working in Saudi Aramco's Southern Area Production Engineering Department. He has 11 years of experience in oil and gas industry. Ibrahim has worked as Production Engineer, Intelligent Field Engineer, Operation Foreman, and Production Engineering Supervisor.

Ibrahim received his B.S. degree in Petroleum Engineering from King Fahd University of Petroleum and Minerals (KFUPM), Dhahran, Saudi Arabia.

Danish Ahmed has been working at Saudi Schlumberger since 2007. He is a Senior Intervention Optimization Engineer with Schlumberger Well Services – Coiled Tubing Services, supporting the ACTive Services Platform. Danish's experience includes working as a Field Engineer with Well Production Services (Fracturing and Pumping Services) based in 'Udhailiyah, Saudi Arabia, supporting proppant/acid fracturing and matrix acidizing jobs, followed by working as a Production Technologist with Petro Technical Services (formerly called Data and Consulting Services) in Dhahran, Saudi Arabia.

In 2007, he received his M.S. degree in Petroleum Engineering from Heriot-Watt University, Institute of Petroleum Engineering, Edinburgh, Scotland.

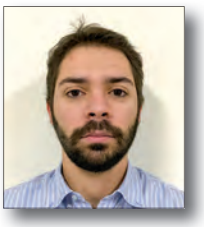

Rodrigo Sa works for Schlumberger Saudi Arabia Well Services – Coiled Tubing Segment. Since 2014, he has been assigned to Saudi Aramco's Gas and Production Engineering Division in 'Udhailiyah as the Coiled Tubing (CT) Technical and Sales Engineer. Rodrigo has worked as a CT Senior Field Engineer in Brazil, and in Saudi Arabia, from 2009 to 2014. His work experience involves designing, executing, and evaluating the CT interventions for offshore ultra-deepwater, high-pressure, high temperature wells, and unconventional resources. Rodrigo was the Project Leader from Schlumberger for developing and successfully implementing CT live descaling interventions for the first time in Saudi Arabia.

In 2009, he received his B.S. degree in Mechanical Engineering from Federal University of Rio Grande do Norte, Natal, Brazil.

The Interpretation of Miscible Fluid Displacements in Multimodal Carbonates

Dr. Ahmad M. Al-Harbi, Jun Gao and Dr. Hyung T. Kwak

ABSTRACT

The transport of fluids through a permeable rock can follow complex paths, depending on the details and complexity of the pore network attributes. Understanding the contribution of pore systems and pore system elements — such as pore bodies and pore throats — to the total flow is important for building and understanding the proper representative relative permeability models for use in reservoir simulation of secondary and tertiary recovery. Carbonate reservoirs containing reservoir facies with instances from both the macropore and micropore pore system families must be assessed for the effect of the pore systems on the relative permeability curves and the ultimate recovery of hydrocarbons from the two-phase flow. These same factors will also affect the extent of the mixing zone during miscible fluid displacement enhanced oil recovery processes.

We study these pore systems using a single-phase dispersion test, mimicking the miscible displacement, and continuously monitor the flood with nuclear magnetic resonance (NMR) T_2 distribution measurements. Fluid displacements relative to pore type are directly observed and quantified. The single-phase dispersion test data is modeled using the convective-dispersive model.

Our results demonstrate that the micropores of our studied bimodal carbonate samples are preferentially connected and that the Type 1 micropores in the M_1 bimodal petrophysical rock type (PRT) effectively contribute to the displacement/flow mechanism in these rocks. Our experimental results from the single-phase dispersion study suggests that the contribution of micropores to the bulk displacement in the M_1 PRT must be included when modeling the relative permeability.

We analyze the experimental results from the miscible fluid displacement experiments using the convective-dispersive model. The analysis results infer that the macropores, M, and the Type 1 micropores communicate in parallel and as a series for the M_1 PRTs. These results demonstrate the importance of including this flow behavior in the design of any types of miscible and surfactant flooding for reservoirs with these PRTs as they are relevant to the extent of the mixing zone relative to pore types. Further investigation of the current claim, including more samples from different lithofacies of the M_1 PRT, is under development.

INTRODUCTION

Major efforts and studies have presented the geological, petrophysical, and statistical data defining the presence, types, and statistics of the multimodal porosity in a major carbonate reservoir[1-7] of Saudi Arabia. Cantrell and Hagerty (1999)[2] defined the presence of multiple types of microporosity using petrographic methods and mercury injection capillary pressure (MICP) data. Clerke et al. (2008)[1] constructed a large, statistically robust database containing geological attributes, petrophysical attributes, and dynamic attributes for these important limestone reservoir pore systems. The latter statistically classified the pore systems in this reservoir as consisting of at least four modes (porositions) after classifying on the maximum pore throat diameter attribute extracted using Thomeer analysis from a large set of MICP data. The modes are termed as M, 1, 2, and 3 porositions[1]. The M_1, which stands for the Type M macroporosition and Type 1 microporosition combination, is found to be the most abundant PRT in the Arab-D reservoir. The M instance comes from the macroporosity mode with a wide range of pore throat diameters, a mean maximum diameter of ~58 µm and average porosity of 17%. The Type 1, on the other hand, comes from a mode of smaller maximum pore throat diameters with a mean maximum diameter in the neighborhood of 1.1 µm and an estimated average porosity of 5.6%[1].

Petrographic studies by Cantrell and Hagerty (1999)[2] showed that both pore subsystems in the grainstones and mud-lean packestones with micritized grains (M_1) are well connected. Interestingly, the Type 1 micropores carry a considerable amount of the original oil in place in the M_1 PRT, ~25%[8]. Clerke (2009)[6] and Clerke et al. (2013)[8] initiated a comprehensive investigation of the flow properties for the M_1 PRT and demonstrated the contribution of the Type 1 microporosity of the M_1 samples to the total oil recovery by waterflood. Fung et al. (2011)[9] performed numerical studies to evaluate the effect of the imbibition capillary pressure (P_C) and the transfer coefficient between micropores and macropores on the oil recovery forecast of the waterflood of the reservoir containing the M_1 PRT, assuming a spontaneous imbibition process for the mixed wet bimodal reservoir. They concluded that oil recovery is sensitive to both the imbibition P_C and the

transfer coefficient. These previous studies highlight the importance of the interaction between different pore types on oil recovery from an important bimodal carbonate reservoir.

Reservoir pore systems and their geometrical attributes determine the boundary conditions for fluid flow within the sample pore space. The geometrical properties of these boundary conditions are identical in either single-phase or multiphase flow. Al Harbi (2009)[10] and Funk and Al Harbi (2009)[11] developed an innovative single-phase fluid — no capillarity — experiment to investigate the geometrical controls of the pore systems' geometry for the M_1 PRT. In that work, single-phase fluid transport behavior was investigated during the displacement of water (H_2O) by heavy water (D_2O) in the bimodal M_1 PRT samples.

Even though they have different nuclei, H_2O and D_2O are chemically identical, and deuterium (D) is invisible to the H^1 nuclear magnetic resonance (NMR) measurement. Therefore, the injection of D_2O into the H_2O filled bimodal pore space with the continuous monitoring by H^1 NMR will determine the steadily increasing presence of D_2O by the steadily decreasing presence of the H_2O in the pore subsystems as the displacement proceeds. The outcome is the accurate quantification of single-phase fluid volumetric displacement in each pore type. The replacement process of H_2O by D_2O in the pore space is dispersive redistribution, with the flow velocity and the concentration gradients supported by the details of the M_1 bimodal pore geometry.

In this new work, a series of these D_2O displacing H_2O laboratory studies are conducted on carbonate samples with known petrophysical rock types (PRTs) M, M_1 and Type 1 PRTs[1] to evaluate the bulk displacement efficiency of the various pore types and their combinations under single-phase miscible flow. The volumetric displacement efficiencies for each pore system can be determined from the described experimental data. The results reported here provide important insights into the dynamic processes strictly controlled by the pore geometry during a simple miscible displacement. The single-phase miscible displacement results then serve as a template for the proper modeling of the pore geometrical effects that are still present in the two phase displacements and the proper formulation of the relative permeability.

EXPERIMENTAL

Material

Brines. H_2O and D_2O brines (5% wt NaCl) were used in this study. Density of the H_2O and D_2O brines at room temperature were 1.0313 g/cm^3 and 1.1375 g/cm^3, respectively. The viscosity of the H_2O and D_2O brines at room temperature were 1.27 centipoise (cP) and 1.03 cP, respectively.

Core Samples. Six 1" diameter carbonate samples were prepared for the current study. All of the 1" core plugs were cut in half creating 12 plugs, with one used in the MICP study while the other was used in the single-phase miscible fluid displacement study. The results of the MICP data were used to assign the PRTs using the published criteria[1]. The samples were grouped into three PRTs: M, M_1, and Type 1. Detailed core sample properties are presented in Table 1.

Our NMR T_2 experiments at 100% H_2O brine saturation are straightforward, without hydrocarbon effects. Figure 1 shows the NMR T_2 distributions for the six samples. Figure 2 shows the pore throat diameter distributions from the MICP of the six twin samples.

NMR Monitored Displacements

The NMR experimental configuration is shown in Fig. 3. The system is composed of an NMR system, a high-pressure, high temperature (HPHT) coreflooding NMR probe (P5 probe from Oxford), a Quizix pump, piston accumulator, backpressure regulator (BPR), and a confining pressure and heating circulating system. The NMR system used is 12 MHz Oxford Geospec2 with 3D gradients tuned to hydrogen. The operating temperature was 35 °C. The NMR instrument was set for automated sequential measurements using a Carr-Purcell-Meiboom-Gill (CPMG) sequence, Fig. 4.

Sample No.	PRT	Length (cm)	Conventional Data		MICP Data			
					Macropores		Micropores	
			Porosity (%)	Klinkenberg Permeability (mD)	Entry Pressure Pd1 (psi)	Bulk Volume BV1 (%)	Entry Pressure Pd2 (psi)	Bulk Volume BV2 (%)
28	M	2.22	20.05	612.05	4	20.1		
107	M	2.12	19.89	1,038.42	2	18.8		
40	M_1	2.06	25.36	402.65	5.4	22	180	5.6
67	M_1	2.1	18.65	70.34	5.8	14.6	174	6.2
104	Type 1	2.12	19.23	0.71	165	19.2		
105	Type 1	2.43	20.71	0.88	200	19.8		

Table 1. Detailed core sample properties from the conventional and MICP data

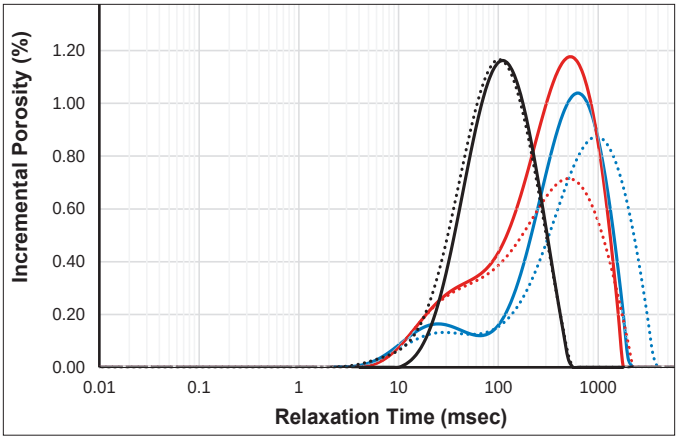

Fig. 1. The NMR T_2 distributions of the fully water saturated samples: S28 M PRT (solid blue line), S107 M PRT (dash blue line), S40 M_1 PRT (solid red line), S67 M_1 PRT (dash red line), S104 Type 1 PRT (solid black line), and S105 Type 1 PRT (dash black line).

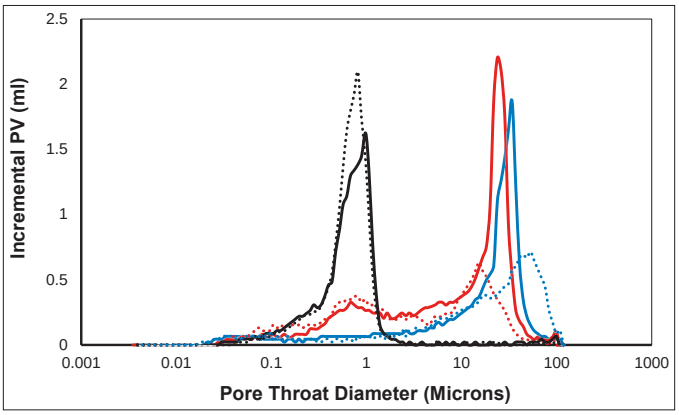

Fig. 2. Pore throat diameter distributions from the MICP: S28 M PRT (solid blue line), S107 M PRT (dash blue line), S40 M_1 PRT (solid red line), S67 M_1 PRT (dash red line), S104 Type 1 PRT (solid black line), and S105 Type 1 PRT (dash black line).

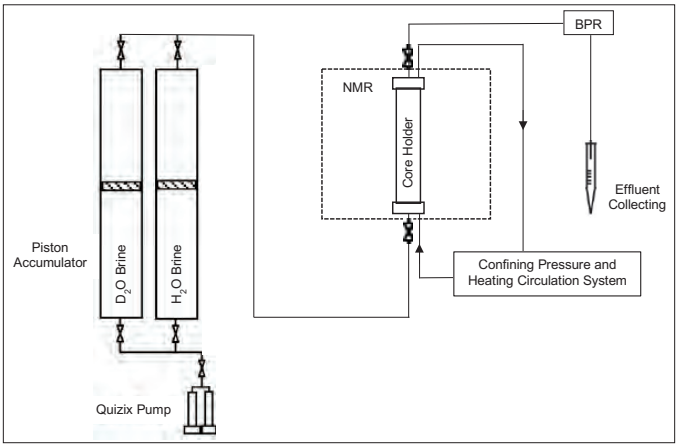

Fig. 3. Schematic diagram of the NMR H^1 T_2 monitored single-phase test of the D_2O displacing the H_2O.

In our experiments, the P5 probe is vertically mounted in the NMR magnet. Before each sample displacement test, the P5 probe is calibrated using a standard calibration liquid sample with known volume to ensure the optimum sensitivity. The percentage error in our T_2 measurements is less than 1%. The sample is confined using an NMR invisible circulated fluorinated fluid at 1,000 psi and maintained at a constant temperature. Brines are loaded into each individual piston accumulator, degassed using a vacuum pump, and injected into the core sample by a computer controlled Quizix pump. The minimum injection rate used was 0.0227 cm³/min, so that dispersion dominates the flow[13]. We monitor the H^1 NMR T_2 during the injections. The dispersion dominated signal continues to develop during the injection but after 2 pore volumes (PVs) to 3 PVs of injection, the succeeding signal changes are no longer indicative of the dispersion. The H^1 NMR T_2 measurements are acquired using a constant number of scans of four, for each T_2 measurement. One T_2 measurement takes about 100 seconds. The SNR for one T_2 measurement is monitored continuously and the scan count is increased to eight when the SNR drops below 100, to account for the SNR decrease. The time series of results is then normalized to $\sqrt{NS}$ to enable quantitative comparisons.

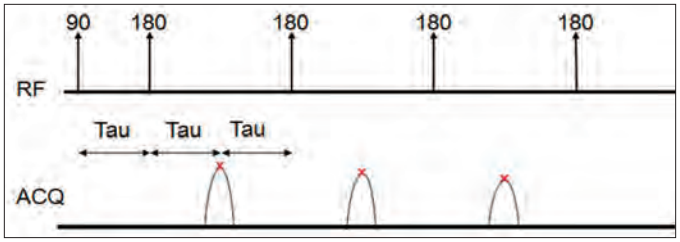

Fig. 4. The CPMG sequence used to obtain the T_2 measurements.

The test procedure of the displacement testing was as follows:

1. Saturate the core plugs with synthetic connate brine under vacuum, and then apply a pressure of 2,000 psi to assure the plugs are fully saturated.
2. Mount the core plug in a Teflon heat shrink tube in the P5 probe and apply a confining pressure of 1,000 psi. Flush 5 PV of H_2O brine with a backpressure of 400 psi to assure no gas was trapped during loading of the sample.
3. Purge the inlet line prior to each D_2O displacement. Bypass the BPR.
4. Conduct H^1 NMR T_2 measurements. NMR acquisition parameters are shown in Table 2.
5. Set the D_2O brine pump flow rate at a constant rate of 0.0227 cm³/min.
6. Start the D_2O brine injection and NMR T_2 measurement simultaneously.
7. Stop the D_2O brine injection after the injection of 2 PVs.
8. Switch to H_2O brine and flush it for at least 10 PVs using a backpressure of 400 psi.
9. Repeat steps 3 to 6 for H_2O brine using an injection rate of 0.227 cm³/min.

NMR Measurement Parameter	T_2 by CPMG Sequence	T_2 Map by Spin-Echo Single Point Imaging (SE-SPI) Sequence
Recycling Delay (RD), s	15	15
Echo Delay (Tau), µs	120	120
Total Number of Echo Trains (NECH)	41,667	53,761
Number of Scans (NS)	8	8
Field of View (cm)		4
Number of Steps		32
Maximum Gradient Strength (gauss/cm)		25.2

Table 2. NMR measurement parameters

EXPERIMENTAL RESULTS AND DISCUSSIONS

Pore Type from NMR T_2 Distribution

The NMR T_2 distributions and NMR T_2 spatial measurements at 100% H_2O brine saturation of the six samples are shown in Fig. 1. Figure 1 also shows that samples of M and M_1 PRTs (blue and red) contain two pore types (M for macropore and 1 for micropore) and two distribution components within the H^1 NMR T_2 distributions. The macropores give a high amplitude distribution component centered at about 500 ms to 600 ms relaxation time. A smaller amplitude contribution is evident and not completely resolved with a pronounced shoulder at about 30 ms to 50 ms, relaxation time. The MICP data of the samples of the M PRT (blue lines in Fig. 2) clearly show that these samples contains one family of large pore throats with a long trailing end. Based on the Thomeer analysis method, this trailing end infers that there are a steadily declining portion of pore throat diameters and volumes associated with the pore system and these are likely corners and crevices associated with the larger pore network and less connected[1]. Therefore, the pore type in the samples of the M PRT with H^1 NMR T_2 distributions centered at about 20 ms to 30 ms — for samples (S) S28 and S107 — are related to the corners and crevices within the M pore network. In our work, we refer to these pores as dead-end pores.

The monomodal Type 1 PRT (black line in Fig. 1) gives a single symmetric distribution centered relaxation time at about 100 ms. In Fig. 5, the NMR H^1 T_2 spatial record shows uniform pore-size distributions along the length of the core plug. Table 3 presents the porosities derived by fitting the H^1 NMR T_2 distributions to two Gaussian models corresponding to the macropore and dead-end porosity of the M PRT samples and to the macroporosity and microporosity of the M_1 PRT samples. The two Gaussian distributions used to fit the H^1 NMR T_2 distributions are shown in Fig. 6 for the M and M_1 PRTs samples. The macroporosity peak is centered about 500 ms to 600 ms, the Type 1 peak is centered about

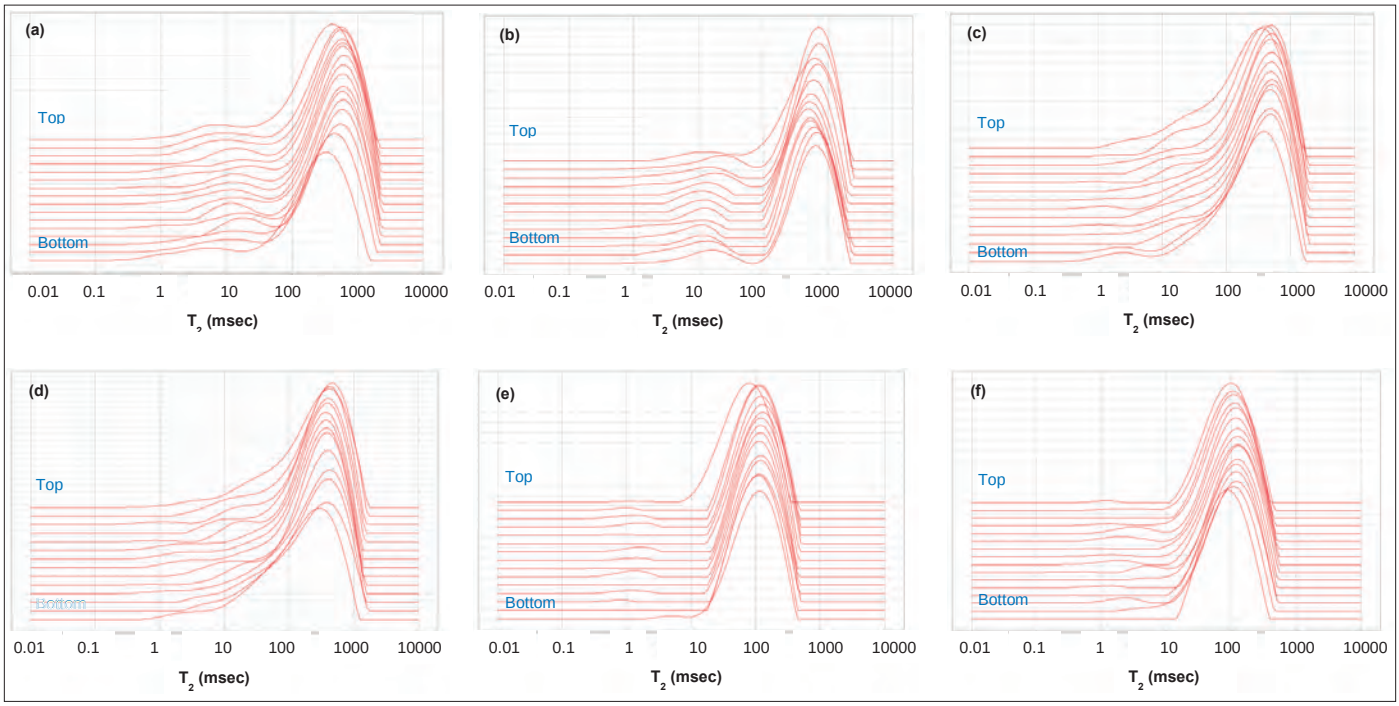

Fig. 5. NMR H^1 T_2 spatial measurements of S28 (a), S107 (b), S40 (c), S67 (d), S104 (e), and S105 (f).

Sample No.	Gaussian Fit		
	Macroporosity (%)	Microporosity (%)	Bulk Porosity (%)
28	15.79	4.56	19.78
107	14.33	5.48	19.34
40	15.26	11.02	25.74
67	9.78	9.88	19.26
104			19.95
105			21.7

Table 3. NMR porosity data derived by fitting the H¹ NMR T_2 distributions to two Gaussian models

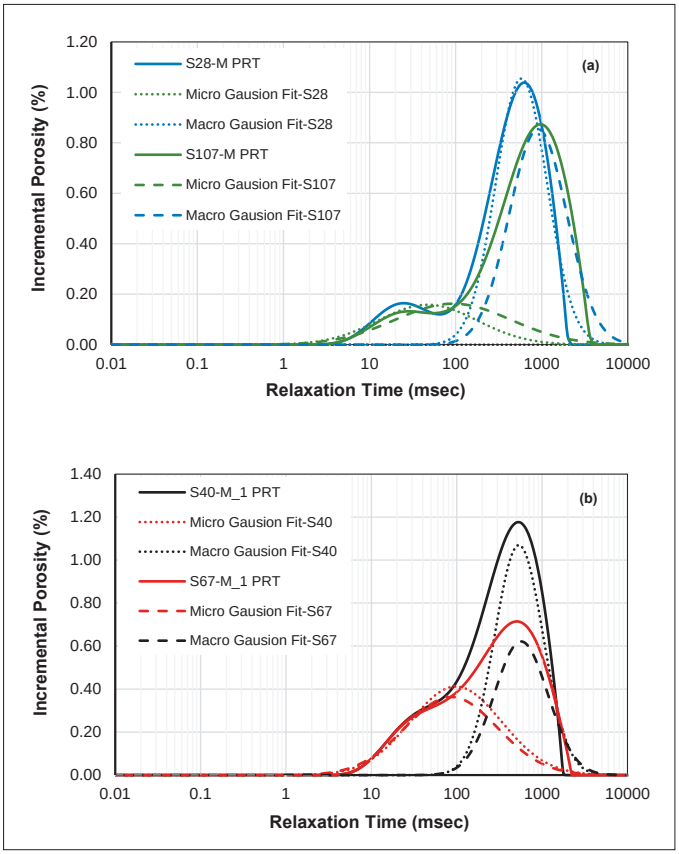

Fig. 6. The H¹ NMR T_2 distributions and Gaussian fits for S28 and S107 (a), and S40 and S67 (b).

100 ms, and the dead-end porosity peak is centered about 40 ms to 80 ms.

T_2 NMR Analysis

NMR H¹ NMR T_2 analysis and modeling were carried out for these samples using the same process that was described in our previous work[11]. The displacement data for use in the model is provided by the normalized H¹ NMR T_2 PV for each pore system as the D_2O injection volume steadily increases in time. The time sorted normalized H¹ NMR T_2 PVs from that study is reproduced here in Fig. 7 — the longer T_2 times are plotted to the left for clarity. Figure 7 from Funk and Al Harbi (2009)[11] clearly shows that the rate of H¹ NMR T_2 PV change is different for the macro (left side time series of H¹ NMR T_2 peaks) and the micro (right side time series of H¹ NMR T_2 peaks).

In the previous study, an integrated error function was used to model the miscible dispersion displacement efficiency data using the convective-dispersive model[11].

In the case of displacements in porous media, transport phenomena are determined by the relative importance of multiple hydrodynamic mechanisms[14]. Deans (1963)[14] describes these as:

1. Molecular diffusion in the flow direction.
2. Turbulent (cell mixing).
3. Lateral transport processes coupled with velocity and/or residence time distributions.
4. Finite mass transfer rate between a porous matrix and the flowing phase.

Deans (1963)[14] adequately described these mechanisms in the following classical dispersion model:

$$\frac{1}{N_{PE}}\frac{\delta^2 C_D}{\delta^2 x_D} + \frac{\delta C_D}{\delta x_D} = \frac{\delta C_D}{\delta t_D} \quad (1)$$

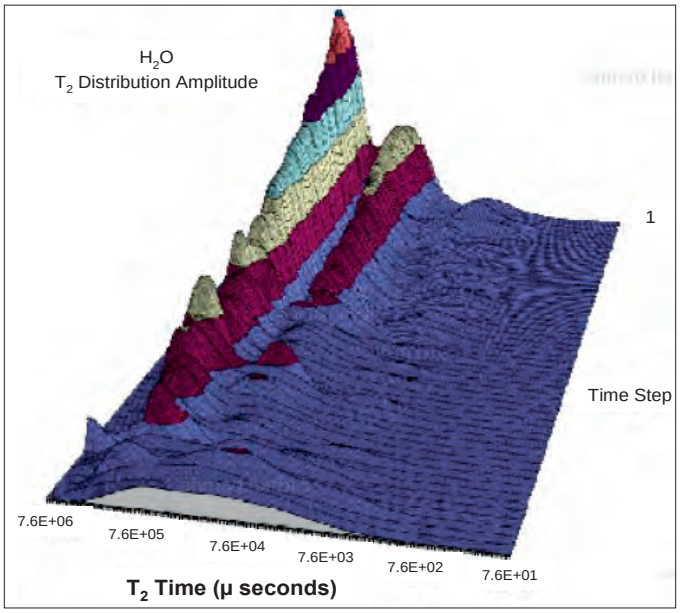

Fig. 7. Displacement time displayed T_2 distributions for the M_1 sample[11].

which can be solved for the boundary conditions:

$$\begin{aligned} C_D(x_D,0) &= 0 && for\ x_D \geq 0 \\ C_D(x_D \to \infty, t_D) &= 0 && for\ t_D \geq 0 \\ C_D(x_D \to -\infty, t_D) &= 1 && for\ t_D \geq 0 \end{aligned} \quad (2)$$

To yield a simplified solution the complementary error function solution for the concentration as a function of displacement distance:

$$C_D = \frac{1}{2} erfc\left[\frac{x_D - t_D}{2\sqrt{\frac{t_D}{N_{PE}}}}\right] \quad (3)$$

This expression works well for effluent concentrations, however, it cannot be applied directly when averaging volumetric data is used. In this case an integral form of the error function solution can be applied[13]. This takes the form of:

$$\bar{C}_D = \int_0^1 C_D(x_D, t_D)dx = \sqrt{\frac{t_D}{N_{PE}}} \cdot \left[ierfc\left(\frac{-\sqrt{t_D N_{PE}}}{2}\right) - ierfc\left(\frac{1-t_D}{2\sqrt{\frac{t_D}{N_{PE}}}}\right)\right] \quad (4)$$

where the dimensionless variables are:

$$C_D = 1 - \frac{C_{H_2O}}{C_{H_2O_{initial}}}, \text{ Dimensionless deuterium concentration}$$

$$t_D = \int_0^t \frac{q_i}{V_{P_i}} dt, \text{ Dimensionless time}$$

$$x_D = \frac{x}{L}, \text{ Dimensionless distance}$$

$$N_{PE} = \frac{uL}{\emptyset K_L}, \text{ Peclet Number}$$

where $ierfc$ is the integral of the complementary error function defined by:

$$ierfc(x) = \int_x^\infty erfc(s)ds = \frac{1}{\sqrt{\pi}}\exp(-x^2) - x\, erfc(x) \quad (5)$$

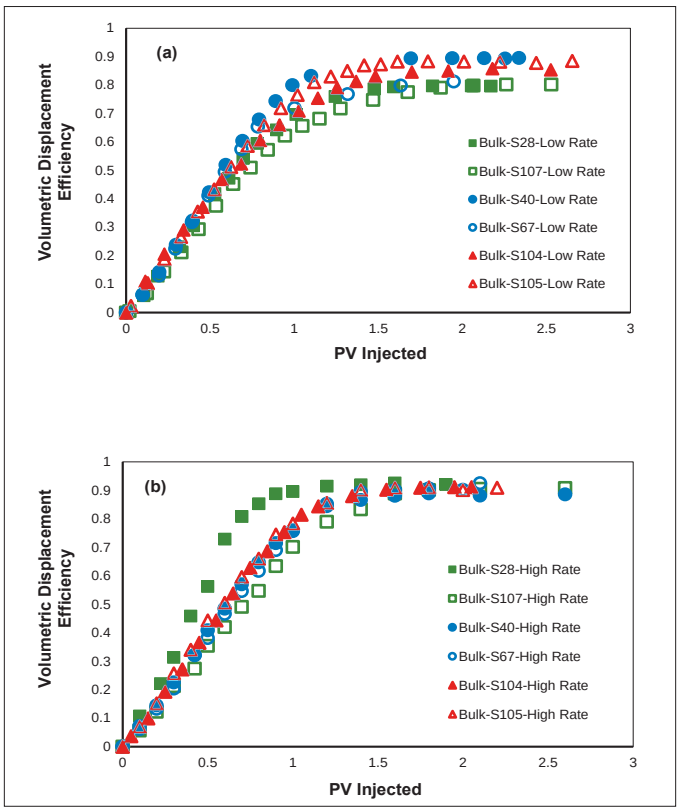

Fig. 8. Injected PV domain bulk data for the low displacement rate (a), and the high displacement rate (b). Volumetric displacement efficiency almost reached a plateau after the injection of about 2 PVs of D_2O brine, except for S67.

Sample No.	Injection Rate	Macropartition				Micropartition/Dead-End Partition				Bulk		
		Vol. Fraction	u (cm²/sec)	N_{PE}	Kl (cm²/sec)	Vol. Fraction	u (cm²/sec)	N_{PE}	Kl (cm²/sec)	u (cm²/sec)	N_{PE}	Kl (cm²/sec)
28	Low	0.776	2.81×10^{-5}	33.07	9.73×10^{-6}	0.224	5.60×10^{-6}	26.1	1.10×10^{-5}	2.78×10^{-5}	28.9	1.10×10^{-5}
	High		2.84×10^{-4}	68.2	6.15×10^{-5}		7.39×10^{-5}	77.4	4.87×10^{-5}	3.60×10^{-4}	69.4	5.94×10^{-5}
107	Low	0.723	1.73×10^{-5}	19.2	1.32×10^{-5}	0.277	5.70×10^{-6}	19.2	8.79×10^{-6}	2.37×10^{-5}	18.6	1.35×10^{-5}
	High		1.56×10^{-4}	36.0	6.33×10^{-5}		5.12×10^{-5}	64.7	3.03×10^{-5}	2.12×10^{-4}	38.6	5.82×10^{-5}
40	Low	0.581	1.58×10^{-5}	74.1	2.83×10^{-6}	0.419	1.14×10^{-5}	42	4.98×10^{-6}	2.75×10^{-5}	51.6	4.10×10^{-6}
	High		1.51×10^{-4}	52.83	3.78×10^{-5}		1.12×10^{-4}	27.6	7.48×10^{-5}	2.61×10^{-4}	47.4	4.23×10^{-5}
67	Low	0.498	1.46×10^{-5}	25.6	1.21×10^{-5}	0.502	1.47×10^{-5}	27.3	1.13×10^{-5}	2.94×10^{-5}	26.7	1.16×10^{-5}
	High		1.16×10^{-4}	67.4	3.64×10^{-5}		1.33×10^{-4}	21	1.33×10^{-4}	2.39×10^{-4}	48.3	5.22×10^{-5}
104	Low									2.85×10^{-5}	21.6	1.34×10^{-5}
	High									2.87×10^{-4}	46.0	6.32×10^{-5}
105	Low									2.71×10^{-5}	26.4	1.11×10^{-5}
	High									2.67×10^{-4}	35.4	8.15×10^{-5}

Table 4. NMR T_2 partitioned convective-dispersive fitting results (u, N_{PE} and Kl) for the low and high injection rates. Model results for dead-end pores (shaded) are assumed to be not realistic

with the properties that:

$$ierfc(0) = \frac{1}{\sqrt{\pi}} and\ \frac{1}{\sqrt{\pi}}(-x) = 2x + ierfc(x) \quad (6)$$

In our work, we used Eqn. 4 to model the displacement efficiency data. This function carries two unknowns, which are dispersion coefficient and fluid velocity (u). Thanks to the successful experimental measurement of the flow rate relative to pore type, the model could be fitted to the displacement efficiency data by varying only the dispersion coefficient. Subsequently, measuring the flow rates usually require several data points before breakthrough time, which was difficult to obtain in the current study due to the higher fluid injection rate than the rates used from the previous study.

Here, the volumetric displacement efficiency data, E_D (t), is defined as:

$$E_{D,i}(t) = 1 - \frac{Volume\ of\ water\ in\ pore\ subsystem,\ \ i,\ \ at\ displacement\ time,\ \ t}{Total\ volume\ of\ displaced\ water\ in\ pore\ subsystem,\ \ i,\ \ after\ displacement} \quad (7)$$

Figure 8 shows that the E_D of the bulk samples, obtained from the NMR T_2 measurements, which almost reached a plateau after the injection of about 2 PVs of D_2O brine, except for S67. But the data does show that there are still some pores that are not yet accessed by D_2O brine. We assume that these pores are less connected to the flowing pores in the samples, and that their displacement is only through a slow mass transfer process with the flowing pores. Since the main objective of the current work is to assess the pore geometry effect of the flowing pores on dispersion results, we considered that the displacement in

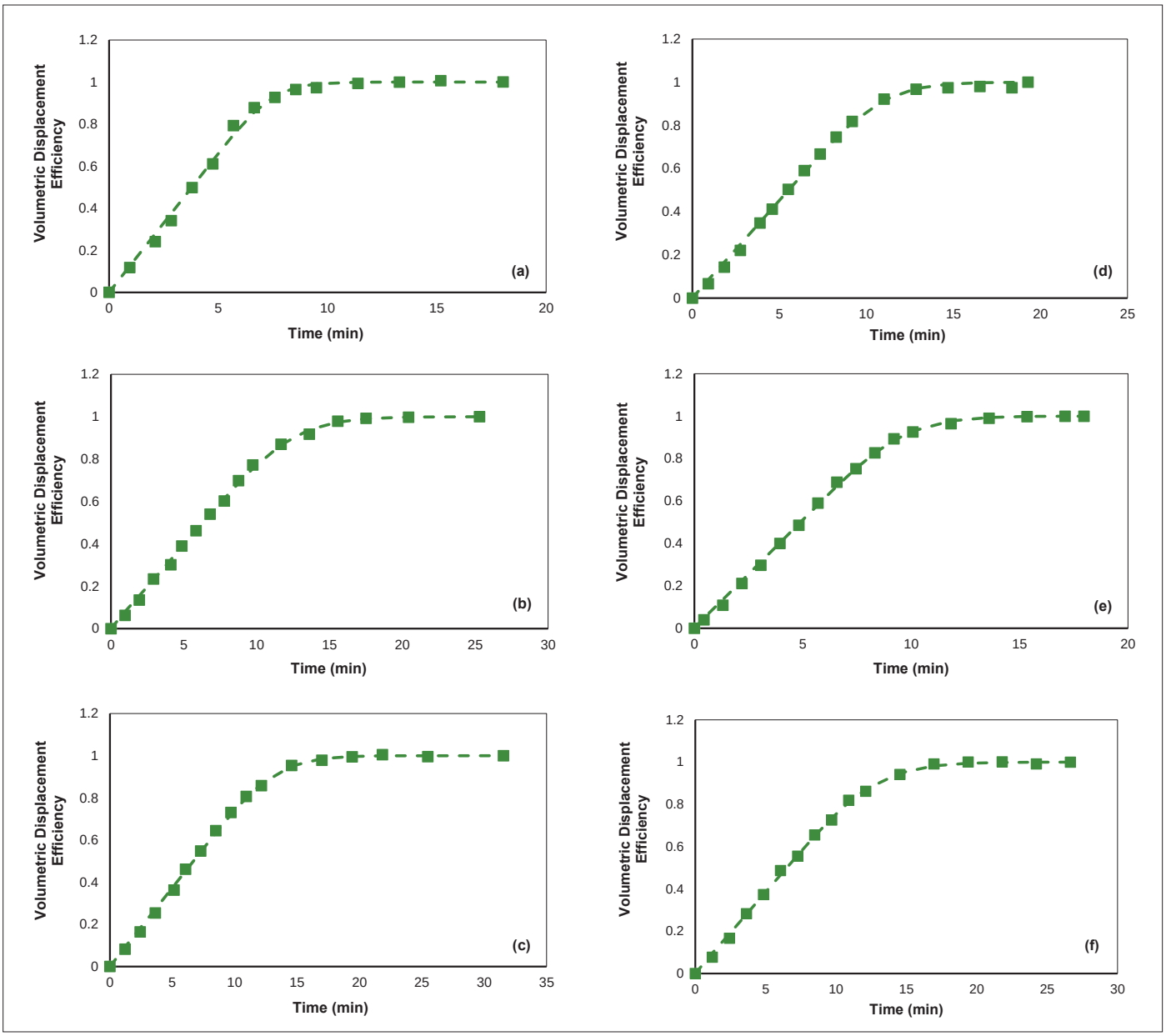

Fig. 9. Time domain of the volumetric displacement efficiency bulk data (marker), from the high injection rate, and convective-dispersive model fit (line) for S28 (a), S107 (b), S40 (c), S67 (d), S104 (e), and S105 (f).

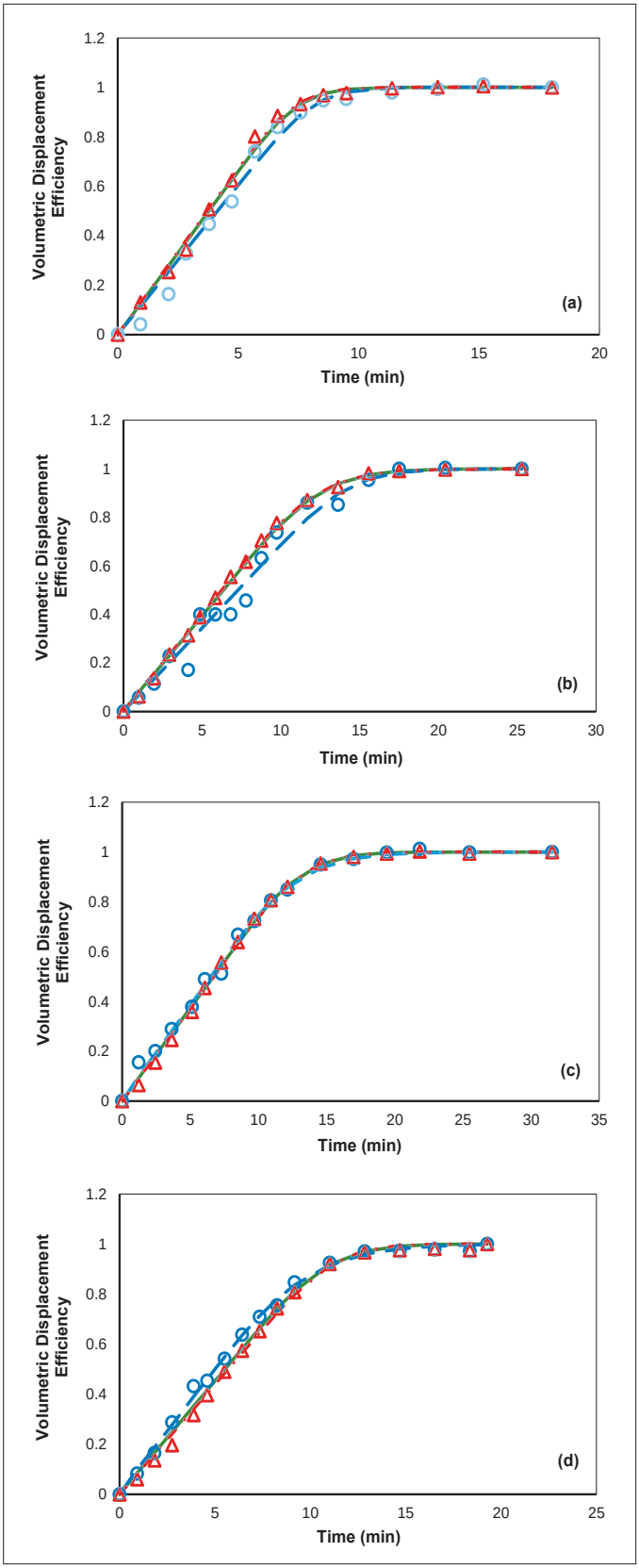

Fig. 10. Time domain of the volumetric displacement efficiency data, from the high injection rate, and convective-dispersive model fits for both the macropores and dead-end pores in the M PRT samples, S28 (a) and S107 (b), and the macropores and micropores in the M_1 PRT samples, S40 (c), and S67 (d). Markers represent time domain of the volumetric displacement efficiency data (blue for micropartition, and red for macropartition) and lines represent convective-dispersive model fits (blue for micropartition, and red for macropartition, and green for the bulk sample).

our cores already reached equilibrium (plateau region in Fig. 8) after the injection of about 2 PV to 2.5 PVs.

Therefore, we normalized our displacement data to the total PV displaced by D_2O at the conclusion of the displacement tests. The volumetric displacement efficiency data of each pore system at each time step was modeled using Eqn. 4 for the convective-dispersive model and the integrated difference between the data and the model — integrated error — was obtained. The model was iteratively adjusted using just two fluid parameters; u and the fluid dispersion parameter, until the integrated error was reduced to a minimum. The results of this model to data reconciliation are presented in Table 4. Also, in this work, the macropore and micropore/dead-end PVs used in the volumetric displacement efficiency calculation were obtained by successive Gaussian analysis of the H^1 NMR T_2 PVs rather than by using a single T_2 cutoff value — defined as the NMR T_2 value dividing the NMR T_2 distribution into micropores/dead-end pores and macropores — as was done previously.

Fitting of the volumetric displacement efficiency data for all samples — at the high injection rate — are shown in Figs. 9 and 10. The results of fitting these data to the model, Eqn. 4, are also shown in Table 4. The dispersion parameter values for the macropartition and the micropartition (Kl) are well within the range of other tests on carbonates reported in the literature[11, 16, 18-20].

Figure 9 shows that the bulk data of all studied samples was nicely fitted by the classical convective-dispersive model, Eqn. 4. Consequently, there are clear disagreements between the model fit and the bulk data in the regions of the early linear trend, the mid-time rollover, and the late time plateau. In the early linear trend region, all figures show that the model fit always displays a shift to the left. This could be attributed to two reasons; the presence of dead-end pores that barely contribute to the fluid flow (and even to diffusion[21]), and/or the presence of traces of H_2O brine in the grooves of the bottom end-piece (inlet side of the core sample) of the NMR probe. Both of these reasons may cause experimental data in this region to shift to the right. It is assumed that the dead-end pores in these samples are caused by different pore geometries — different pores' corners and crevices — as these samples are from different rock textures. Although, these dead-end pores are expected to be of negligible volumes in the M_1 PRT samples because of the development of the well-connected Type 1 microporosity. Therefore, their presence — if there is any — in the M_1 PRT samples will have minimal implications on the first two regions of the displacement curve. In the region of the mid-time rollover, the effect of dead-end pores arises causing little mismatch between data and the model — as for S28 in Fig. 9a. Although, when fluid channeling dominates the displacement in a sample, the mismatch between the data and the model fit will be less, due to the flow in some of the macropores that did not break through yet — as in S107 in Fig. 9b.

In the region of the late-time plateau, the model nicely fit

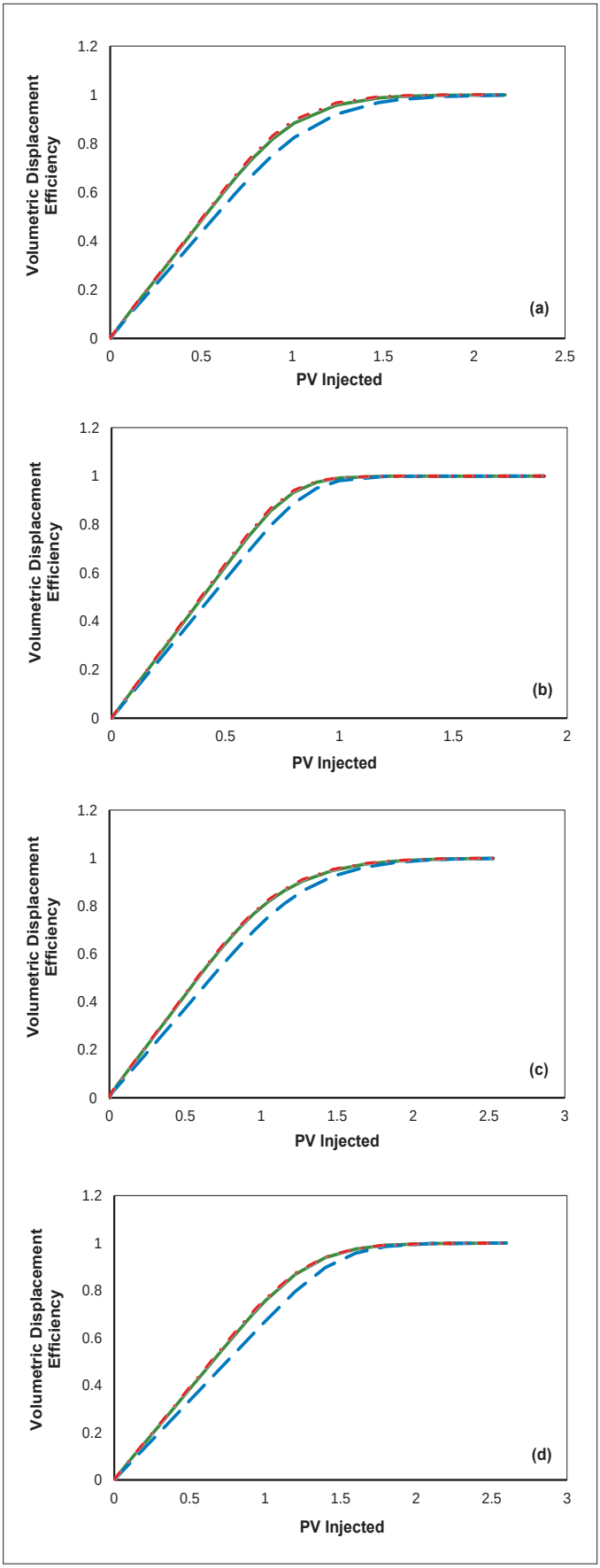

Fig. 11. The M PRT displacement characteristic in S28 at a low dispersion rate (a), S28 at a high dispersion rate (b), S107 at a low dispersion rate (c), and S107 at a high dispersion rate (d). The blue line is for micropartition, the red line for macropartition, and the green line is for the bulk sample.

the data. This is because we normalized the displacement data to the total displaced PV in the sample to eliminate the effect of dead-end pores on the quality of the model fit at this late displacement region, expected to be dominated by diffusion through mass transfer between the flowing pores — as for the M_1 and Type 1 samples — and between the flowing pores and the dead-end pores — as for the M PRT samples. The bulk fit for S104 and S105, Figs. 9e and 9f, is the micro fit since these samples are from the Type 1 PRT, which don't have macropores.

Figure 10 shows the time domain data, from the high injection rate, and convective-dispersion model fits for both the macropores and dead-end pores in the M PRT samples, Figs. 10a and 10b, and the macropores and micropores in the M_1 PRT, Figs. 10c and 10d. In these figures, the bulk fit curves are displayed without the displacement data. We need to evaluate the relative contributions to the bulk dispersive displacement from the different pore systems existing in the M and M_1 PRTs. To do this, we partitioned the dispersive displacement in our carbonate samples into a dispersive displacement through the macropores (macropartition), and another dispersive displacement through the micropores (micropartition).

In addition, we partitioned the fluid displacement between the dead-end pores and the macropores — dead-end pores partition — since these dead-end pores are less, or not connected among each other. The M_1 samples, on the other hand, contains a good portion of Type 1 microporsity as estimated from the NMR T_2 distributions. The Type 1 microporosity in this PRT is characterized as a well-connected network of pores that exist adjacent to well-connected macropores[8]. The behavior of micropartition fits in the M_1 PRT samples are in excellent agreement with that of the bulk fits of S104 and S105 — samples with only microporosity. This implies that the dispersive flow takes place through the micropores of the M_1 PRT in addition to the dominated dispersive flow through the macropores in the M_1 PRT.

Two Flow Rate Injection Data

The displacement characteristics of the M, M_1, and Type 1 PRTs were evaluated at two different injection flow rates, which adjust the displacement from the low to the high dispersion condition. During single-phase displacement, dispersion dominates diffusion for interstitial velocities above 3 cm/day, or approximately 3.5×10^{-5} cm/s[13], which for our 1" diameter core samples, corresponds to about 1.7×10^{-4} cm^3/s. Our low dispersion displacement flow rate is 3.8×10^{-4} cm^3/s, about twice that threshold and the high dispersion flow rate is about 20 times that condition, 3.8×10^{-3} cm^3/s.

Figure 11 shows the two flow rate displacements for S28 and S107, which are classified as containing the M PRT. Figures 11a and 11b show S28 at a low dispersion rate and a high dispersion rate, respectively. Figures 11c and 11d show S107 at a low dispersion rate and a high dispersion rate, re-

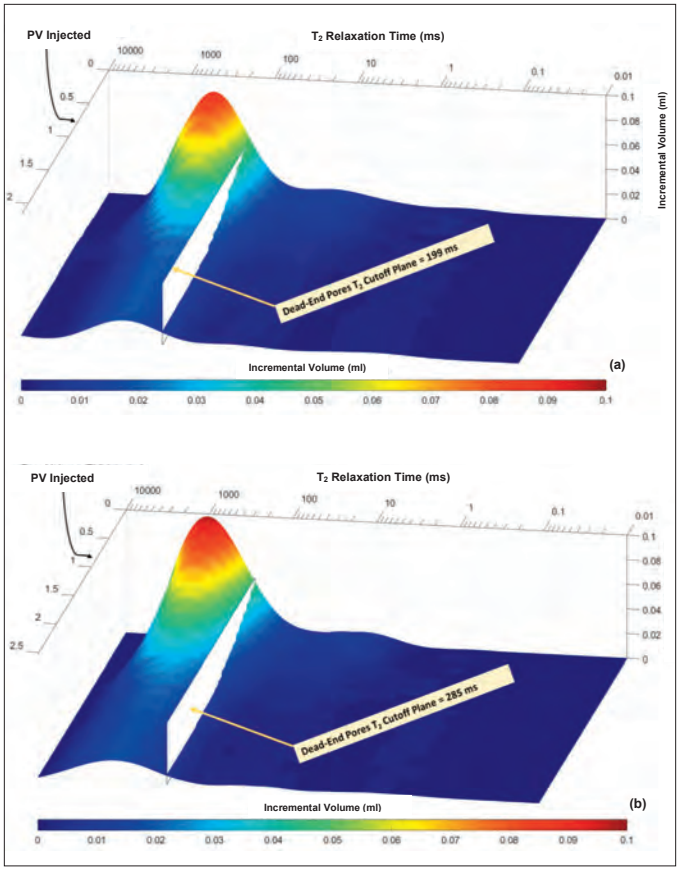

Fig. 12. 3D surface plot of the sequence of the NMR T_2 incremental volume of D_2O brine (z axis and color shading), pore body size by NMR T_2 decay time (x axis) scans ordered by PV injection of the D_2O brine since the start of displacement (y axis) for the M PRT core samples' pore system.

spectively. On the left is the low rate data and on the right is the high rate data. The figures display the bulk results with the analysis of these data using a macropartition and a dead-end partition. Figure 11 clearly shows that the bulk dispersive displacement in the M PRT samples can be adequately fit with only the macropartition solution. This implies that the contribution to the bulk dispersive displacement from the dead-end pores in the M PRTs is not significant — especially in the region of the early linear trend; the region where the dispersive displacement is important. The reason for this is attributed to the diffusive displacement through a mass transfer rate between the dead-end pores and the flowing macropores.

Figure 12 displays the 3D surface plot of the sequence of the NMR T_2 incremental volume of D_2O brine (z axis and color shading), pore body size by NMR T_2 decay time (x axis) scans ordered by PV injection of the D_2O brine since the start of displacement (y axis) for the M PRT core samples' pore system. The declining ridge shown in the left side of the dead-end pore's T_2 cutoff plane — defined as the NMR T_2 value dividing the NMR T_2 distribution into dead-end pores and macropores — in these figures is related to the declining volume of H_2O brine with increasing the PV of the injected D_2O brine in the large M size pores. The next rightward declining ramp is associated with the declining volume of H_2O brine with increasing the PV of the diffused D_2O brine in dead-end pores.

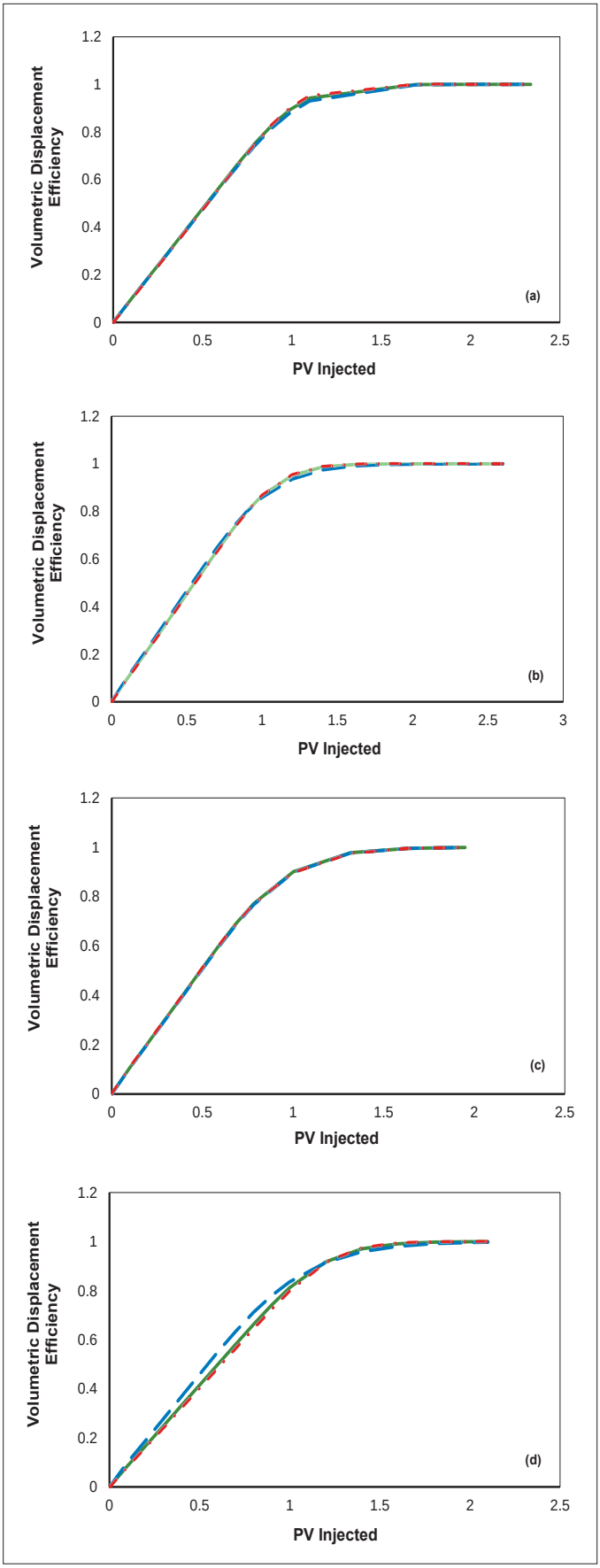

Fig. 13. The M_1 PRT displacement characteristic in S40 at a low dispersion rate (a), S40 at a high dispersion rate (b), S67 at a low dispersion rate (c), and S67 at a high dispersion rate (d). The blue line is for micropartition, the red line is for macropartition, and the green line is for the bulk sample.

The H_2O brine volume declines in each pore type as the hydrogen in the H_2O brine is replaced by deuterium in the D_2O brine; the H_2O incremental volume in either the ridge or the ramp of the common pore body size decline at different rates.

This indicates two distinct pore geometry controlled rates of the displacement progress — one is controlled by the dispersive displacement rate as in the macropores and the other is controlled by the diffusive displacement by the mass transfer rate between the macropores and the dead-end pores. If the mass transfer rate is sufficiently large, dead-end pores will function as flowing pores, due to practically instantaneous mass transfer[22]. The results in Table 4 also show that for the high injection rate, the u within the macropores is about four times that of the dead-end pores; however, we modeled the flow in the dead-end pores (flow partition) using the convective-dispersive model. Therefore, the fitting results from the dead-end pores partition's data — u and bulk dispersion coefficient, K_L, in Table 4 — are not realistic since these pores are not connected among each other's, which violates the assumptions used in the construction of the model.

Figure 13 shows the two flow rate displacements for S40 and S67, which are classified as containing the M_1 PRT. Figures 13a and 13b show S40 at a low dispersion rate and a high dispersion rate, respectively. Figures 13c and 13d show S67 at a low dispersion rate and a high dispersion rate, respectively. On the left is the low rate data and on the right is the high rate data. The two flow rate displacements of the M_1 PRT samples shown clearly suggests that the M only solution will not completely describe the bulk dispersive displacement in the M_1 PRT samples, especially in the region of the early linear trend. Evidently, this illustrates that the micropores in these samples will affect the bulk fluid flow. These M_1 PRT samples contains a good portion of Type 1 microporosity of up to about 50% of the total PV in these samples.

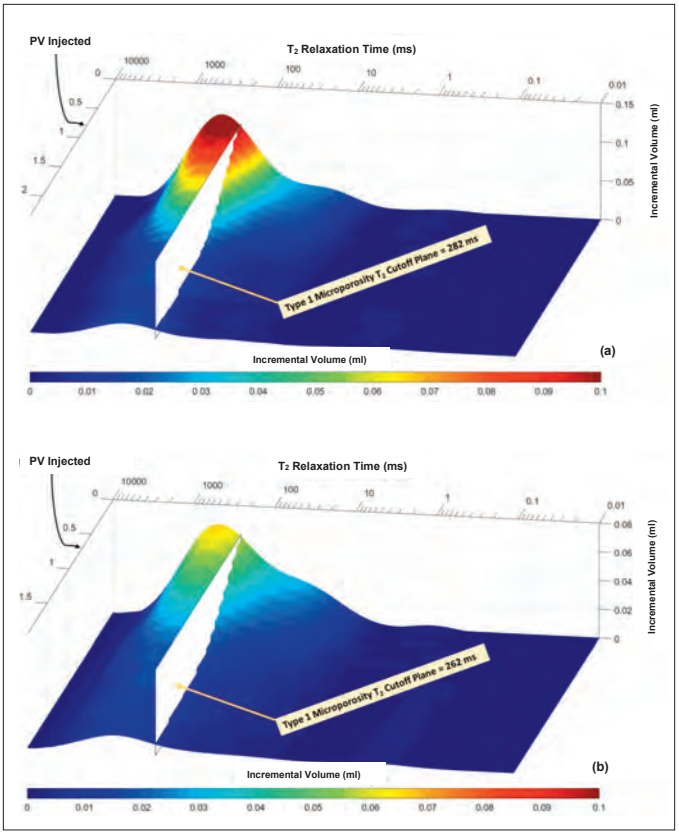

Fig. 14. 3D surface plots of the sequence of NMR T_2 incremental volume of D_2O brine (z axis and color shading), pore body size by NMR T_2 decay time (x axis) scans ordered by PV injected of D_2O brine since the start of displacement (y axis) for the M_1 PRT core samples' pore system.

Figure 13 also shows that the micropores in the two samples are either being displaced first — as in S67, Fig. 13d — or being equally displaced — as in S40, Fig. 13b. For example, for the high rate data of S40 in Fig. 13b, the macropores and micropores showed an equal E_D of about 0.42 after the injection of about 0.5 PV of D_2O brine while in S67, Fig. 13d, the E_D of the micropores — about 0.5 — was higher than that of the macropores — about 0.40.

Figure 14 displays 3D surface plots of the sequence of NMR T_2 incremental volume of D_2O brine (z axis and color shading), pore body size by NMR T_2 decay time (x axis) scans ordered by PV injected of D_2O brine since the start of displacement (y axis) for the M_1 PRT core samples' pore system. The declining ridge shown on the left side of the Type 1 micropore's T_2 cutoff plane — defined as the NMR T_2 value dividing the NMR T_2 distribution into Type 1 micropores and macropores — in these figures is related to the declining volume of H_2O brine with increasing PV of the injected D_2O brine in the large M size pores. The next rightward declining ramp is associated with the declining volume of H_2O brine with increasing the PV of the dispersed D_2O brine in the Type 1 micropores. The H_2O brine volume declines in each pore type as the hydrogen in the H_2O brine is replaced by deuterium in the D_2O brine; the H_2O incremental volume in either the ridge or the ramp of the common pore body size declines at different rates. This indicates two distinct pore geometry controlled rates of the dispersive displacement progress.

The comparison of this M_1 data to the previously discussed M data indicates a different flow dynamic in the M_1 samples. Additionally, the results of these fits suggests that the flow rates of the micropores and the macropores are distinctly different. For example, by utilizing the velocity data (u) in Table 4 for the high injection rate, and by assuming uniform pore body distributions across the cross-sectional area of the core samples and throughout the length of the core samples, the ratio of macro- to micro-interstitial flow rates was estimated to be about 1.86 for S40 and about 0.86 for S67.

The high injection rate displacement data in Fig. 13 may infer that the pore systems in these samples from M_1 PRT are both connected and interconnected as observed by previous work[1, 2, 6, 8]. For example, the distinct gaps in the displacement efficiencies of the macropartitions and micropartitions at the early linear trend region — dispersive displacement dominates the flow — may infer connectivity between similar pore body sizes. On the other hand, the overlaying (or about overlaying) of the displacement efficiencies of the macropartitions and

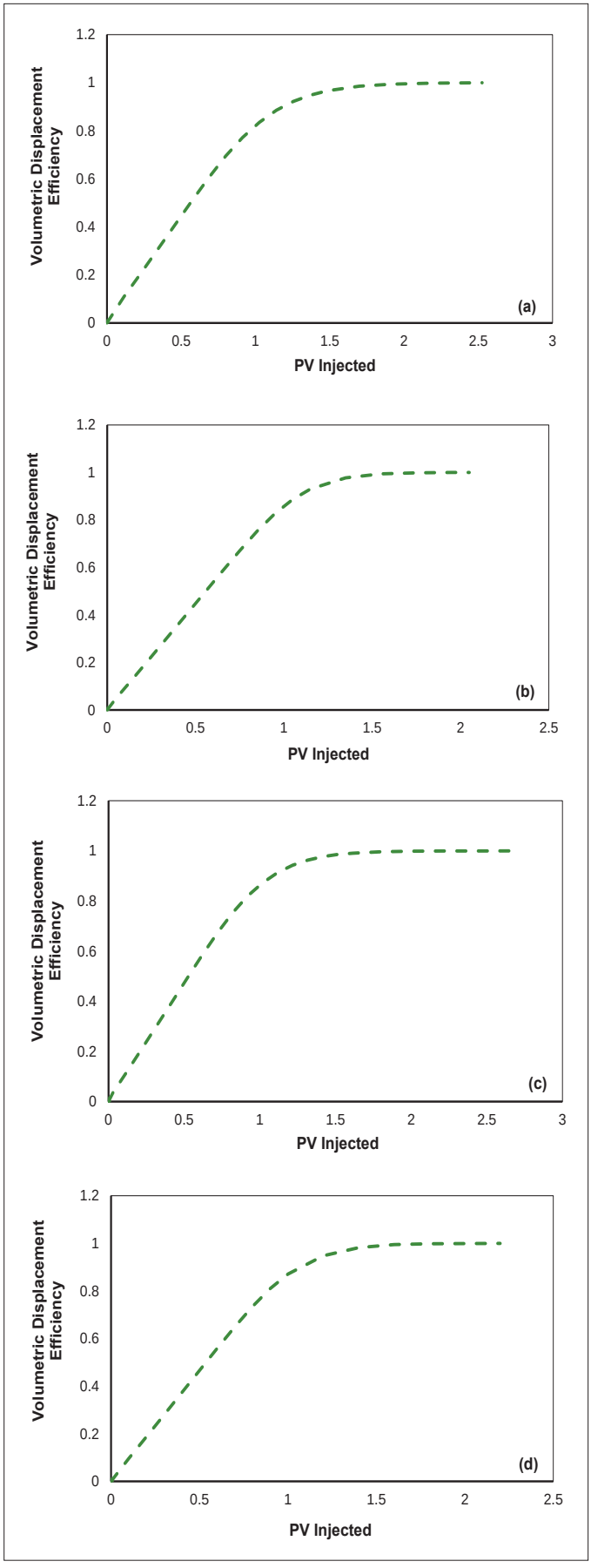

Fig. 15. Type 1 PRT bulk displacement characteristic in S104 at a low dispersion rate (a), S104 at a high dispersion rate (b), S105 at a low dispersion rate (c), and S105 at a high dispersion rate (d).

micropartitions starting in the region of the mid-time rollover and ending in the region of the late-time plateau — diffusive flow by mass transfer rate between the different pore systems is important — may infer interconnectivity between different pore body sizes.

Figure 15 shows the two flow rate displacements for S104 and S105, which are classified as containing the Type 1 PRT. Figures 15a and 15b show S104 at a low dispersion rate and a high dispersion rate, respectively. Figures 15c and 15d show S105 at a low dispersion rate and a high dispersion rate, respectively. On the left is the low rate data and on the right is the high rate data. Figure 15 clearly demonstrates that these Type 1 microporosity samples can be adequately fit using a single mode of dispersion (as shown in Figs. 9e and 9f) and a second one is not required. S104 and S105 show similar permeability — 0.71 millidarcies (md) for S104 and 0.88 md for S105 — and similar porosity — 19.23% for S104 and 20.71% for S105. Furthermore, both samples have identical pore throat distributions as previously displayed. The two samples also have uniform spatial NMR T_2 distributions, suggesting uniformity of pore body distributions along the length of the core samples. The analysis of the dispersion data from these two samples gives almost similar results for the model parameters, Table 4. For example, the N_{PE} for S104 and S105 from the high injection rate results are about 46 and 35, respectively. This demonstrates the similarity in their dispersive displacement with and average N_{PE} of about 40. The Type 1 micropores in the M_1 PRT samples, on the other hand, have an average N_{PE} of about 24, suggesting higher dispersive flow than the samples of the Type 1 PRT.

Pore Connectivity in the M_1 PRT Affects Displacements

The issue of the connectivity between the pore subsystems in a multimodal sample is a wide open and active topic of investigation. This connectivity issue will affect the modeling and the performance of miscible and immiscible displacement processes.

In two-phase flow, oil production from micropores could be modeled by adopting a mass transfer mechanism — oil production by expulsion — between the micropores and macropores in addition to other parameters[9]. The model uses a mass transfer coefficient between the pore systems in the M_1 PRT as an input to estimate the shape factor characterizing the geometric interaction between the different pore types. The mass transfer coefficient could be estimated by using the modeling and experimental approach from the current study with some modifications.

For miscible displacement, the Peclet number becomes an important factor.

The Peclet number for the flowing pore type N_{PE} has the form:

$$N_{PE} = \frac{uL}{\emptyset K_L} \quad (8)$$

where u is fluid flow velocity, L is length of sample, $\emptyset$ is porosity, and K_L is the bulk dispersion coefficient. The Peclet number for the dead-end pore type, N_{PED}, adopted from the spherical model[17], which assumes mass transport occurs through only diffusion between a flowing and a stagnant pore systems, and has the form:

$$N_{PES} = \frac{r_S^2 u}{D_S L} \quad (9)$$

where u is fluid flow velocity, and L is length of sample. According to Corea et al. (1990)[17], r_s is the radius of the porous sphere, and D_S is the diffusion coefficient in the porous sphere. The r_s in Corea model represents the distance the fluid in the stagnant pore travels to reach the flowing pores. In our work, we assume uniform distribution of pores across the cross-sectional area and along the length of a core plug sample, and then we define r_s as the following:

$$r_S = \left(\frac{\frac{porosity\ of\ dead\ end\ pores\ in\ the\ sample}{total\ porosity\ of\ the\ sample} \times diameter\ of\ core\ plug}{2} \right)^2 \quad (10)$$

To estimate the D_S for the dead-end pores in the M PRT samples, we conducted a diffusion experiment using the 12 MHz NMR instrument on S105 of the Type 1 PRT, saturated with H_2O brine. Since S105 has an almost identical NMR T_2 distribution (Fig. 1) as the dead-end pores in the M PRT samples — the Gaussian fits of the dead-end pores in Fig. 6 — we assumed that S105 and the dead-end pores in the M PRT samples will have an identical diffusion coefficient. The measured D_S in S105 has a value of 1.34×10^{-5} cm²/second.

The fluid flow in the M PRT is dominated by the flow in the macropores, Fig. 16, from the one-to-one relationship between the bulk Peclet number and the macro-Peclet number for both injection rates. But the M_1 PRT samples did not show a similar relationship in the two rates, except for S67 at the low rate. This suggests that the dispersion process in the M_1 PRT is affected by the dispersion process of the Type 1 micropores in this PRT. The figure also shows that the Type 1 micropores in the M_1 PRT has an almost one-to-one relationship between the bulk Peclet number and the micro-Peclet number for the low injection rate, indicating the contribution

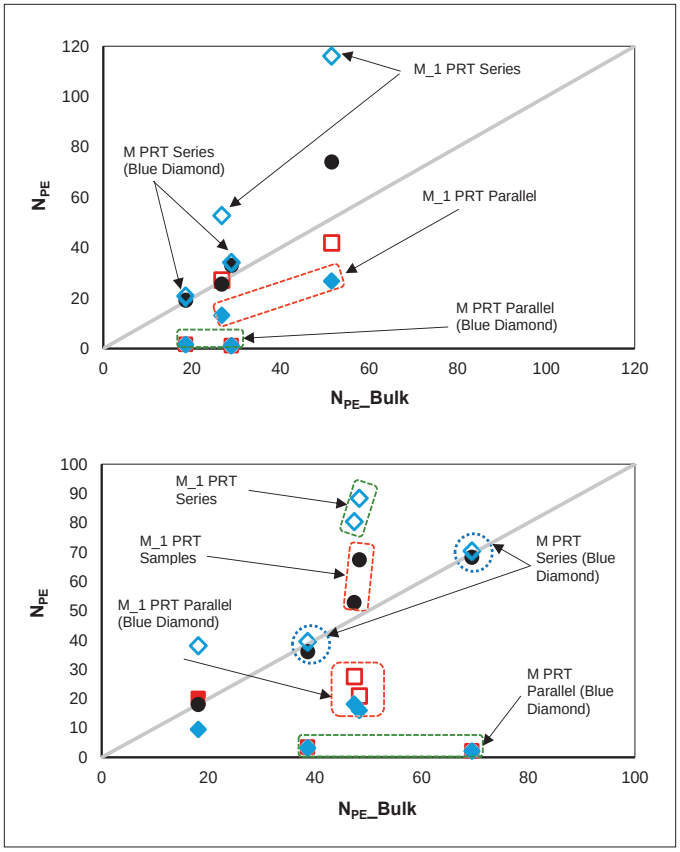

Fig. 16. Bulk N_{PE} comparison with N_{PE} for micropores, dead-end pores, and macropores at a low injection rate (a), and at a high injection rate (b). The macropores (solid black circle), micropores (hollow red square), dead-end pores (solid red square), parallel communication (solid blue diamond), and series communication (hollow blue diamond) are displayed. Data that falls at the equal line (solid gray line) implies more contribution to the bulk flow, and data that falls away from the equal line implies less contribution to the bulk flow.

of the micropores to the bulk dispersive displacement. Consequently, the bulk dispersive displacement is dominated by the macro-dispersive displacement in the M_1 PRT, especially at the high injection rate. The Peclet number of the dead-end pores in the M PRT did not show a one-to-one relationship with the bulk Peclet number, indicating insignificant contribution of the dead-end pores to the bulk dispersive displacement.

In Fig. 16, we also plot the values we have obtained, Table 5, for the pore system parallel Peclet number (using the electrical analogical circuit, resistors, for bimodal pore system, two Peclet numbers; one represents micropores or dead-end pores and the other represents macropores, and are communi-

Sample No.	N_{PE}								Communication			
	Low Dispersion Rate				High Dispersion Rate				Low Dispersion Rate		High Dispersion Rate	
	Macro-partition	Micro-partition	Dead-End Partition	Bulk	Macro-partition	Micro-partition	Dead-End Partition	Bulk	Series	Parallel	Series	Parallel
28	33.00		1.12	28.9	68.20		2.18	69.43	34.19	1.09	70.38	2.11
107	19.20		1.66	18.6	36.04		3.46	38.63	20.85	1.52	39.50	3.16
40	74.00	42.00		51.6	52.80	27.56		47.36	116.07	26.8	80.39	18.11
67	25.60	27.30		26.7	67.40	20.96		48.32	52.83	13.20	88.34	16.00

Table 5. Series and parallel Peclet numbers for the samples of the M and M_1 PRT

cating in parallel configuration with the macro-Peclet number) and the series Peclet number (using the electrical analogical circuit, resistors, for bimodal pore system, two Peclet numbers; one represents micropores or dead-end pores and the other represents macropores, and are communicating in series configuration with the macro-Peclet number) against the bulk Peclet number for the low and high rate displacements. The analysis of this displacement data indicates that for our M_1 PRT samples, the pore systems have both series and parallel communications. The M_1 PRT samples, in the low injection rate, showed more parallel and less series communications with the bulk Peclet number when compared to that of the high injection rate, showing almost equal communications. On the other hand, the dead-end pores in the M PRT showed series communication with the macropores of the M PRT, in both injection rates, suggesting instantaneous mass transfer between the dead-end pores and the macropores.

The design of mixing sensitive displacement processes, such as miscible flooding and surfactant flooding, requires the estimation of the extent of mixing in the reservoir. The results from this study provide a significant insight into the dynamic processes during miscible displacement. In practice, the variation of the length of the miscible zone generally varies[11] as $\sqrt{\frac{1}{N_{PE}}}$. Using this relationship, the results showed that the mixing zone of the micropores in the M_1 PRT could slightly exceed that of macropores during actual reservoir miscible displacement — reservoir rate of 1 ft/day is equivalent to ~0.1 cm^3/min in the 1" core plug, which is closer to the high rate used in this study. This slight variation in mixing zones will then produce diffusive mass transfer due to concentration gradients. As we have only studied two samples from the M_1 PRT, the conclusions of this work cannot be globalized for the entire reservoir with different lithofacies of the M_1 PRT. Currently, we are extending the current study to include several core samples from the M_1 PRT with different lithofacies.

CONCLUSIONS

This NMR monitored dispersion study was conducted to investigate the displacement characteristics in carbonate samples from different PRTs. In addition, the results from modeling the displacement curves using the NMR T_2 partition model provide insight into fluid displacement characteristics, extent of mixing zone, and types of communication taking place within different pore types. The following conclusions were drawn based on the experiments and modeling conducted on the six carbonate samples:

1. The bulk displacement efficiency is dominated by that of the macropores in the M PRT. This indicates that the dead-end pores of the M PRT have negligible contribution to the bulk displacement/flow. This suggests that the contribution of the dead-end pores of the M PRT could be ignored when modeling relative permeability.
2. The bulk displacement efficiency was affected by the displacement efficiency of micropores in the M_1 PRT. This suggests that the micropores of the M_1 PRT have an effective role over displacement/flow in these rock types. This also suggests that the contribution of the micropores in the M_1 PRT must be included when modeling relative permeability.
3. For micropores and macropores in the M_1 PRT, the communication path is through a parallel and series connection. As the injection rate increases, series and parallel communication becomes equally important. This finding provides a crucial information for designing efficient miscible and surfactant flooding for these rock types.

ACKNOWLEDGMENTS

The authors would like to thank the management of Saudi Aramco for their support and permission to publish this article. The authors would also like to thank Mustafa Al Satrawi and Badr Al Zahrani from Saudi Aramco's EXPEC ARC for conducting the experiments.

This article was presented at the SPE Kingdom of Saudi Arabia Annual Technical Symposium and Exhibition, Dammam, Saudi Arabia, April 24-27, 2017.

REFERENCES

1. Clerke, E.A., Mueller, H.W., Phillips, E.C., Eyvazzadeh, R.Y., et al.: "Application of Thomeer Hyperbolas to Decode the Pore Systems, Facies and Reservoir Properties of the Upper Jurassic Arab-D Limestone, Ghawar Field, Saudi Arabia: A 'Rosetta Stone' Approach," *GeoArabia*, Vol. 13, Issue 4, January 2008, pp. 113-160.
2. Cantrell, D.L. and Hagerty, R.M.: "Microporosity in Arab Formation Carbonates, Saudi Arabia," *GeoArabia*, Vol. 4, Issue 2, 1999, pp. 129-154.
3. Cantrell, D.L. and Hagerty, R.M.: "Reservoir Rock Classification, Arab-D Reservoir, Ghawar Field, Saudi Arabia," *GeoArabia*, Vol. 8, January 2003, pp. 435-462.
4. Clerke, E.A.: "Beyond Porosity-Permeability Relationships — Determining Pore Network Parameters for the Ghawar Arab-D Using the Thomeer Method," *GeoFrontier*, Vol. 1, Issue 3, September 2003, pp. 12-17.
5. Clerke, E.A.: "Beyond Porosity-Permeability Relationships: Determining Pore Network Parameters for the Ghawar Arab-D Using the Thomeer Method," *GeoArabia*, Abstract, Vol. 9, Issue 1, 2004, p. 55.
6. Clerke, E.A.: "Permeability, Relative Permeability, Microscopic Displacement Efficiency and Pore Geometry of the M_1 Bimodal Pore Systems in Arab D Limestone," *SPE*

Journal, Vol. 14, Issue 3, September 2009, pp. 524-531.

7. Ahr, W.M., Allen, D., Boyd, A., Bachman, H.N., et al.: "Confronting the Carbonate Conundrum," *Oilfield Review*, Vol. 17, Issue 1, Spring 2005, pp. 18-29.
8. Clerke, E.A., Funk, J.J. and Shtepani, E.: "Spontaneous Imbibition of Water into Oil Saturated M_1 Bimodal Limestone," IPTC paper 17162, presented at the International Petroleum Technology Conference, Beijing, China, March 26-28, 2013.
9. Fung, L.S.K., Middya, U. and Dogru, A.H.: "Numerical Simulation of Fractured Carbonate Reservoirs with the M_1 Bimodal Pore System," SPE paper 142296, presented at the SPE Reservoir Simulation Symposium, The Woodlands, Texas, February 21-23, 2011.
10. Al-Harbi, A.: "Transport Processes in Carbonate Rocks Using NMR T_2 Distributions," M.S. thesis, King Fahd University of Petroleum and Minerals, 2009.
11. Funk, J.J. and Al-Harbi, A.M.: "Modeling Complex Dispersive Capacitance in Carbonates Using NMR T_2 Distributions," SPE paper 126180, presented at the SPE Saudi Arabia Section Technical Symposium, al-Khobar, Saudi Arabia, May 9-11, 2009.
12. Lake, L.W.: *Enhanced Oil Recovery*, Prentice Hall, 1989, 550 p.
13. Deans, H.A.: "A Mathematical Model for Dispersion in the Direction of Flow in Porous Media," *Society of Petroleum Engineers Journal*, Vol. 3, Issue 1, March 1963, pp. 49-52.
14. Bretz, R.E. and Orr Jr., F.M.: "Interpretation of Miscible Displacements in Laboratory Cores," *SPE Reservoir Engineering*, Vol. 2, Issue 4, November 1987, pp. 492-500.
15. Correa, A.C., Pande, K.K., Ramey Jr., H.J., Brigham, W.E.: "Computation and Interpretation of Miscible Displacement Performance in Heterogeneous Porous Media," *SPE Reservoir Engineering*, Vol. 5, Issue 1, February 1990, pp. 69-78.
16. Batycky, J.P., Maini, B.B. and Fisher, D.B.: "Simulation of Miscible Displacement in Full-Diameter Carbonate Cores," *Society of Petroleum Engineers Journal*, Vol. 22, Issue 5, October 1982, pp. 647-657.
17. Skauge, A., Vik, B., Pourmohammadi, S. and Spildo, K.: "Dispersion Measurements Used in Special Core Analysis of Carbonates," SCA paper 2006-14, presented at the International Symposium of the Society of Core Analysts, Trondheim, Norway, September 12-16, 2006.
18. Vik, B., Djurhuus, K., Doublet, D., Spildo, K., et al.: "Characterization of Vuggy Carbonate by Miscible Processes," paper SCA2008-28, presented at the International Symposium of the Society of Core Analysts, Abu Dhabi, UAE, October 29-November 2, 2008.
19. Heide, M.: "Dispersion and Two-Phase Flow in Material from Different Carbonate Pore Classes," M.S. thesis, The University of Bergen, 2008.

BIOGRAPHIES

Dr. Ahmad M. Al-Harbi is a Petroleum Engineer in the Pore Scale Physics Group of the Reservoir Engineering Technology Division in Saudi Aramco's Exploration and Petroleum Engineering Center – Advanced Research Center (EXPEC ARC). His current research focus is seeking solutions for ultimate recovery from Saudi Arabian reservoirs by acquiring deeper understandings of fluid dispersion, pore connectivity, and fluid-rock interaction in porous media.

Ahmad has 15 years of experience in the oil industry with Saudi Aramco. He has been involved with various enhanced oil recovery (EOR) research projects, such as chemical EOR.

In 2001, Ahmad received his B.S. degree in Chemical Engineering from King Fahd University of Petroleum and Minerals (KFUPM), Dhahran, Saudi Arabia, and in 2013, he received his Ph.D. degree in Petroleum Engineering from the University of Calgary, Calgary, Alberta, Canada.

Jun Gao joined Saudi Aramco in October 2015 and is currently working in Saudi Aramco's Exploration and Petroleum Engineering Center – Advanced Research Center (EXPEC ARC) as a Petroleum Scientist with the Reservoir Engineering Technology Division. Prior to joining Saudi Aramco, he worked as a Research Scientist on multiple advanced enhanced oil recovery (EOR) studies for oil companies at Tomographic Imaging and Porous Media Laboratory (TIPM lab) in Perm Inc. and the University of Calgary. Prior to that, Jun worked as a Petroleum Engineer on national chemical EOR research projects at the Geological Scientific Research Institute, Shengli Oil Field Company, and China Petroleum & Chemical Corporation (Sinopec).

He has over 25 years of research experience in special core analysis and EOR, including chemical, thermal, and carbon dioxide techniques, assisted by imaging technologies such as X-ray computer tomography and nuclear magnetic resonance imaging.

Jun received his B.S. degree in Physics from Shandong University, Shandong, China, his B.Eng. degree in Petroleum Engineering from the China University of Petroleum (East China), Qingdao, China, and his M.S. degree in Petroleum Engineering from the University of Calgary, Calgary, Alberta, Canada.

Dr. Hyung T. Kwak joined Saudi Aramco in April 2010 as a Petroleum Engineer with Saudi Aramco's Exploration and Petroleum Engineering Center – Advanced Research Center (EXPEC ARC). He was a member of the pore scale physics focus area (2010 to 2012) and is currently a member of the SmartWater flooding focus area of the Reservoir Engineering Technology Division. Hyung's current research focus is on seeking deeper understanding of the fluid-rock interaction through modeling and experiments that involve injecting SmartWater into carbonates. Since joining Saudi Aramco, he has been involved in various improved oil recovery and enhanced oil recovery (EOR) research projects, such as SmartWater Flooding, CO_2 EOR, and chemical EOR. Prior to Hyung's current position, he was a Research Scientist at Baker Hughes, where the main area of his research was developing low-field NMR/MRI technology.

He received his B.S. degree in Chemistry from the University Pittsburgh, Pittsburgh, PA, in 1996, and his Ph.D. degree in Physical Chemistry from Ohio State University, Columbus, OH, in 2001.

Before moving into the oil and gas industry, Hyung worked as a postdoctoral fellow for 2 years on the project to develop the world's largest wide bore superconducting magnet, 900 MHz, for the nuclear magnetic resonance spectrometer at the National High Magnetic Field Laboratory.

A Year of Innovation

Julie L. Springer

Since the company's first patent in 1950, Saudi Aramco has contributed to the world's innovation efforts with high-value intellectual property (IP), which has positioned the company as a leader in the energy sector.

In 2017, Saudi Aramco achieved its best year yet with 230 granted patents from the United States Patent and Trademark Office, which puts Saudi Aramco third among oil and gas companies worldwide in the number of patents granted.

A well-developed IP portfolio supports Saudi Aramco's competitive advantage, validates the contributions made by our scientists and researchers, solidifies our position as a technology leader in the energy and chemicals fields, and provides commercialization opportunities for non-core technologies. Patents provide value to the company and the Kingdom of Saudi Arabia by enabling Saudi Aramco to deploy these technologies without the fear of competitors taking the idea and deploying the same or similar technology. Patents also enhance the company's reputation as a technology leader, and stimulates the local economy by creating opportunities for new businesses that leverage advanced technology.

Supporting the company's commitment to creating a robust portfolio of IP, the network innovation model that facilitates strategic alliances with world-class organizations has proven successful in enabling Saudi Aramco to enhance its competitiveness and expand its global technology footprint. These collaborations have contributed to the rise in the number of patented technologies that have been developed between Saudi Aramco and our partners, including leading technical innovators in the industry, as well as leading academic institutions in-Kingdom and around the world.

BIOGRAPHY

Julie L. Springer is a Communications Strategist for the Technology, Oversight and Coordination (TOC) Department managing the communication needs in support of the company's downstream, cross-business and sustainability technology portfolios. She has over 17 years of experience providing communications and public relations support to some of the world's most high profile companies, including Shell, Halliburton, and Dell.

Julie is the recipient of both the Public Relations Society of America (PRSA) Bronze Quill Award, and the American Marketing Award for the re-branding and positioning of Shell subsidiary Shell Energy North America.

She received her B.A. degree in Mass Communications and English from Texas State University, San Marcos, TX.

SAUDI ARAMCO PATENTS GRANTED 2017

Cement Oil-Based Mud Spacer Formulation

Granted Patent: U.S. Patent 9,534,164, Grant Date: January 3, 2017

Mohammad L. Al-Subhi, Scott S. Jennings, and Ahmad S. Al-Humaidi

Hydrocracking Process with Feed/Bottoms Treatment

Granted Patent: U.S. Patent 9,534,179, Grant Date: January 3, 2017

Omer R. Koseoglu

Vertical Seismic Profiling-Common Midpoint Gathers (Vsp-Cmp) By Wavefield Extrapolation

Granted Patent: U.S. Patent 9,535,183, Grant Date: January 3, 2017

Bouchaib El-Marhfoul and John C. Owusu

Mixed Salt CO_2 Sorbent, Process for Making and Uses Thereof

Granted Patent: U.S. Patent 9,539,541, Grant Date: January 10, 2017

Esam Z. Hamad, Wajdi I. Al-Sadat, Luke Coleman, J.P. Shen, and Raghubir Gupta

Integrated System for In Situ Organic Peroxide Production and Oxidative Heteroatom Conversion

Granted Patent: U.S. Patent 9,540,572, Grant Date: January 10, 2017

Omer R. Koseoglu and Abdennour Bourane

Dual Purpose Observation and Production Well

Granted Patent: U.S. Patent 9,540,921, Grant Date: January 10, 2017

Abdulaziz A. Al-Ajaji, Fahad A. Al-Ajmi, and Mohammad S. Kanfar

Assembly for Plugging a Tube

Granted Patent: U.S. Patent 9,541,337, Grant Date: January 10, 2017

Abdullah M. Al-Otaibi

Enhancing Properties of Sulfur Extended Asphalt Using Polyethylene Wax

Granted Patent: U.S. Patent 9,546,275, Grant Date: January 17, 2017

Mohammad A. Parvez, Wahhab H. Al-Abdul, Ibnelwaleed A. Hussein, Mohammed H. Al-Mehthel, and Saleh H. Al-Idi

Densifying Carbon Dioxide with a Dispersion of Carbon Dioxide-Philic Water Capsules

Granted Patent: U.S. Patent 9,546,316, Grant Date: January 17, 2017

Fawaz Al-Otaibi, Yun Chang, Sunil L. Kokal, and Howard K. Schmidt

Hydrotreating of Aromatic-Extracted Hydrocarbon Streams

Granted Patent: U.S. Patent 9,546,328, Grant Date: January 17, 2017

Omer R. Koseoglu

Integrated Ebullated-Bed Process for Whole Crude Oil Upgrading

Granted Patent: U.S. Patent 9,546,330, Grant Date: January 17, 2017

Omer R. Koseoglu and Alain P. Ranc

Continuous Rotary Drilling System and Method of Use

Granted Patent: U.S. Patent 9,546,517, Grant Date: January 17, 2017

Shaohua Zhou

Apparatus for Driving and Maneuvering Wireline Logging Tools in High Angled Wells

Granted Patent: U.S. Patent 9,546,544, Grant Date: January 17, 2017

Mohammed S. Al-Badran

Analyzer for Monitoring Salt Content in High Resistivity Fluids

Granted Patent: U.S. Patent 9,546,978, Grant Date: January 17, 2017

Rashed M. Aleisa, Naim Akmal, and Taher A. Al-Amri

Sulfone Cracking Using Supercritical Water

Granted Patent: U.S. Patent 9,550,948, Grant Date: January 24, 2017

Omer R. Koseoglu, Farhan M. Al-Shahrani, and Abdennour Bourane

Dynamic Demulsification System for Use in a Gas-Oil Separation Plant

Granted Patent: U.S. Patent 9,555,345, Grant Date: January 31, 2017

Emad N. Al-Shafei and M. Rashid Khan

Process for Oxidative Desulfurization with Integrated Sulfone Decomposition

Granted Patent: U.S. Patent 9,555,396, Grant Date: January 31, 2017

Omer R. Koseoglu and Abdennour Bourane

Sulfur Recovery Unit

Granted Patent: U.S. Patent 9,556,030, Grant Date: January 31, 2017

John P. O'Connell

Selective Series-Flow Hydroprocessing System and Method

Granted Patent: U.S. Patent 9,556,388, Grant Date: January 31, 2017

Omer R. Koseoglu

Integrated Hydrotreating and Isomerization Process with Aromatic Separation

Granted Patent: U.S. Patent 9,556,389, Grant Date: January 31, 2017

Omer R. Koseoglu

Non-Acidic Exothermic Sandstone Stimulation Fluids

Granted Patent: U.S. Patent 9,556,718, Grant Date: January 31, 2017

Mohammed N. Al-Dahlan, Ayman R. Al-Nakhli, and Abdullah M. Al-Harith

Portable Device and Method for Field Testing Proppant

Granted Patent: U.S. Patent 9,557,254, Grant Date: January 31, 2017

Mohammad H. Alqam, Hazim H. Abass, Hussain A. Al-Shammary, and Edwin T. Caliboso

Demulsification and Extraction of Biochemicals from Crude and Its Fractions Using Water and Subcritical/Supercritical Carbon Dioxide as Proton Pump with pH Tuning without Precipitating Oil Components

Granted Patent: U.S. Patent 9,562,198, Grant Date: February 7, 2017

Zaki Yusuf and Magdy E. Mohamed Gad

Energy Efficient Apparatus Employing Energy Efficient Process Schemes Providing Enhanced Integration of Gasification-based Multi-Generation and Hydrocarbon Refining Facilities and Related Methods

Granted Patent: U.S. Patent 9,562,201, Grant Date: February 7, 2017

Mahmoud B. Noureldin

Adsorbed Natural Gas Storage Facility

Granted Patent: U.S. Patent 9,562,649, Grant Date: February 7, 2017

Yuguo Wang, Cemal Ercan, Mohammed G. Al-Hashim, Anwar H. Al-Khawajah, and Rashid M. Othman

Generating Subterranean Imaging Data Based on Vertical Seismic Profile Data

Granted Patent: U.S. Patent 9,562,983, Grant Date: February 7, 2017

Leon L.Z. Hu

Sour Gas Combustion Using in Situ Oxygen Production and Chemical Looping Combustion

Granted Patent: U.S. Patent 9,566,546, Grant Date: February 14, 2017

Ali Hoteit

Process for Heavy Oil Upgrading in a Double-Wall Reactor

Granted Patent: U.S. Patent 9,567,530, Grant Date: February 14, 2017

Ki-Hyouk Choi, Joo-Hyeong Lee, and Abdullah T. Al-Abdulhadi

Energy Efficient and Environmentally Advanced Configurations for Naphtha Hydrotreating Process

Granted Patent: U.S. Patent 9,568,256, Grant Date: February 14, 2017

Mahmoud B. Noureldin and Ahmed S. Bunaiyan

Evaluation of Rock Boundaries and Acoustic Velocities Using Drill Bit Sound during Vertical Drilling

Granted Patent: U.S. Patent 9,568,629, Grant Date: February 14, 2017

Maher I. Al-Marhoon and Yunlai Yang

Process for Oxidative Desulfurization and Sulfone Management by Gasification

Granted Patent: U.S. Patent 9,574,142, Grant Date: February 21, 2017

Abdennour Bourane, Omer R. Koseoglu, and Stephane C. Kressmann

Desulfurization and Sulfone Removal Using a Coker

Granted Patent: U.S. Patent 9,574,143, Grant Date: February 21, 2017

Abdennour Bourane, Omer R. Koseoglu, and Stephane C. Kressmann

Process for Oxidative Desulfurization and Denitrogenation Using a Fluid Catalytic Cracking (FCC) Unit

Granted Patent: U.S. Patent 9,574,144, Grant Date: February 21, 2017

Abdennour Bourane, Omer R. Koseoglu, and Stephane C. Kressmann

Tethered Transition Metals Promoted Photocatalytic System for Efficient Hydrogen Evolutions

Granted Patent: U.S. Patent 9,579,639, Grant Date: February 28, 2017

Kazuhiro Takanabe, Tayirjan Isimjan, Weili Yu, Silvano Del Gobbo, and Wei Xu

Magnetic Omni-Wheel

Granted Patent: U.S. Patent 9,579,927, Grant Date: February 28, 2017

Brian Parrott, Pablo E. Carrasco Zanini Gonzalez, Ali Outa, Fadl H. Abdel Latif, and Hassane Trigui

Catalysts and Methods for Polymer Synthesis

Granted Patent: U.S. Patent 9,580,547, Grant Date: February 28, 2017

Scott D. Allen, Gabriel E. Job, and Jay J. Farmer

Controlled Release of Surfactants for Enhanced Oil Recovery

Granted Patent: U.S. Patent 9,580,639, Grant Date: February 28, 2017

Yun C. Chang and Mazen Y. Kanj

Integrated Hydrocarbon Desulfurization with Oxidation of Disulfides and Conversion of SO_2 to Elemental Sulfur

Granted Patent: U.S. Patent 9,580,661, Grant Date: February 28, 2017

Omer R. Koseoglu

Reversible Solid Adsorption Method and System Utilizing Waste Heat for On-Board Recovery and Storage of CO_2 from Motor Vehicle Internal Combustion Engine Exhaust Gases

Granted Patent: U.S. Patent 9,581,062, Grant Date: February 28, 2017

Esam Z. Hamad and Wajdi I. Al-Sadat

Pipeline Integrity Monitoring Using Fiber Optics

Granted Patent: U.S. Patent 9,581,490, Grant Date: February 28, 2017

Soliman A. Al-Walaie and Saleh M. Al-Saikhan

Non-Damaging Bimodal Stimulation Composition and Method of Use Thereof

Granted Patent: U.S. Patent 9,587,165, Grant Date: March 7, 2017

Saleh H. Al-Mutairi, Abdul-Hameed Mohsen, Mubarak A. Al-Dhufairi, and Ali D. Al-Aamri

Integrated Hydrotreating and Steam Pyrolysis Process for Direct Processing of a Crude Oil

Granted Patent: U.S. Patent 9,587,185, Grant Date: March 7, 2017

Raheel Shafi, Julio Hasselmeyer, Abdennour Bourane, Ibrahim A. Abba, and Abdul-Rahman Akhras

Packer Setting Method Using Disintegrating Plug

Granted Patent: U.S. Patent 9,587,456, Grant Date: March 7, 2017

Brian A. Roth

Method for Determining Stress in Flexible Joints by Use of Leveling Means

Granted Patent: U.S. Patent 9,587,966, Grant Date: March 7, 2017

Farooq N. Al-Jwesm

Frequency Varying Filtering of Simultaneous Source Seismic Data

Granted Patent: U.S. Patent 9,588,241, Grant Date: March 7, 2017

Shoudong Huo and Hai Xu

Apparatus and Computer Readable Medium for Determining Well Characteristics and Pore Architecture Utilizing Conventional Well Logs

Granted Patent: U.S. Patent 9,588,939, Grant Date: March 7, 2017

Johannes J. Buiting and Nicolas Leseur

Process for Preparing Lipid Coated Particles of Plant Material

Granted Patent: U.S. Patent 9,592,488, Grant Date: March 14, 2017

Zaki Yusuf, Bandar Fadhel, and Ahmad D. Hammad

Sulfur Recovery Process for Treating Low to Medium Mole Percent Hydrogen Sulfide Gas Feeds with BTEX in a Claus Unit

Granted Patent: U.S. Patent 9,593,015, Grant Date: March 14, 2017

Jean-Pierre R. Ballaguet, Milind M. Vaidya, Sebastien A. Duval, Aadesh Harale, Anwar H. Khawajah, and Veera V.R. Tammana

Process for the Hydration of Mixed Butenes to Produce Mixed Alcohols

Granted Patent: U.S. Patent 9,593,059, Grant Date: March 14, 2017

Wei Xu, Farhan M. Al-Shahrani, Abdennour Bourane, and Stephan R. Vogel

Metal Complexes

Granted Patent: U.S. Patent 9,593,203, Grant Date: March 14, 2017

Scott D. Allen, Jay J. Farmer, Gabriel E. Job, and Anna E. Cherian

Hanger and Penetrator for Through Tubing ESP Deployment with a Vertical Production Tree

Granted Patent: U.S. Patent 9,593,561, Grant Date: March 14, 2017

Jinjiang Xiao, Brian A. Roth, and Brett W. Bouldin

Well Completion Sliding Sleeve Valve-based Sampling System and Method

Granted Patent: U.S. Patent 9,593,574, Grant Date: March 14, 2017

Alwaleed A. Al-Gouhi

Energy Efficient and Environmentally Advanced Configurations for Naphtha Hydrotreating Process

Granted Patent: U.S. Patent 9,593,888, Grant Date: March 14, 2017

Mahmoud B. Noureldin and Ahmed S. Bunaiyan

Fast Beam Migration Using Plane-Wave Destructor (PWD) Beam Forming

Granted Patent: U.S. Patent 9,594,176, Grant Date: March 14, 2017

Alexander M. Popovici, Sergey Fomel, Nicolay Tanushev, Iulian F. Musat, Ioan Sturzu, and Constantinos X. Tsingas

Ethylene Oligomerization Process

Granted Patent: U.S. Patent 9,598,329, Grant Date: March 21, 2017

Kareemuddin M. Shaik and Wei Xu

Process for Oxidative Desulfurization and Sulfone Disposal Using Solvent Deasphalting

Granted Patent: U.S. Patent 9,598,647, Grant Date: March 21, 2017

Abdennour Bourane, Omer R. Koseoglu, and Stephane C. Kressmann

Integrated Process for CO_2 Capture and Use in Thermal Power Production Cycle

Granted Patent: U.S. Patent 9,598,993, Grant Date: March 21, 2017

Mourad V. Younes, Wajdi I. Al-Sadat, and Esam Z. Hamad

Nuclear Magnetic Resonance Gas Isotherm Technique to Evaluate Reservoir Rock Wettability

Granted Patent: U.S. Patent 9,599,581, Grant Date: March 21, 2017

Hyung T. Kwak and Ahmad M. Al-Harbi

Synthesis of Ordered Microporous Carbons by Chemical Vapor Deposition

Granted Patent: U.S. Patent 9,604,194, Grant Date: March 28, 2017

Yuguo Wang, Cemal Ercan, Rashid M. Othman, Minkee Choi, and Seokin Choi

Series-Parallel Electric Hybrid Powertrain with Multi-Fuel Capabilities

Granted Patent: U.S. Patent 9,604,527, Grant Date: March 28, 2017

Vittorio Manente

Method for the Fluidized Catalytic Cracking of a Heavy Hydrocarbon Feedstock

Granted Patent: U.S. Patent 9,605,213, Grant Date: March 28, 2017

Musaed S. Al-Ghrami, Cemal Ercan, Sulaiman S. Al-Khattaf, Mohammed A.B. Siddiqui, and Abdullah M. Aitani

Energy Efficient Gasification-based Multi-Generation Apparatus Employing Advanced Process Schemes and Related Methods

Granted Patent: U.S. Patent 9,605,220, Grant Date: March 28, 2017

Mahmoud B. Noureldin

Energy Efficient Gasification-based Multi-Generation Apparatus Employing Energy Efficient Gasification Plant-Directed Process Schemes and Related Methods

Granted Patent: U.S. Patent 9,605,221, Grant Date: March 28, 2017

Mahmoud B. Noureldin

Method and Composition for Contemporaneously Dimerizing and Hydrating a Feed Having Butene to Produce a Fuel Additive Composition

Granted Patent: U.S. Patent 9,605,226, Grant Date: March 28, 2017

Wei Xu, Thamer A. Mohammad, Aadesh Harale, and Kareemuddin M. Shaik

Clamp Device for Vertical Pump Coupling Alignment

Granted Patent: U.S. Patent 9,605,703, Grant Date: March 28, 2017

Mohammad M. Halabi

Turbulence-Inducing Devices for Tubular Heat Exchangers

Granted Patent: U.S. Patent 9,605,913, Grant Date: March 28, 2017

Abdullah M. Al-Otaibi

Methods for Simultaneous Process and Utility Systems Synthesis in Partially and Fully Decentralized Environments

Granted Patent: U.S. Patent 9,606,594, Grant Date: March 28, 2017

Mahmoud B. Noureldin, Mana M. Al-Owaidh, Abdulaziz M. Al-Nutaifi, and Faisal F. Al-Musa

Downhole Self-Isolating Wellbore Drilling Systems

Granted Patent: U.S. Patent 9,611,700, Grant Date: April 4, 2017

Shaohua Zhou

Borehole Electric Field Survey with Improved Discrimination of Subsurface Features

Granted Patent: U.S. Patent 9,611,736, Grant Date: April 4, 2017

Alberto F. Marsala and Andrew D. Hibbs

Machines, Systems, and Methods for Super-Virtual Borehole Sonic Interferometry

Granted Patent: U.S. Patent 9,612,352, Grant Date: April 4, 2017

Abdulrahman A. Shuhail, Ali A. Aldawood, and Abdullatif Al-Shuhail

Systems and Computer Programs for Simultaneous Process and Utility Systems Synthesis in Partially and Fully Decentralized Environments

Granted Patent: U.S. Patent 9,612,635, Grant Date: April 4, 2017

Mahmoud B. Noureldin, Mana M. Al-Owaidh, Abdul-Aziz Al-Nutaifi, and Faisal F. Al-Musa

Floor Mat System and Associated, Computer Medium and Computer Implemented Methods for Monitoring and Improving Health and Productivity of Employees

Granted Patent: U.S. Patent 9,615,746, Grant Date: April 4, 2017

Samantha J. Horseman

Expandable Tool Having Helical Geometry

Granted Patent: U.S. Patent 9,617,802, Grant Date: April 4, 2017

Rafael A. Lastra

Method of Making Sulfur Extended Asphalt Modified with Crumb Rubber

Granted Patent: U.S. Patent 9,624,351, Grant Date: April 18, 2017

Mohammed H. Al-Mehthel, Mohammad A. Parvez, Hamad I. Al-Abdul Wahhab, Ibnelwaleed A. Hussein, and Saleh H. Al-Idi

Application of Downhole Rotary Tractor

Granted Patent: U.S. Patent 9,624,723, Grant Date: April 18, 2017

Scott D. Fraser

Electrodynamic and Electromagnetic Suspension System Tractor

Granted Patent: U.S. Patent 9,624,743, Grant Date: April 18, 2017

Mohammed S. Al-Dabbous

Method of Evaluating Rock Properties While Drilling Using Downhole Acoustic Sensors and Telemetry System

Granted Patent: U.S. Patent 9,624,768, Grant Date: April 18, 2017

Yunlai Yang

Image-based Analysis of a Geological Thin Section

Granted Patent: U.S. Patent 9,626,771, Grant Date: April 18, 2017

Mokhles M. Mezghani and Salem H. Shammari

Encapsulation and Controlled Delivery of Strong Mineral Acids

Granted Patent: U.S. Patent 9,631,139, Grant Date: April 25, 2017

Ghaithan Al-Muntasheri, Ginger D. Rothrock, Leah M. Johnson, and Sarah Shepherd

Method and Apparatus for Downhole Alignment of Optic Fibers

Granted Patent: U.S. Patent 9,631,482, Grant Date: April 25, 2017

Brian A. Roth

Catalyst to Attain Low Sulfur Gasoline

Granted Patent: U.S. Patent 9,636,662, Grant Date: May 2, 2017

Ki-Hyouk Choi, Sameer A. Al-Ghamdi, Ali H. Al-Shareef, and Ali H. Al-Hamadah

Sulfur Asphalt in Roofing, Damp-Proofing and Water Proofing

Granted Patent: U.S. Patent 9,637,635, Grant Date: May 2, 2017

Mohammed H. Al-Mehthel, Hamad I. Al-Abdul Wahhab, Saleh H. Al-Idi, and Ibnelwaleed A. Hussein

Process for Reducing the Total Acid Number in Refinery Feedstocks

Granted Patent: U.S. Patent 9,637,689, Grant Date: May 2, 2017

Adnan Al-Hajji, Omer R. Koseoglu, Hendrik Muller, and Hanadi Al-Jawad

Integrated System for in Situ Organic Peroxide Production and Oxidative Heteroatom Conversion and Hydrotreating

Granted Patent: U.S. Patent 9,637,690, Grant Date: May 2, 2017

Omer R. Koseoglu and Abdennour Bourane

System, Method, and Apparatus for Daisy Chain Network Protection from Node Malfunction or Power Outage

Granted Patent: U.S. Patent 9,641,245, Grant Date: May 2, 2017

Soliman A. Al-Walaie and Muhammad S. Al-Juaid

Targeted Desulfurization Apparatus Integrating Oxidative Desulfurization and Hydrodesulfurization to Produce Diesel Fuel Having an Ultra-Low Level of Organosulfur Compounds

Granted Patent: U.S. Patent 9,644,156, Grant Date: May 9, 2017

Abdennour Bourane, Omer R. Koseoglu, and Mohammed I. Katheeri

Electromagnetic Assisted Ceramic Materials for Heavy Oil Recovery and In Situ Steam Generation

Granted Patent: U.S. Patent 9,644,464, Grant Date: May 9, 2017

Sameeh I. Batarseh

System and Method for Generating Power and Enhanced Oil Recovery

Granted Patent: U.S. Patent 9,647,286, Grant Date: May 9, 2017

Aqil Jamal, Thang V. Pham, and Aadesh Harale

Polymer Nanocomposites and Methods of Making Nanocomposites

Granted Patent: U.S. Patent 9,650,494, Grant Date: May 16, 2017

Ye Chen, Jing Tao, Lin Deng, and Niveen Khashab

Steam Cracking Process and System with Integral Vapor-Liquid Separation

Granted Patent: U.S. Patent 9,650,576, Grant Date: May 16, 2017

Abdul-Rahman Akhras, Abdennour Bourane, Raheel Shafi, and Ibrahim A. Abba

Sealing a Portion of a Wellbore

Granted Patent: U.S. Patent 9,650,859, Grant Date: May 16, 2017

Shaohua Zhou

Mapping Resistivity Distribution within the Earth

Granted Patent: U.S. Patent 9,651,700, Grant Date: May 16, 2017

Alberto F. Marsala, Andrew D. Hibbs, and Todor Petrov

System and Method for Producing Display of Petrophysical Property Height Profile for Both Vertical and Horizontal Wellbores

Granted Patent: U.S. Patent 9,652,565, Grant Date: May 16, 2017

Steven D. Russell, Muhammad Razi B. Abu-Bakar, and Khalid S. Al-Wahabi

Process for Upgrading Heavy and Highly Waxy Crude Oil without Supply of Hydrogen

Granted Patent: U.S. Patent 9,656,230, Grant Date: May 23, 2017

Ki-Hyouk Choi

Process for Producing Aromatics from Wide Boiling Temperature Hydrocarbon Feedstocks

Granted Patent: U.S. Patent 9,657,238, Grant Date: May 23, 2017

Raed Abudawoud and Mohammed Al-Amer

Wireline Crawler Tractor

Granted Patent: U.S. Patent 9,657,542, Grant Date: May 23, 2017

Abdulrahman A. Al-Mulhem

Steam Generation System having Multiple Combustion Chambers and Dry Flue Gas Cleaning

Granted Patent: U.S. Patent 9,657,937, Grant Date: May 23, 2017

Tidjani Niass

Catalytic Compositions Useful in Removal of Sulfur Compounds from Gaseous Hydrocarbons, Processes for Making these and Uses Thereof

Granted Patent: U.S. Patent 9,663,725, Grant Date: May 30, 2017

Abdennour Bourane, Omer R. Koseoglu, Zinfer Ismagilov, Svetlana Yashnik, Mikhail Kerzhentsev, and Valentin Parmon

Process for Heavy Oil Upgrading in a Double-Wall Reactor

Granted Patent: U.S. Patent 9,670,419, Grant Date: June 6, 2017

Ki-Hyouk Choi, Joo-Hyeong Lee, and Abdullah T. Al-Abdulhadi

Apparatus and Method for Producing Oil and Gas Using Buoyancy Effect

Granted Patent: U.S. Patent 9,670,754, Grant Date: June 6, 2017

Mari H. Al-Qahtani

Real-Time Dynamic Data Validation Methods for Intelligent Fields

Granted Patent: U.S. Patent 9,671,524, Grant Date: June 6, 2017

Abdel-Nasser Abitrabi, Fahad Al-Ajmi, Majed Awajy, and Marc Lamontagne

Determining Continuous Capillary Pressure Curves for Subsurface Earth Formations Using Saturation and NMR Log Data

Granted Patent: U.S. Patent 9,671,525, Grant Date: June 6, 2017

Mustafa Al-Ibrahim, Mokhles M. Mezghani, and Johannes J. Buiting

High Performance and Grid Computing with Liveliness and Deadlines Fault Tolerant Data Distributor Quality of Service

Granted Patent: U.S. Patent 9,674,033, Grant Date: June 6, 2017

Raed A. Al-Shaikh and Sadiq M. Sait

Controlling Flow of Black Powder in Hydrocarbon Pipelines

Granted Patent: U.S. Patent 9,675,979, Grant Date: June 13, 2017

James C. Hassell

Three-Dimensional Multi-Modal Core and Geological Modeling for Optimal Field Development

Granted Patent: U.S. Patent 9,684,084, Grant Date: June 20, 2017

Roger R. Sung and Edward A. Clerke

Dynamic Threshold Methods for Filtering Noise and Restoring Attenuated High-Frequency Components of Acoustic Signals

Granted Patent: U.S. Patent 9,684,087, Grant Date: June 20, 2017

Yunlai Yang

Sulfur Management and Utilization in Molten Metal Anode Solid Oxide Fuel Cells Fuels Cells

Granted Patent: U.S. Patent 9,685,675, Grant Date: June 20, 2017

Stamatios Souentie, Yasmeen A. Dawsari, and Esam Z. Hamad

Integrated Systems and Methods for Separation and Extraction of Polynuclear Aromatic Hydrocarbons, Heterocyclic Compounds, and Organometallic Compounds from Hydrocarbon Feedstocks

Granted Patent: U.S. Patent 9,688,923, Grant Date: June 27, 2017

Zaki Yusuf and Alberto L. Ballesteros

Systems for Monitoring and Improving Biometric Health of Employees

Granted Patent: U.S. Patent 9,693,734, Grant Date: July 4, 2017

Samantha J. Horseman

Method for Killing and Removing Microorganisms and Scale Using Separation Unit Equipped with Rotating Magnets

Granted Patent: U.S. Patent 9,694,303, Grant Date: July 4, 2017

Faisal M. Al-Abbas and Anthony Kakpovbia

Method of Conversion of a Drilling Mud to a Gel-based Lost Circulation Material to Combat Lost Circulation during Continuous Drilling

Granted Patent: U.S. Patent 9,695,653, Grant Date: July 4, 2017

Md. Amanullah, Turki T. Al-Subaie, Abdulaziz S. Bubshait, and Omar A. Al-Fuwaires

Dynamic Threshold Systems, Computer Readable Medium, and Program Code for Filtering Noise and Restoring Attenuated High-Frequency Components of Acoustic Signals

Granted Patent: U.S. Patent 9,696,444, Grant Date: July 4, 2017

Yunlai Yang

Induced Polarization Logging with Borehole to Surface Electromagnetic Transmitter

Granted Patent: U.S. Patent 9,696,450, Grant Date: July 4, 2017

Alberto F. Marsala, Muhammad H. Al-Buali, Tang Biyan, and Zhanxiang He

Claus Process for Sulfur Recovery with Intermediate Water Vapor Removal by Adsorption

Granted Patent: U.S. Patent 9,701,537, Grant Date: July 11, 2017

Cemal Ercan, Rashid M. Othman, and Yuguo Wang

Method for Enhanced Fracture Cleanup Using Redox Treatment

Granted Patent: U.S. Patent 9,701,894, Grant Date: July 11, 2017

Ayman R. Al-Nakhli, Hazim H. Abass, and Ahmad S. Al-Otaibi

Advanced Control of Severe Fluid Catalytic Cracking Process for Maximizing Propylene Production from Petroleum Feedstock

Granted Patent: U.S. Patent 9,701,914, Grant Date: July 11, 2017

M. Rashid Khan and Othman A. Taha

Expandable Liner Hanger and Method of Use

Granted Patent: U.S. Patent 9,702,229, Grant Date: July 11, 2017

Shaohua Zhou

Method and Apparatus for in-Well Wireless Control Using Infrasound Sources

Granted Patent: U.S. Patent 9,702,242, Grant Date: July 11, 2017

Mohamed N. Noui-Mehidi and Michael J. Black

Oil Field Process Control System

Granted Patent: U.S. Patent 9,705,934, Grant Date: July 11, 2017

Patrick S. Flanders, Abdelghani A. Daraiseh, Saeed Al-Abeediah, Ralph Hartman, and Abdullah S. Al-Nufaii

Centrally Threaded Plug for Heat Exchanger Tube and Removal Tool

Granted Patent: U.S. Patent 9,709,346, Grant Date: July 18, 2017

Dhawi A. Al-Otaibi

Computer Mouse System and Associated, Computer Medium and Computer Implemented Methods for Monitoring and Improving Health and Productivity of Employees

Granted Patent: U.S. Patent 9,710,788, Grant Date: July 18, 2017

Samantha J. Horseman

Catalyst and Process for Thermo-Neutral Reforming of Liquid Hydrocarbons

Granted Patent: U.S. Patent 9,714,169, Grant Date: July 25, 2017

Fahad I. Al-Muhaish, Shakeel Ahmed, Roberto C. Pontes Bittencourt, Mauri J. Baldini Cardoso, and Vivian P. de Souza

Hydrotreating System for Aromatic-Extracted Hydrocarbon Streams

Granted Patent: U.S. Patent 9,714,392, Grant Date: July 25, 2017

Omer R. Koseoglu

Multiphase in Situ Flow Sensing with Ultrasonic Tomography and Vortex Shedding

Granted Patent: U.S. Patent 9,714,854, Grant Date: July 25, 2017

Michael J. Black, Mohamed N. Noui-Mehidi, and Talha J. Ahmad

Simultaneous Gas Chromatograph Analysis of a Multi-Stream Natural Gas Upgrade Generated through a Multi-Membrane Process

Granted Patent: U.S. Patent 9,714,925, Grant Date: July 25, 2017

Naim Akmal, Saeed H. Al-Shahrani, Anwar H. Al-Khawajah, Milind M. Vaidya, Jean-Pierre R. Ballaguet, and Sebastien A. Duval

Bimetallic Titania-based Electrocatalysts Deposited on Ionic Conductors for Hydrodesulfurization Reactions

Granted Patent: U.S. Patent 9,718,046, Grant Date: August 1, 2017

Ahmad D. Hammad, Esam Z. Hamad, George Panagiotou, Christos Kordulis, and Demetrios Theleritis

Oxidative Desulfurization Process and System Using Gaseous Oxidant-Enhanced Feed

Granted Patent: U.S. Patent 9,719,029, Grant Date: August 1, 2017

Omer R. Koseoglu and Abdennour Bourane

Formation Swelling Control Using Heat Treatment

Granted Patent: U.S. Patent 9,719,328, Grant Date: August 1, 2017

Khaled A. Al-Buraik

Method and Apparatus for Zonal Isolation and Selective Treatments of Subterranean Formations

Granted Patent: U.S. Patent 9,719,336, Grant Date: August 1, 2017

Jack D. Lynn

Seismic Image Filtering Machine to Generate a Filtered Seismic Image, Program Products, and Related Methods

Granted Patent: U.S. Patent 9,720,119, Grant Date: August 1, 2017

Saleh M. Al-Saleh

Tomographic Imaging of Multiphase Flows

Granted Patent: U.S. Patent 9,721,336, Grant Date: August 1, 2017

Michael J. Black, Talha J. Ahmad, and Mohamed N. Noui-Mehidi

Systems, Computer Medium and Computer Implemented Methods for Harvesting Human Energy in the Workplace

Granted Patent: U.S. Patent 9,722,472, Grant Date: August 1, 2017

Samantha J. Horseman and Ronald Monsen

Systems, Methods, and Computer Medium to Provide Adaptive Priority Scheduling of Communications over a Network and Dynamic Resources Allocation among Devices within the Network

Granted Patent: U.S. Patent 9,722,951, Grant Date: August 1, 2017

Soloman M. Al-Madi

Integrated Nodes, Computer Readable Media and Program Products, and Computer Implemented Methods for Providing an Integrated Node for Data Acquisition, Verification and Conditioning, and for Remote Subsystem Control

Granted Patent: U.S. Patent 9,723,060, Grant Date: August 1, 2017

Soloman M. Al-Madi, Soliman A. Al-Walaie, and Tofig A. Al-Dhubaib

Delayed Coking Plant Combined Heating and Power Generation

Granted Patent: U.S. Patent 9,725,652, Grant Date: August 8, 2017

Mahmoud B. Noureldin and Hani M. Al-Saed

Process for Production of Mixed Butanols and Diisobutenes as Fuel Blending Components

Granted Patent: U.S. Patent 9,732,018, Grant Date: August 15, 2017

Kareemuddin M. Shaik, Wei Xu, Ibrahim A. Abba, Thamer Mohammed, Hiren Shethna, and Kadhim A. Mohammed

Systems, Methods, and Computer Medium to Optimize Storage for Hydrocarbon Reservoir Simulation

Granted Patent: U.S. Patent 9,732,593, Grant Date: August 15, 2017

Ahmed S. Al-Zawawi, Santiago A. Ganis, Abdulaziz Al-Subaie, Majdi Baddourah, and Badr M. Al-Harbi

Methods for the Synthesis of Polycyclic Guanidine Compounds

Granted Patent: U.S. Patent 9,738,647, Grant Date: August 22, 2017

Alexei A. Gridnev

Tight Gas Stimulation by in Situ Nitrogen Generation

Granted Patent: U.S. Patent 9,738,824, Grant Date: August 22, 2017

Ayman R. Al-Nakhli, Hazim H. Abass, and Ali A. Al-Taq

Variable Cone Flow Meter

Granted Patent: U.S. Patent 9,739,651, Grant Date: August 22, 2017

Abdullah M. Al-Otaibi

Method and Apparatus for Testing Gel-based Lost Circulation Materials

Granted Patent: U.S. Patent 9,739,694, Grant Date: August 22, 2017

Md. Amanullah and Turki T. Al-Subaie

Electromagnetic Time-Lapse Remote Sensing of Reservoir Conditions

Granted Patent: U.S. Patent 9,739,905, Grant Date: August 22, 2017

Armando R. Sena

System and Method for Harvesting Energy Downhole from an Isothermal Segment of a Wellbore

Granted Patent: U.S. Patent 9,741,916, Grant Date: August 22, 2017

Mohamed N. Noui-Mehidi

Auto Thermal Reforming (ATR) Catalytic Structures

Granted Patent: U.S. Patent 9,745,191, Grant Date: August 29, 2017

Thang V. Pham, Sai P. Katikaneni, Jorge N. Beltramini, Moses O. Adebajo, Joao C.D. da Costa, and Gao Q. Lu

Kalina Cycle-based Conversion of Gas Processing Plant Waste Heat into Power

Granted Patent: U.S. Patent 9,745,871, Grant Date: August 29, 2017

Mahmoud B. Noureldin and Akram H. Kamel

System, Machine, and Computer Readable Storage Medium for Forming an Enhanced Seismic Trace Using a Virtual Seismic Array

Granted Patent: U.S. Patent 9,753,165, Grant Date: September 5, 2017

Ibrahim A. Al-Hukail and Luc Ikelle

Systems, Program Code, Computer Readable Media for Planning and Retrofit of Energy Efficient Eco-Industrial Parks through Inter-Time-Inter-Systems Energy Integration

Granted Patent: U.S. Patent 9,760,099, Grant Date: September 12, 2017

Mahmoud B. Noureldin, Abdulaziz M. Al-Nutaifi, and Mana M. Al-Owaidh

Control of Fluid Catalytic Cracking Process for Minimizing Additive Usage in the Desulfurization of Petroleum Feedstocks

Granted Patent: U.S. Patent 9,764,314, Grant Date: September 19, 2017

Saeed S. Al-Alloush, Othman A. Taha, and M. Rashid Khan

Automation and Control of Energy Efficient Fluid Catalytic Cracking Processes for Maximizing Value Added Products

Granted Patent: U.S. Patent 9,765,262, Grant Date: September 19, 2017

Othman A. Taha and M. Rashid Khan

Chemical Looping Combustion Process with Multiple Fuel Reaction Zones and Gravity Feed of Oxidized Particles

Granted Patent: U.S. Patent 9,765,961, Grant Date: September 19, 2017

Ali Hoteit

Metal Complexes

Granted Patent: U.S. Patent 9,771,388, Grant Date: September 26, 2017

Gabriel E. Job, Scott D. Allen, Christopher A. Simoneau, Ronald Valente, and Jay J. Farmer

Production of Upgraded Petroleum by Supercritical Water

Granted Patent: U.S. Patent 9,771,527, Grant Date: September 26, 2017

Ki-Hyouk Choi, Joo-Hyeong Lee, Mohammad S. Garhoush, and Ali H. Alshareef

Integrated Slurry Hydroprocessing and Steam Pyrolysis of Crude Oil to Produce Petrochemicals

Granted Patent: U.S. Patent 9,771,530, Grant Date: September 26, 2017

Essam Sayed, Raheel Shafi, Abdul-Rahman Akhras, Abdennour Bourane, and Ibrahim A. Abba

Vibrator Sub

Granted Patent: U.S. Patent 9,771,770, Grant Date: September 26, 2017

Abdulrahman A. Al-Mulhem

Sensor for Monitoring for the Presence and Measurement of Aqueous Aldehyde Biocides

Granted Patent: U.S. Patent 9,772,287, Grant Date: September 26, 2017

Mohammed A. Al-Moniee, Naim Akmal, Peter F. Sanders, and Fahad N. Al-Abeedi

Classification Scheme of Sized Bridging Materials for Superior Drill-In Fluid Design

Granted Patent: U.S. Patent 9,772,320, Grant Date: September 26, 2017

Md. Amanullah

Correcting Time-Lapse Seismic Data for Overburden and Recording Effects

Granted Patent: U.S. Patent 9,772,415, Grant Date: September 26, 2017

Roy M. Burnstad

Method of Using Concentrated Solar Power (CSP) for Thermal Gas Well Deliquification

Granted Patent: U.S. Patent 9,777,562, Grant Date: October 3, 2017

Rafael A. Lastra and Abubaker S. Saeed

Slug Flow Monitoring and Gas Measurement

Granted Patent: U.S. Patent 9,778,226, Grant Date: October 3, 2017

Talha J. Ahmad, Michael J. Black, and Mohamed N. Noui-Mehidi

Characterization of Crude Oil by Ultraviolet Visible Spectroscopy

Granted Patent: U.S. Patent 9,778,240, Grant Date: October 3, 2017

Omer R. Koseoglu, Adnan Al-Hajji, and Gordon Jamieson

Cleaning Apparatus for Heat Exchange Tubes of Air Cooled Heat Exchangers

Granted Patent: U.S. Patent 9,784,510, Grant Date: October 10, 2017

Abdullah M. Al-Otaibi

Methods and Systems for Estimating Sizes and Effects of Wellbore Obstructions in Water Injection Wells

Granted Patent: U.S. Patent 9,784,885, Grant Date: October 10, 2017

Mohammed D. Al-Ajmi and Sami A. Al-Nuaim

Image-based Analysis of a Geological Thin Section

Granted Patent: U.S. Patent 9,786,065, Grant Date: October 10, 2017

Mokhles M. Mezghani and Salem H. Shammari

Integrated Heavy Liquid Fuel Coking with Chemical Looping Concept

Granted Patent: U.S. Patent 9,790,437, Grant Date: October 17, 2017

Ali Hoteit, Mourad Younes, and Aqil Jamal

System for Multi-Zone Well Test/Production and Method of Use

Granted Patent: U.S. Patent 9,790,767, Grant Date: October 17, 2017

Shaohua Zhou

Isolatable non-Slam Piston Check Valve

Granted Patent: U.S. Patent 9,791,054, Grant Date: October 17, 2017

Omar M. Al-Amri

Methods for Determining Well Characteristics and Pore Architecture Utilizing Conventional Well Logs

Granted Patent: U.S. Patent 9,792,258, Grant Date: October 17, 2017

Johannes J. Buiting and Nicolas Leseur

Development of High Temperature Low Density Cement

Granted Patent: U.S. Patent 9,796,622, Grant Date: October 24, 2017

Abdullah S. Al-Yami, Ahmad S. Al-Humaidi, Salah H. Al-Saleh, and Turki T. Al-Subaie

Foam Concrete with the Use of Oil Ash

Granted Patent: U.S. Patent 9,796,624, Grant Date: October 24, 2017

Mohammed H. Al-Mehthel, Mohammed Maslehuddin, Saleh H. Al-Idi, and Mohammed Ibrahim

Fire-Resistant Sulfur Concrete

Granted Patent: U.S. Patent 9,796,629, Grant Date: October 24, 2017

Mohammed H. Al-Mehthel, Mohammed Maslehuddin, Saleh H. Al-Idi, and Mohammed R. Ali

Encapsulation of an Acid Precursor for Oil Field Applications

Granted Patent: U.S. Patent 9,796,919, Grant Date: October 24, 2017

Yun Chang, Mazen Kanj, and Curt Thies

Method and Composition for Contemporaneously Dimerizing and Hydrating a Feed Having Butene to Produce a Gasoline Composition

Granted Patent: U.S. Patent 9,796,941, Grant Date: October 24, 2017

Wei Xu, Thamer A. Mohammad, Aadesh Harale, and Kareemuddin M. Shaik

Remedial Second-Stage Cementing Packer

Granted Patent: U.S. Patent 9,797,219, Grant Date: October 24, 2017

Mohammed Al-Badran

Data Compression of Hydrocarbon Reservoir Simulation Grids

Granted Patent: U.S. Patent 9,797,225, Grant Date: October 24, 2017

Gustavo I. Chavez and Badr M. Harbi

Catalyst Reactor Basket

Granted Patent: U.S. Patent 9,802,173, Grant Date: October 31, 2017

Omer R. Koseoglu and Salman J. Al-Khaldi

Method for Mixing in a Hydrocarbon Conversion Process

Granted Patent: U.S. Patent 9,802,176, Grant Date: October 31, 2017

Ki-Hyouk Choi, Mohammad S. Garhoush, Bader M. Al-Otaibi, and Mohammad A. Abdullah

Enhanced Oil Recovery by in Situ Steam Generation

Granted Patent: U.S. Patent 9,803,133, Grant Date: October 31, 2017

Ayman R. Al-Nakhli and Michael J. Black

Power Generation from Waste Heat in Integrated Crude Oil Refining, Aromatics, and Utilities Facilities

Granted Patent: U.S. Patent 9,803,145, Grant Date: October 31, 2017

Mahmoud B. Noureldin, Hani M. Al-Saed, and Ahmad S. Bunaiyan

Hydrocracking Process with Interstage Steam Stripping

Granted Patent: U.S. Patent 9,803,148, Grant Date: October 31, 2017

Omer R. Koseoglu, Ali H. Al-Abdulal, Masaru Ushio, and Koji Nakano

Power Generation from Waste Heat in Integrated Aromatics and Naphtha Block Facilities

Granted Patent: U.S. Patent 9,803,505, Grant Date: October 31, 2017

Mahmoud B. Noureldin, Hani M. Al-Saed, and Ahmad S. Bunaiyan

Power Generation from Waste Heat in Integrated Crude Oil Hydrocracking and Aromatics Facilities

Granted Patent: U.S. Patent 9,803,506, Grant Date: October 31, 2017

Mahmoud B. Noureldin, Hani M. Al-Saed, and Ahmad S. Bunaiyan

Power Generation Using Independent Dual Organic Rankine Cycles from Waste Heat Systems in Diesel Hydrotreating-Hydrocracking and Continuous Catalytic Cracking Aromatics Facilities

Granted Patent: U.S. Patent 9,803,507, Grant Date: October 31, 2017

Mahmoud B. Noureldin, Hani M. Al-Saed, and Ahmad S. Bunaiyan

Power Generation from Waste Heat in Integrated Crude Oil Diesel Hydrotreating and Aromatics Facilities

Granted Patent: U.S. Patent 9,803,508, Grant Date: October 31, 2017

Mahmoud B. Noureldin, Hani M. Al-Saed, and Ahmad S. Bunaiyan

Power Generation from Waste Heat in Integrated Crude Oil Refining and Aromatics Facilities

Granted Patent: U.S. Patent 9,803,509, Grant Date: October 31, 2017

Mahmoud B. Noureldin, Hani M. Al-Saed, and Ahmad S. Bunaiyan

Power Generation Using Independent Dual Organic Rankine Cycles from Waste Heat Systems in Diesel Hydrotreating-Hydrocracking and Atmospheric Distillation-Naphtha Hydrotreating-Aromatics Facilities

Granted Patent: U.S. Patent 9,803,511, Grant Date: October 31, 2017

Mahmoud B. Noureldin, Hani M. Al-Saed, and Ahmad S. Bunaiyan

Power Generation from Waste Heat in Integrated Aromatics, Crude Distillation, and Naphtha Block Facilities

Granted Patent: U.S. Patent 9,803,513, Grant Date: October 31, 2017

Mahmoud B. Noureldin, Hani M. Al-Saed, and Ahmad S. Bunaiyan

Power Generation from Waste Heat in Integrated Hydrocracking and Diesel Hydrotreating Facilities

Granted Patent: U.S. Patent 9,803,930, Grant Date: October 31, 2017

Mahmoud B. Noureldin, Hani M. Al-Saed, and Ahmad S. Bunaiyan

Systems and Methods for Determining Water Cut of a Fluid Mixture

Granted Patent: U.S. Patent 9,804,105, Grant Date: October 31, 2017

Muhammad A. Karimi, Atif Shamim, and Muhammad Arsalan

Method for Monitoring and Improving Health and Productivity of Employees Using a Computer Mouse System

Granted Patent: U.S. Patent 9,805,339, Grant Date: October 31, 2017

Samantha J. Horseman

System for Combined Hydrogen and Electricity Production Using Petroleum Fuels

Granted Patent: U.S. Patent 9,806,364, Grant Date: October 31, 2017

Jamal Aqil and Thang V. Pham

Systems, Computer Medium and Computer Implemented Methods for Monitoring and Improving Biomechanical Health of Employees

Granted Patent: U.S. Patent 9,808,156, Grant Date: November 7, 2017

Samantha J. Horseman

Air Filter Ultrasonic Cleaning Systems and the Methods of Using the Same

Granted Patent: U.S. Patent 9,808,840, Grant Date: November 7, 2017

Mansour A. Al-Shafei, Gasan S. Alabedi, and Marwan R. Al-Dossary

Polycarbonate Polyol Compositions and Methods

Granted Patent: U.S. Patent 9,809,678, Grant Date: November 7, 2017

Scott D. Allen, Geoffrey W. Coates, Anna E. Cherian, Chris A. Simoneau, Alexei A. Gridnev, and Jay J. Farmer

System, Apparatus, and Method for Utilization of Bracelet Galvanic Anodes to Protect Subterranean Well Casing Sections Shielded by Cement at a Cellar Area

Granted Patent: U.S. Patent 9,809,888, Grant Date: November 7, 2017

Mohammed H. Al-Mubasher

Multilateral Wells Placement via Transshipment Approach

Granted Patent: U.S. Patent 9,810,052, Grant Date: November 7, 2017

Ghazi D. Al-Qahtani, Noah E. Berlow, and Mohamed Y. Soliman

Hybrid Transponder System for Long-Range Sensing and 3D Localization

Granted Patent: U.S. Patent 9,810,057, Grant Date: November 7, 2017

Howard K. Schmidt and Abdullah A. Al-Shehri

Wireless Power Transmission to Downhole Well Equipment

Granted Patent: U.S. Patent 9,810,059, Grant Date: November 7, 2017

Talha J. Ahmad

Calcium Sulfate Looping Cycles for Sour Gas Combustion and Electricity Production

Granted Patent: U.S. Patent 9,810,146, Grant Date: November 7, 2017

Ali Hoteit and Mourad Younes

Variable Speed Pipeline Pig with Internal Flow Cavity

Granted Patent: U.S. Patent 9,810,365, Grant Date: November 7, 2017

Mohamed A. Soliman

Methods, Systems, and Computer Medium having Computer Programs Stored Thereon to Optimize Reservoir Management Decisions

Granted Patent: U.S. Patent 9,816,366, Grant Date: November 14, 2017

Ghazi D. Al-Qahtani, Mohamed Y. Soliman, and Ismael De-Farias

Modified Goswami Cycle-based Conversion of Gas Processing Plant Waste Heat into Power and Cooling

Granted Patent: U.S. Patent 9,816,401, Grant Date: November 14, 2017

Mahmoud B. Noureldin and Akram H. Kamel

Adjusting a Fuel on Board a Vehicle

Granted Patent: U.S. Patent 9,816,467, Grant Date: November 14, 2017

Esam Z. Hamad and Ibrahim M. Al-Gunaibet

Power Generation Using Independent Triple Organic Rankine Cycles from Waste Heat in Integrated Crude Oil Refining and Aromatics Facilities

Granted Patent: U.S. Patent 9,816,759, Grant Date: November 14, 2017

Mahmoud B. Noureldin, Hani M. Al-Saed, and Ahmad S. Bunaiyan

Characterization of Crude Oil by Simulated Distillation

Granted Patent: U.S. Patent 9,816,919, Grant Date: November 14, 2017

Omer R. Koseoglu, Adnan Al-Hajji, and Frederick Adam

Systems and Methods for Constructing and Testing Composite Photonic Structures

Granted Patent: U.S. Patent 9,816,941, Grant Date: November 14, 2017

Enrico Bovero, Abdullah S. Al-Ghamdi, and Abdullah A. Al-Shahrani

Adjusting a Fuel on Board a Vehicle

Granted Patent: U.S. Patent 9,827,850, Grant Date: November 28, 2017

Esam Z. Hamad and Abdullah S. Al-Ramadan

Compositions of and Methods for Using Hydraulic Fracturing Fluid for Petroleum Production

Granted Patent: U.S. Patent 9,828,543, Grant Date: November 28, 2017

Fakuen F. Chang, Paul D. Berger, and Christie H. Lee

System and Method for Forming a Lateral Wellbore

Granted Patent: U.S. Patent 9,828,807, Grant Date: November 28, 2017

Shaohua Zhou

Methods and Apparatus for Collecting and Preserving Core Samples from a Reservoir

Granted Patent: U.S. Patent 9,828,820, Grant Date: November 28, 2017

Anuj Gupta, Daniel T. Georgi, and Katherine L. Hull

Method and Apparatus for Subsurface Data Transfer Using Well Fluids

Granted Patent: U.S. Patent 9,828,851, Grant Date: November 28, 2017

Clovis S. Bonavides

Modified Goswami Cycle-based Conversion of Gas Processing Plant Waste Heat into Power and Cooling with Flexibility

Granted Patent: U.S. Patent 9,828,885, Grant Date: November 28, 2017

Mahmoud B. Noureldin and Akram H. Kamel

Computer Mouse for Monitoring and Improving Health and Productivity of Employees

Granted Patent: U.S. Patent 9,830,576, Grant Date: November 28, 2017

Samantha J. Horseman

Computer Mouse System and Associated Computer Medium for Monitoring and Improving Health and Productivity of Employees

Granted Patent: U.S. Patent 9,830,577, Grant Date: November 28, 2017

Samantha J. Horseman

Systems, Computer Medium and Computer Implemented Methods for Coaching Employees based Upon Monitored Health Conditions Using an Avatar

Granted Patent: U.S. Patent 9,833,142, Grant Date: December 5, 2017

Samantha J. Horseman

Lightweight Foam Concrete with Elemental Sulfur

Granted Patent: U.S. Patent 9,834,477, Grant Date: December 5, 2017

Mohammed H. Al-Mehthel, Saleh H. Al-Idi, Mohammed Maslehuddin, and Mohammed Shameem

Systems and Methods for Producing Propylene

Granted Patent: U.S. Patent 9,834,497, Grant Date: December 5, 2017

Sohel Shaikh, Aqil Jamal, and Zhonglin Zhang

Adhesive Compositions and Methods

Granted Patent: U.S. Patent 9,834,710, Grant Date: December 5, 2017

Vahid Sendijarevic, Scott D. Allen, and James O'Connor

Ecofriendly Lubricating Additives for Water-based Wellbore Drilling Fluids

Granted Patent: U.S. Patent 9,834,718, Grant Date: December 5, 2017

Md. Amanullah, Abdulaziz Bubshait, and Omar Fuwaires

Compositions of and Methods for Using Hydraulic Fracturing Fluid for Petroleum Production

Granted Patent: U.S. Patent 9,834,721, Grant Date: December 5, 2017

Fakuen F. Chang, Paul D. Berger, Christie H. Lee, and Susanta Mohapatra

Method for Assessing Ablation Modulai of Mud Cakes to Predict Ease of Mud Cake Removal or Cleaning Efficiency of Cleaning/Washing/Spacer Fluids

Granted Patent: U.S. Patent 9,835,608, Grant Date: December 5, 2017

Md. Amanullah, Mohammed K. Al-Arfaj, and Adel A. Al-Ansari

Cored Rock Analysis Planning through CT Images

Granted Patent: U.S. Patent 9,842,431, Grant Date: December 12, 2017

Sinan Caliskan and Abdullah M. Shebatalhamd

Systems, Computer Medium and Computer Implemented Methods for Monitoring and Improving Biometric Health of Employees

Granted Patent: U.S. Patent 9,844,344, Grant Date: December 19, 2017

Samantha J. Horseman

Sulfur Extended Polymer for Use in Ashpalt Binder and Road Maintenance

Granted Patent: U.S. Patent 9,845,371, Grant Date: December 19, 2017

Mohammed H. Al-Mehthel, Saleh H. Al-Idi, Ibnelwaleed Hussein, Hamad Al-Abdulwahhab and Junaid Akhtar

Recovery and Re-Use of Waste Energy in Industrial Facilities

Granted Patent: U.S. Patent 9,845,995, Grant Date: December 19, 2017

Mahmoud B. Noureldin and Hani M. Al-Saed

Recovery and Re-Use of Waste Energy in Industrial Facilities

Granted Patent: U.S. Patent 9,845,996, Grant Date: December 19, 2017

Mahmoud B. Noureldin and Hani M. Al-Saed

Magnetic Omni-Wheel

Granted Patent: U.S. Patent 9,849,722, Grant Date: December 26, 2017

Brian J. Parrott, Pablo Carrasco Zanini Gonzalez, Ali H. Outa, Fadl H. Abdel Latif, and Hassane A. Trigui

Hinged Vehicle Chassis

Granted Patent: U.S. Patent 9,849,925, Grant Date: December 26, 2017

Ali H. Outa, Brian J. Parrott, Pablo Carrasco Zanini Gonzalez, and Fadl H. Abdel Latif

Polycarbonate Polyol Compositions and Methods

Granted Patent: U.S. Patent 9,850,345, Grant Date: December 26, 2017

Jay J. Farmer

Recovery and Re-Use of Waste Energy in Industrial Facilities

Granted Patent: U.S. Patent 9,851,153, Grant Date: December 26, 2017

Mahmoud B. Noureldin and Hani M. Al-Saed

System and Method for Calculating the Orientation of a Device

Granted Patent: U.S. Patent 9,851,721, Grant Date: December 26, 2017

Pablo Carrasco Zanini Gonzalez, Fadl H. Abdel Latif, and Ali H. Outa

SUBSCRIPTION ORDER FORM

To begin receiving the *Saudi Aramco Journal of Technology* at no charge, please complete this form.

Please print clearly.

Name _____

Title _____

Organization _____

Address _____

City _____

State/Province _____

Postal code _____

Country _____

E-mail address _____

Number of copies _____

TO ORDER

By phone/email:

Saudi Aramco Public Relations Department
JOT Distribution
+966-013-876-0498
william.bradshaw.1@aramco.com

By mail:

Saudi Aramco Public Relations Department
JOT Distribution
Box 5000
Dhahran 31311
Saudi Arabia

Current issues, select back issues and multiple copies of some issues are available upon request.

The *Saudi Aramco Journal of Technology* is published by the Saudi Aramco Public Relations Department, Saudi Arabian Oil Company, Dhahran, Saudi Arabia.

GUIDELINES FOR SUBMITTING AN ARTICLE TO THE SAUDI ARAMCO JOURNAL OF TECHNOLOGY

These guidelines are designed to simplify and help standardize submissions. They need not be followed rigorously. If you have additional questions, please feel free to contact us at Public Relations. Our address and phone numbers are listed on page 80.

Length

Varies, but an average of 2,500-3,500 words, plus illustrations/photos and captions. Maximum length should be 5,000 words. Articles in excess will be shortened.

What to send

Send text in Microsoft Word format via email or on disc, plus one hard copy. Send illustrations/photos and captions separately but concurrently, both as email or as hard copy (more information follows under file formats).

Procedure

Notification of acceptance is usually within three weeks after the submission deadline. The article will be edited for style and clarity and returned to the author for review. All articles are subject to the company's normal review. No paper can be published without a signature at the manager level or above.

Format

No single article need include all of the following parts. The type of article and subject covered will determine which parts to include.

Working title

Abstract

Usually 100-150 words to summarize the main points.

Introduction

Different from the abstract in that it "sets the stage" for the content of the article, rather than telling the reader what it is about.

Main body

May incorporate subtitles, artwork, photos, etc.

Conclusion/summary

Assessment of results or restatement of points in introduction.

Endnotes/references/bibliography

Use only when essential. Use author/date citation method in the main body. Numbered footnotes or endnotes will be converted. Include complete publication information. Standard is *The Associated Press Stylebook*, 52nd ed. and *Webster's New World College Dictionary*, 5th ed.

Acknowledgments

Use to thank those who helped make the article possible.

Illustrations/tables/photos and explanatory text

Submit these separately. **Do not place in the text.** Positioning in the text may be indicated with placeholders. Initial submission may include copies of originals; however, publication will require the originals. When possible, submit both electronic versions, printouts and/or slides. Color is preferable.

File formats

Illustration files with .EPS extensions work best. Other acceptable extensions are .TIFF, .JPEG and .PICT.

Permission(s) to reprint, if appropriate

Previously published articles are acceptable but can be published only with written permission from the copyright holder.

Author(s)/contributor(s)

Please include a brief biographical statement.

Submission/Acceptance Procedures

Papers are submitted on a competitive basis and are evaluated by an editorial review board comprised of various department managers and subject matter experts. Following initial selection, authors whose papers have been accepted for publication will be notified by email.

Papers submitted for a particular issue but not accepted for that issue will be carried forward as submissions for subsequent issues, unless the author specifically requests in writing that there be no further consideration. Papers previously published or presented may be submitted.

Submit articles to:

Editor
The *Saudi Aramco Journal of Technology*
C-11B, Room AN-1080
North Admin Building #175
Dhahran 31311, Saudi Arabia
Tel: +966-013-876-0498
Email: william.bradshaw.1@aramco.com.sa

Submission deadlines

Issue	Paper submission deadline	Release date
Fall 2018	May 23, 2018	September 30, 2018
Winter 2018	August 16, 2018	December 31, 2018
Spring 2019	November 20, 2018	March 31, 2019
Summer 2019	February 21, 2019	June 30, 2019

NOTES:

NOTES:

NOTES:

New Mechanisms of Iron Sulfide Deposition during Acid Stimulation in Sour Gas Carbonate Reservoir

Dr. Tao Chen, Dr. Qiwei Wang, and Dr. Fakuen F. Chang

ABSTRACT

Iron sulfide deposition in sour gas wells has caused severe flow assurance issues. It affects well deliverability, interferes with well surveillance, and restricts well intervention. The mitigation of iron sulfide deposition is notoriously difficult. To make suitable strategies to manage iron sulfide, it is essential to understand the source of iron and mechanisms of iron sulfide deposition.

Optimizing Cost and Restoring Integrity with the First Saudi Aramco Mechanical Descaling Using a Wireline Torque Action Debris Breaker Tool

Abdullah A. Al-Ghamdi, Ibrahim M. El-Zefzafy, Mohammad H. Al-Malki, and Russell Turner

ABSTRACT

This article strives to address the great success of utilizing the torque action debris breaker (TADB) tool as a wireline means to restore wellbore accessibility. The tool was trial tested to remove hard scale accumulation consisting of 95% iron compounds. Iron compound scales are generally among the most difficult types of scale to be removed by chemical means as historical data showed high failure rates in terms of succeeding to eliminate wellbore blockage.

Understanding Shale Petrophysics Helps in Drilling Stable Boreholes: Case Studies

Mohammed K. Al-Arfaj and Hamad S. Al-Kharra'a

ABSTRACT

Drilling stable boreholes in shale formations can be a very challenging task when water-based drilling fluids are used. The interactions between the water phase in drilling fluids with shale rocks cause different drilling problems, such as shale swelling and dispersion. The extent to which a shale sample swells or disperses depends on the clay content of the shale. Some types of clay have a tendency to swell more while others have a tendency to disperse more.

New Understanding on Iron Sulfide Deposition during Acid Stimulation in Sour Gas Wells Using an Advanced Modeling Approach

Dr. Peng Lu, Dr. Tao Chen, Dr. Qiwei Wang, and Dr. Fakuen F. Chang

ABSTRACT

Iron sulfide scaling has been a persistent problem for oil and gas production from sour reservoirs. To study iron sulfide deposition in near wellbore formations, an advanced numerical geochemical method, reactive transport modeling (RTM), is applied in this article to simulate the iron-bearing scale formation — especially during and post-acid stimulation. The code "TOUGHREACT" is used for simulation.